A Measurement of Triple Gauge Boson Couplings in Fully Leptonic W Decays

Alun Wyn Lloyd

Thesis submitted for the degree of
Doctor of Philosophy

Particle Physics Group
School of Physics and Astronomy
University of Birmingham

November 2000

Abstract

This thesis presents two investigations performed on data collected by the OPAL detector at LEP, the large electron-positron collider at CERN, Geneva.

The main investigation uses data recorded during 1999 with centre-of-mass energies in the range 192–202 GeV to measure the charged triple gauge boson coupling parameters, κ_γ, λ and g_1^Z in fully leptonic W-pair decays. A sample of 157 events is selected, and a set of five angles, which is sensitive to the coupling strength, is reconstructed for each event. An Optimal Observables technique is used to extract the coupling values from this sample by comparing them with simulated events. The triple gauge boson couplings are measured to be

$$\begin{aligned} \kappa_\gamma &= 1.18^{+0.46}_{-0.32}, \\ \lambda &= -0.13^{+0.13}_{-0.12}, \\ g_1^Z &= 0.85^{+0.17}_{-0.16}, \end{aligned}$$

where the errors include both the statistical and systematic uncertainties. This analysis alone demonstrates the presence of couplings between three gauge bosons, and the values predicted by the Standard Model are κ_γ=+1.0, λ=0.0 and g_1^Z=+1.0.

A second investigation uses data recorded during 1991–5 with centre-of-mass energies at and around the mass of the Z boson. An inclusive b hadron reconstruction is developed and then employed in the reconstruction of orbitally excited B meson states, B_J^*. Some of the results describing the properties of these states are presented.

Author's Contribution

The results presented in this thesis represent work which was carried out within the OPAL collaboration. The achievements of the collaboration are a result of the combined efforts of more than 300 people. A great effort is required to maintain and operate the detector as well as to analyse and publish its data. This complex structure of responsibilities means that the effort of an individual can be difficult to appreciate.

The main data analysis effort involved a measurement of the triple gauge boson coupling parameters. This was undertaken as part of the OPAL triple gauge coupling working group. My contribution was to develop the analysis for the extraction of the coupling values and extend it to cover data samples with several centre-of-mass energies. The techniques were then applied to the most recent events which were recorded during 1999 with centre-of-mass energies in the range 192–202 GeV. This included performing tests and checks on the procedure. The results in this thesis were first presented in the summer conferences of 2000, and they have been combined with those from other OPAL analyses and LEP collaborations.

The first year was involved in the development and testing of a procedure used for the inclusive reconstruction of b hadron events recorded by OPAL between 1991 and 1995. This was used in the investigation of orbitally excited B mesons. Involvement in this topic continued as a member of the editorial board for an OPAL paper on the subject which has now been submitted for publication.

The Birmingham University OPAL group is responsible for the maintenance and running of the Muon Endcap subdetector, which was built in conjunction with the Rutherford Appleton Laboratory. My involvement was with the running of this subdetector while resident at CERN for two of the three years. This involved daily monitoring of the gas, high voltage and data acquisition systems as well as of the data quality. It also included reporting the status of running to the collaboration as well as being available to respond to queries, problems and emergencies day and night.

Acknowledgements

The last three years have been some of the best and most influential of my life, for different reasons. This PhD course has given me many fantastic opportunities, therefore I would like to thank the University of Birmingham High Energy Physics Group for offering me the place. During undergraduate and summer projects I came to know several members of the group, in particular Pete Watkins who tutored me in my first year in 1993, and began my curiosity in the subject. I am very happy and pleased to thank Dave Charlton, my supervisor throughout this course. I have benefited enormously from his genuine competence and expertise which has provided many useful and thorough discussions, his ability to explain all levels of a problem, from the mundane coding to the full implications of the research, and his overall approach which has really helped me to work efficiently. There are many other people in the group with whom I have had many enjoyable and useful conversations. Particularly while on-call for the OPAL muon endcaps I could always rely on John Wilson, Jim Homer, Nige Watson, Alan Watson and Tom McMahon for enlightening and reassuring discussions and for providing familiar faces in 28-R-015.

Looking after the Birmingham muon endcap subdetector was the main reason for receiving the great opportunity to live in Geneva for two of the three years of the course. Despite needing to be responsible, which implied being within 'one hour' of the detector, I managed to experience to the maximum, through travel, the huge opportunities which living in Geneva presents. At every free moment I indulged in exploring the nearby and not-so-nearby regions of Europe. The beauty and variety of the terrains of Switzerland, the tranquility and patisserie of the neighbouring French regions, the beverages of Southern Germany, and the history, life and beauty of the Italian cities, lakes and mountains. The winter months were devoted to the tremendously enjoyable activity of sliding around the Alps. Skiing was a sport I had never tried before moving to Geneva, but the result of two courses from the CERN ski club and plenty of practice has left me eager to tackle anything.

These fantastic times were shared with many of the people who I met and spent time with in Geneva; Shaun, Scott, Jeremy, Steve, Tom, Russell, Vick, Barbara, Andy, Brinnick, Philippe, Goetz, Dave, Helen... I hope that Dave, Andy, Kev and Rob, who came out to visit me in Geneva, also had a great time. I wish to apologise to Paul for keeping him waiting on the bridge in Zurich as I missed our rendez-vous by hours! Let's not forget my friends back in the HEP group, Dave, Mike and Paul.

I said that the last few years have been the best of my life, my parents deserve lots of thanks for always helping me, but finally I'd like to thank Andrea for everything.

Alun, November 2000.

Contents

List of Figures

List of Tables

Chapter 1

Theoretical Framework

The theory which is currently used to describe the fundamental constituents of matter and their interactions is called the 'Standard Model', see for example [1, 2]. The current view of the way in which matter is composed, built upon many years of research and observations, is of fundamental, indivisible components. The Standard Model is a theory developed to describe and predict their behaviour and it is extremely successful at doing so. A mathematical framework which connects the concepts of fundamental particles and the forces between them arose from the combination of relativistic and quantum mechanics, which is referred to as Relativistic Quantum Field Theory. Particular aspects of this theory are used to build the Standard Model. At the LEP accelerator at CERN, Geneva, the predictions of the Standard Model are tested by observing the products of electron-positron collisions.

This chapter begins with an overview of the elementary particles and interactions which make up the Standard Model of particle physics. It then discusses the use of gauge field theories to describe their behaviour with particular attention given to the theories of the electromagnetic, weak and strong forces. Some of the predictions of the theory are also presented.

1.1 Overview of the Standard Model

It is thought that the Universe is composed of two types of elementary particles, 'fermions' and 'bosons', which are distinguished by their spin angular momentum. The fermions form the matter content, they are described by Fermi-Dirac statistics and have half-integer spin. The bosons are the mediating particles of the fundamental forces, they are described by Bose-Einstein statistics and they have integer spin. The fermions interact via four fundamental forces, the electromagnetic, weak, strong and gravitational forces. Gravity is responsible for attracting bodies with mass. Although it is the most apparent, it is insignificant for elementary particles due to their small masses and it is not included in the Standard Model.

Fermions are divided into 'leptons' and 'quarks' according to the interactions that they experience. All fermions experience the weak force, and the charged fermions also experience the electromagnetic force. In addition, the quarks experience the strong force whereas the leptons do not.

- There are six types of **leptons**, called the electron (e), muon (μ) and tau (τ), and their associated neutrinos (ν_{e}, ν_μ and ν_τ). The first three have a single unit of electric charge while the neutrinos are electrically neutral.
- There are also six 'flavours' of **quarks**, called up (u), down (d), strange (s), charm (c), bottom (b) and top (t). These particles have a fractional charge, either $+\frac{2}{3}e$ or $-\frac{1}{3}e$, where e is the electron charge. They also possess a property called 'colour' where each quark can be either red, green or blue. Quarks do not exist alone but are found bound into hadrons, either into groups of three, called 'baryons', or as quark-antiquark pairs, called 'mesons'.

For each one of these particles there is an antimatter partner called the antiparticle which is identical to the original in almost every respect except that it has reversed internal quantum numbers, such as electric charge and colour. An antiparticle is denoted by a line drawn above the particle symbol, for example a b quark and its antiparticle,

1st Generation	2nd Generation	3rd Generation	Charge
Leptons			
e^- (0.511 MeV/c^2)	μ^- (105.7 MeV/c^2)	τ^- (1,777 MeV/c^2)	-1e
ν_e ($<$ 15 eV/c^2)	ν_μ($<$ 0.17 MeV/c^2)	ν_τ($<$ 18.2 MeV/c^2)	0
Quarks			
u (1–5 MeV/c^2)	c (1.1–1.4 GeV/c^2)	t (174 $\pm$ 5 GeV/c^2)	$+\frac{2}{3}e$
d (3–9 MeV/c^2)	s (60–170 MeV/c^2)	b (4.1–4.4 GeV/c^2)	$-\frac{1}{3}e$

Table 1.1: The members of the three fermion generations together with their masses (shown in brackets) and charges.

$\overline{\mathrm{b}}$, or by the reversed charge, for example an electron, e^-, and the positron e^+. The leptons and quarks are grouped into three 'families' or 'generations' which have sequentially increasing masses and shorter lifetimes. The particles introduced so far are summarised together with their charges and masses in table 1.1 [3]. 'Everyday' matter is built from only the first generation of fermions, while the others are produced in high energy interactions. All of these fermions have now been discovered in experiments, the top quark was observed directly in $p\overline{p}$ collisions by the CDF [4] and D0 [5] collaborations at FNAL during 1995, and the announcement for the direct observation of the tau neutrino was made in July 2000 by the DONUT collaboration also at FNAL [6]. The mass of the neutrino is also an important subject of investigation since if it has mass it may be able to oscillate between the different types as recent results from the Super-Kamiokande experiment suggest [7].

In the Standard Model, the forces of nature are understood in terms of the exchange of virtual gauge bosons between the fermions. The four fundamental forces have already been introduced and their range, R, is governed by the mass of the exchange particle, m, via the Heisenberg Uncertainty Principle, leading to $R \leq \hbar/mc$, where $\hbar$ is the Planck constant divided by 2π. In this way, a massless particle can be created from the vacuum for an infinite time period and therefore travel an infinite distance, so massless mediators have infinite range. Conversely, mediators with finite mass can only be created for a finite time period and therefore have a finite range.

Despite being ignored in the Standard Model, gravity, which extends over infinite distances acting between objects with mass, is expected to be mediated by the unobserved massless particle called the graviton. The electromagnetic force also acts over infinite distances, it acts between particles carrying electric charge and is mediated by the massless photon, γ. Since the photon has no charge it does not interact with itself. This force is described accurately by the theory of Quantum Electrodynamics (QED). The nuclear forces are the weak and the strong forces which act over very short distances. The weak force is carried by the massive W and Z bosons, also called charged and neutral currents, which couple to all fermions. These bosons are heavy and therefore this force has a very short range. At the energies at which these bosons are produced, the weak force becomes as strong as the electromagnetic force and the theories describing the two have been successfully unified into a single Electroweak Theory. The strong force takes place between colour carrying particles and it is responsible for the binding of quarks. It is carried by the massless gluon, g, and described by the theory of Quantum Chromodynamics (QCD). Since the gluons themselves carry colour they are able to self interact which limits the effective range of the force. These gauge bosons are summarised together with their charges and masses in table 1.2 [3].

Each generation of leptons has its own lepton number which is conserved in known reactions, preventing the different generations from mixing. This is not the case for the quark families. The three quark generations listed in table 1.1 are the mass eigenstates of the weak interaction, whereas the states observed in the particle interactions, called the weak eigenstates, are $\begin{pmatrix} u \\ d' \end{pmatrix}$, $\begin{pmatrix} c \\ s' \end{pmatrix}$ and $\begin{pmatrix} t \\ b' \end{pmatrix}$. The two sets of eigenstates are related to each other through the three-by-three Cabbibo-Kobayashi-Maskawa (CKM) matrix [8, 9] which is given by

$$\begin{pmatrix} d' \\ s' \\ b' \end{pmatrix} = \begin{pmatrix} V_{ud} & V_{us} & V_{ub} \\ V_{cd} & V_{cs} & V_{cb} \\ V_{td} & V_{ts} & V_{tb} \end{pmatrix} \begin{pmatrix} d \\ s \\ b \end{pmatrix}.$$

Interaction	Gauge boson	Charge
Electromagnetic	γ (0)	0
Weak	$\mathrm{W}^{\pm}$ $(80.41 \pm 0.10\,\mathrm{GeV}/c^2)$	$\pm 1e$
	Z^0 $(91.188 \pm 0.007\,\mathrm{GeV}/c^2)$	0
Strong	g (0)	0

Table 1.2: The gauge vector bosons together with their masses (shown in brackets) and their charges.

The values in this matrix have been experimentally measured from the observation of weak decays and neutrino scattering experiments, and their 90% confidence limit values are currently [3]

$$\begin{pmatrix} 0.9745-0.9760 & 0.217-0.224 & 0.0018-0.0045 \\ 0.217-0.224 & 0.9737-0.9753 & 0.036-0.042 \\ 0.004-0.013 & 0.035-0.042 & 0.9991-0.9994 \end{pmatrix}.$$

Since the matrix is almost diagonal, the weak decay occurs dominantly within the same generation, however, the non-zero off diagonal terms show that cross-generational decays can occur. Heavy quarks can therefore decay into first generation quarks, primarily in a series of steps such as $\mathrm{b} \to \mathrm{c} \to \mathrm{s} \to \mathrm{u}$.

1.2 Gauge Field Theories

Gauge field theories have been very successful at describing and predicting the properties of particle interactions. Before discussing the properties of these theories it is useful to introduce the powerful concept of symmetries in physical systems. Symmetries are evident in classical physics, such as the motion of planets, but at the particle level the concept can be used to simplify the complexities of quantum mechanics. Symmetries yield conservation laws, and likewise conservation laws reveal underlying symmetries (Noether's theorem). For example, if a system is invariant, or appears unchanged, under a translation in space, then momentum will be conserved. More formally, a symmetry, S, exists if the Hamiltonian, H, of the system, which is a function expressing the energy of the system in terms of its momentum and position, is invariant under the transformation given by S, so $[S, \mathrm{H}] = 0$.

An expression called the 'Lagrangian', or Lagrangian density, $\mathcal{L}$, is a function of fields and their space-time derivatives which describes the physical system, it is analogous to the classical Lagrangian which is expressed in terms of the kinetic energy, T, and the potential energy, V, so that $\mathcal{L} = T - V$. In the field theory Lagrangian are the matter fields representing the fundamental particles, and terms controlling the way in which they interact with each other.

Another important concept in gauge theories is that of phase transformations. A wave function, $\psi(x)$, describing a state, can undergo a phase transformation, or rotation, such as

$$\psi(x) \rightarrow \psi'(x) = e^{i\phi}\psi(x).$$

If ϕ is a constant then this is referred to as a *global* phase transformation. Since the quantum mechanical observables are unchanged by this transformation, the absolute phase of the wave function cannot be measured and a global phase symmetry exists. In the theory of QED, which arose from incorporating Maxwell's framework for electromagnetism with quantum mechanics, the Lagrangian for free electrons is globally phase invariant and the corresponding conserved quantum number is charge. If, however, ϕ is allowed to be space-time dependent, becoming $\phi(x)$, which is also known as a *local* phase transformation, the quantum mechanical observables can only be made invariant if a new field is introduced. In QED, this new field behaves like the photon field, and the Langrangian for free electrons becomes one in which the electrons experience the electromagnetic interaction. The Lagrangian is then said to have *gauge* symmetry. These new fields transform differently to the fermion fields and they are found to correspond to the gauge bosons themselves. The set of local phase transformations, $e^{i\phi(x)}$, form a mathematical group, and in QED this is called the U(1) group. It is said that each generator of the gauge group introduces a conserved quantity and in particular a

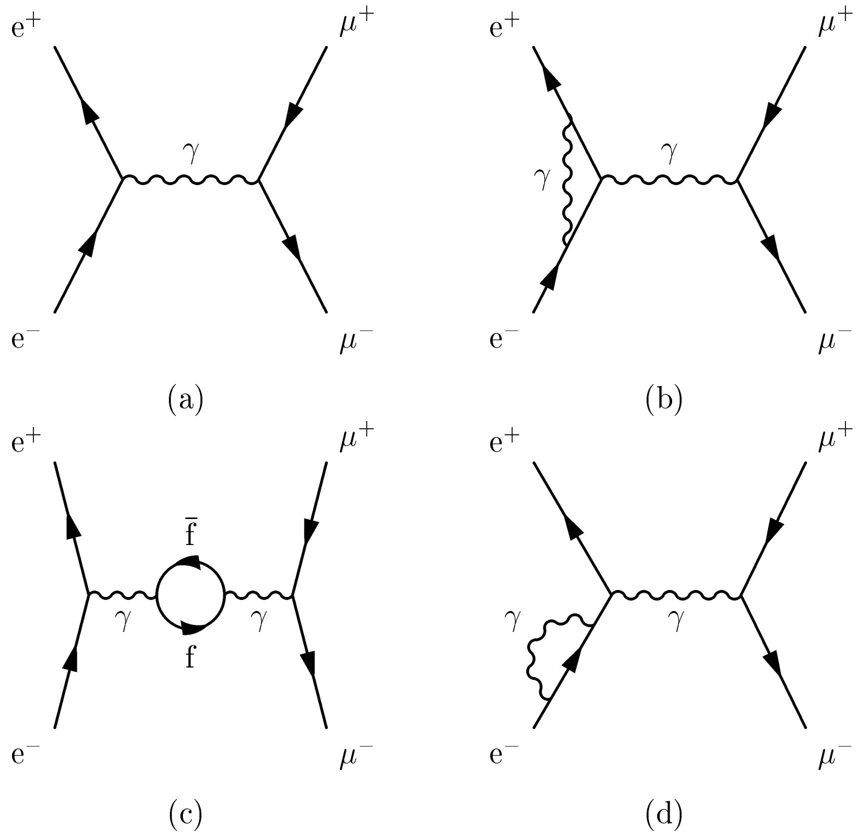

Figure 1.1: Feynman diagrams for the QED process, $e^+e^- \to \gamma \to \mu^+\mu^-$, for (a) the lowest order diagram and (b) a first order correction. Diagrams (c) and (d) show QED corrections for the same process involving a fermion loop and an internal photon respectively.

massless gauge boson field.

For gauge theories to be useful they needs to be able to predict physical quantities such as production cross-sections, angular distributions and decay rates which can be compared to experimental observation. A pictorial representation of the processes occurring in the theory was developed to aid in the calculations and these are called 'Feynman diagrams'. The physical observables arising from the process in these diagrams are determined using Feynman rules which have an intimate connection with the Lagrangian.

The Feynman diagram for one of the most basic QED interactions between leptons and a photon, in this case the electron-positron annihilation into a virtual photon producing a muon pair, $e^+e^- \to \gamma \to \mu^+\mu^-$, is shown in figure 1.1(a). The diagram describes the propagation of the incoming and outgoing particles through space and time where straight lines represent the fermions and wavy lines the boson propagators. At each vertex, energy and momentum are conserved, and each represents an interaction between the participating particles. Each is assigned a factor, e, which is related to the so called 'fine structure constant', α, which describes the strength of the electromagnetic coupling[a]. The process shown in figure 1.1(a) is called a lowest order process since only the smallest number of couplings is involved, and the results from the calculation performed on this are referred to as 'Born level'. To calculate the total cross-section for this process, the result for this diagram, together with the contributions from all of the other diagrams which have an incoming electron and positron, and an outgoing muon pair must each be calculated and added together. The diagrams in figures 1.1(b-d) represent a few of the higher order contributions and the results which these diagrams contribute are referred to as 'radiative corrections'. There are two types of such diagrams, the so called 'QED corrections' which arise from the addition of photons to the Feynman diagram, and 'weak corrections' where massive bosons are exchanged. There is obviously an infinite series of such higher order diagrams with increasing complexity.

The Feynman rules can be used to calculate these more complex diagrams. Mathematically, the result is a power series in terms of the coupling constant, α, and since for QED $\alpha \ll 1$ the series should converge rapidly. Unfortunately a problem arises from diagrams which contain loops in the fermion or propagator lines. In these cases the momentum flowing around the loop is unconstrained and so the integral which determines their contribution must be performed over an infinite range. This causes it to be divergent, rendering the perturbation expansion unphysical. The problem can be addressed and the infinities cancelled by redefining the parameters being used, this technique is called 'renormalisation'.

Renormalisation consists of reabsorbing the loops in the divergent diagrams into the original definition of the electron or photon lines. The electron charge, originally defined as the charge of the bare electron, is now chosen to include the effects of

[a] $\alpha = \frac{e^2}{4\pi} \simeq \frac{1}{137}$.

all of these higher order processes so that now the bare charge is infinite, and the redefined charge is set equal to its measured finite value. This can be visualised as the electron being surrounded by a cloud of virtual activity consisting of the emission and reabsorption of virtual photons which convert to virtual $f\bar{f}$ pairs. These virtual particles have the effect of shielding the infinite electron charge. Actually, when the electron structure is investigated by probing more deeply into it, its charge appears to increase since the outer layers of the shielding are being penetrated. The same effect manifests itself in the measurement of the QED coupling constant, α, where at higher energies it is found to increase, as such it is referred to as a 'running electromagnetic coupling constant'.

It has been shown that all gauge theories are renormalisable [10], and the success of QED motivated the development of similar theories for the weak and the strong interactions which will be described in the following sections.

1.2.1 Electroweak Theory

The unification of the electromagnetic and weak forces into a single gauge field theory, called the Electroweak Theory, was proposed by Glashow, Salam and Weinberg [11–13]. Unlike QED where the vector boson is massless, Electroweak Theory must describe a massive vector boson since the weak interaction takes place over a finite distance. If a mass term is introduced into the Lagrangian describing the interaction, the theory ceases to remain gauge invariant and so the power of the theory is lost. This problem was solved by introducing *hidden* symmetries where the symmetry is spontaneously broken but the Lagrangian continues to be symmetric, in this way the gauge fields can acquire mass. Furthermore, this theory remains renormalisable.

Gauge transformations can be represented by matrices, and these matrices can form more complicated groups than U(1). For the Electroweak Theory it was found that the $\mathrm{SU(2)_L} \otimes \mathrm{U(1)_Y}$ symmetry group structure works, in which the conserved property is the weak charge. $\mathrm{SU(2)_L}$ is the weak *isospin* group which is parity violating and acts only on *left*-handed fermions, hence the label 'L'. $\mathrm{U(1)_Y}$ is the weak *hypercharge* group which is given the label 'Y'. The $\mathrm{SU(2)_L}$ group is non-Abelian which allows the gauge bosons which are generated by it to interact directly with each other. This gives rise to the triple gauge boson coupling vertices which are investigated in this thesis. To enable the parity violation of $\mathrm{SU(2)_L}$ the fermions are divided into two sets according to their weak isospin, T. The left-handed fermions are grouped into weak isospin doublets,

$$\begin{pmatrix} \nu_{\mathrm{e}} \\ \mathrm{e} \end{pmatrix}_{\mathrm{L}}, \begin{pmatrix} u \\ d \end{pmatrix}_{\mathrm{L}}, \ldots ,$$

with the third component of the weak isospin having $T^3 = \pm\frac{1}{2}$, while the right-handed fermions transform as singlets,

$$\mathrm{e_R}, \mathrm{u_R}, \mathrm{d_R}, \ldots ,$$

with $T^3 = 0$. The relationship between the third component of the weak isospin, T^3, the weak hypercharge, Y, and the electric charge, Q, is given by

$$Q = T^3 + \frac{Y}{2}.$$

In this scheme T^3 and Y are conserved quantities and so the conservation of charge is implicit.

The $\mathrm{SU(2)_L} \otimes \mathrm{U(1)_Y}$ group has four gauge bosons associated to these conserved quantities, these are the three weak bosons of $\mathrm{SU(2)_L}$, $\mathrm{W^1}$, $\mathrm{W^2}$ and $\mathrm{W^3}$, which couple to the weak isospin, and the neutral boson, B, which couples to the weak hypercharge. The physical $\mathrm{W^\pm}$ gauge bosons, which mediate the charged current interaction within the weak doublet, emerges from a linear orthogonal combination of the $\mathrm{W^1}$ and $\mathrm{W^2}$ fields such that

$$\mathrm{W^\pm} = \frac{1}{\sqrt{2}}[\mathrm{W^1} \mp i\mathrm{W^2}].$$

Linear combinations of the remaining $\mathrm{W^3}$ field and the B field manifest as the physical fields describing the photon and the $\mathrm{Z^0}$ such that

$$\gamma = \mathrm{W^3} \sin\theta_{\mathrm{W}} + \mathrm{B}\cos\theta_{\mathrm{W}},$$

$$\mathrm{Z^0} = \mathrm{W^3}\cos\theta_{\mathrm{W}} - \mathrm{B}\sin\theta_{\mathrm{W}}.$$

In these expressions, θ_W is the weak mixing angle which determines the relative strength of the couplings of the fermions to the W and B fields, referred to as g and g' respectively. They are related by

$$g \sin\theta_W = g' \cos\theta_W = e,$$

and they also determine the relationship between the masses of the W and Z bosons by $M_W = M_Z \cos\theta_W$. The value of θ_W is not predicted by the Standard Model and it must be measured experimentally.

1.2.2 Quantum ChromoDynamics

Quantum Chromodynamics is the gauge field theory describing the strong interaction. The associated symmetry group is $SU(3)_C$ and the theory generates an octet of *coloured* gauge bosons, hence the label 'C', called gluons. In general, the Feynman diagrams for QCD are similar to those for QED except that the electron lines are replaced by quarks, and the photon propagators by gluons. Calculations for QCD processes are more complicated since gluons themselves carry colour and therefore self-interact. As with the fine structure constant, the strong coupling constant, α_s, varies as a function of the energy scale, except this time in the opposite sense so that it becomes weaker as the energy increases, or as the distance becomes shorter. At around 1 GeV α_s is close to unity, this means that the contributions from higher order corrections to the lowest order process are significant. In the same way that an electron was visualised surrounded by a cloud of virtual particles which shielded the charge, the quark can be visualised surrounded by a cloud of virtual gluons, but since the gluons themselves carry colour charge, they effectively increase the observed gluon charge of the bare quark.

At high energies and small distances, where the strong coupling constant is small, the individual particles can be regarded as essentially free, this is referred to as 'asymptotic freedom'. In this low α_s regime, perturbative QCD calculations can be used successfully. At low energies and large distances, where the strong coupling constant

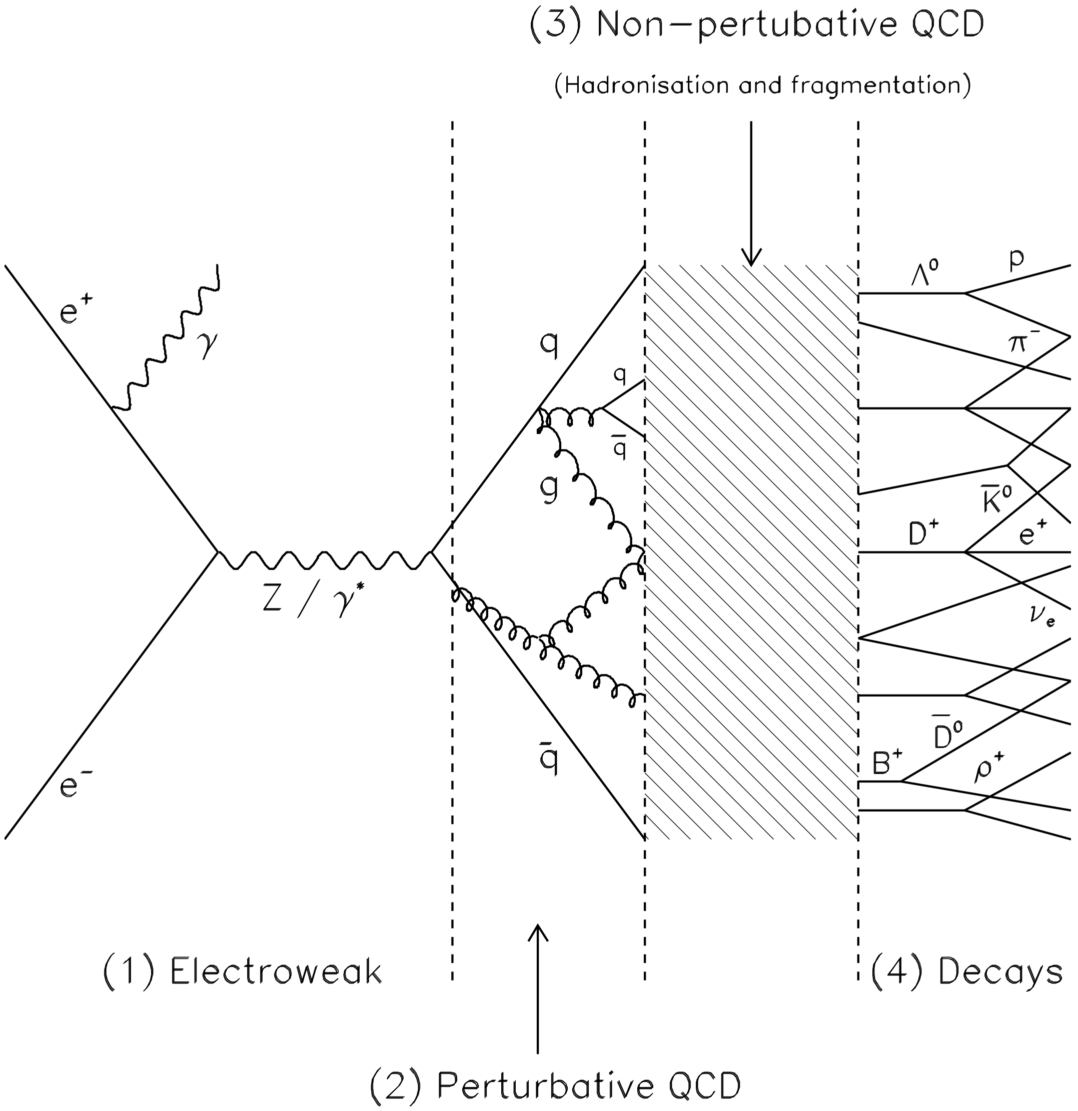

Figure 1.2: A schematic diagram of an electron-positron interaction leading to quark pair production. The process can be described in four separate phases: the $e^+e^- \rightarrow q\overline{q}$ electroweak phase (1), a perturbative QCD phase (2), a non-perturbative fragmentation and hadronisation phase (3) followed by the decays of the hadrons (4).

is large, the QCD rule of 'colour confinement' states that quarks can only exist in colourless bound states, these were introduced as the mesons and baryons. The gluon field around a lone colour charge would have sufficient energy to create new coloured particles around the quark, and the quark is said to 'dress'. If α_{s} is too large then the perturbative approach to calculating physical quantities in QCD becomes useless.

A diagram of the quark pair production process at LEP is presented in figure 1.2. The electron-positron interaction producing the primary quark-antiquark pair is an electroweak process. These quarks radiate gluons which produce more quark-antiquark pairs. In principle this part of the process can be predicted by perturbative QCD. As the energy of these products fall, the theory becomes non-perturbative and it is then necessary to use phenomenological models to describe the hadronisation and fragmentation which subsequently takes place. Finally, these hadrons may themselves be unstable and decay into the observed particles.

1.3 LEP Physics

The Electroweak Theory can be used to calculate physically observed quantities in a similar way to the earlier discussion for QED. The most important electroweak process studied at LEP during 1990–5 was fermion pair production by electron-positron annihilation via a virtual photon or Z boson propagator. This data is virtually completely dominated by the Z boson exchange. The corresponding lowest order diagram for this process is shown in figure 1.3(a). At the Born level, this process receives separate contributions from the pure photon exchange, from the Z exchange, and from the interference between the two diagrams. The total cross-section for the photon exchange is predicted to be proportional to the inverse of the square of the centre-of-mass energy of the electron-positron collision. The contribution from the Z exchange is dominated by the Z resonance, and the total cross-section, as a function of the centre-of-mass energy, is described by a Breit-Wigner centred at the mass of the Z boson. The cross-section for the process $\mathrm{e}^+\mathrm{e}^-\to\mu^+\mu^-$ as a function of the centre-of-mass energy is shown in fig-

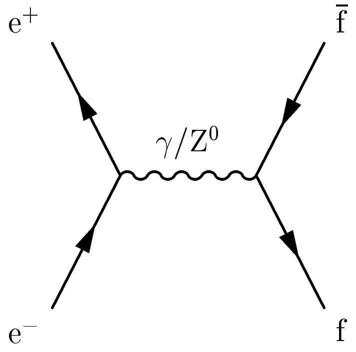

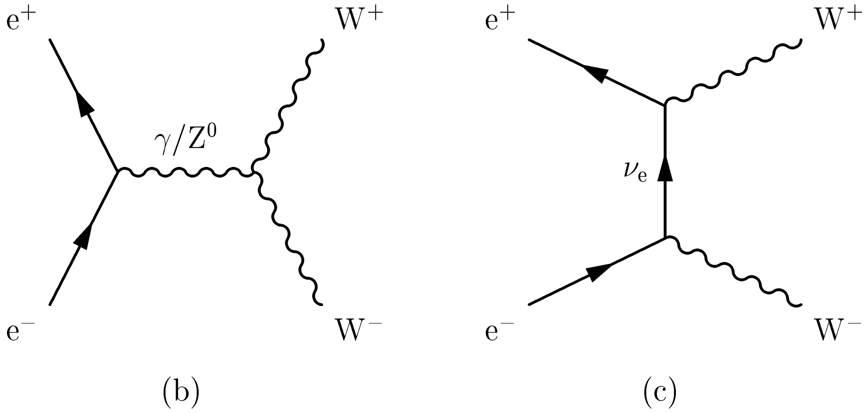

Figure 1.3: The Feynman diagram for the process $e^+e^- \rightarrow f\bar{f}$ via (a) the s-channel exchange of a virtual photon or Z boson and (b) for the process $e^+e^- \rightarrow WW$ via the s-channel exchange of a virtual photon or Z boson, or (c) the t-channel exchange of an electron neutrino.

ure 1.4(a). The theoretical predictions, obtained using a package called ZFITTER [14] which includes radiative corrections from higher order diagrams, is shown together with the Born level prediction in which only the lowest order Feynman diagram is considered.

After 1995, the centre-of-mass energy at LEP was increased enabling the study of W-pair production. At tree level this takes place via three diagrams, the so called s-channel exchange of a photon or Z boson, or via the so called t-channel exchange of an electron-neutrino as shown in figures 1.3(b-c) and are referred to as the charged current (CC03) diagrams. The W bosons decay hadronically or leptonically, but there are other processes which can give the same final states. The contributions from these CC03 diagrams can be calculated using Electroweak Theory and the total cross-section for the process $e^+e^- \rightarrow W^+W^-$ as a function of the centre-of-mass energy is shown in figure 1.4(b). The theoretical predictions, including radiative corrections, are obtained using the GENTLE [15] package, though other packages such as RACOONWW [16] and YFSWW [17] can also be used. The predictions in which some of the CC03 diagrams are omitted are also shown. The expectation for only ν_e exchange, where no coupling occurs between three gauge bosons, compared to the measured values [18], confirms that triple gauge boson couplings, also called TGCs, are present in nature. It also demonstrates the increasing sensitivity of LEP data to these vertices with increasing centre-of-mass energy.

The spontaneous symmetry breaking described earlier, which enables the bosons to acquire mass, is described by the Higgs mechanism. This introduces an additional scalar field called the Higgs field with which the gauge fields interact, the strength of this interaction is proportional to their mass. A consequence of this is that a new scalar particle, called the Higgs boson, is predicted, yet its mass is not. A current goal of experimental particle physics is to discover the Higgs boson. Direct measurements using the most recent LEP data have set a lower limit of $113.5\,\mathrm{GeV}/c^2$ at the 95% confidence level although a 2.9σ excess of events consistent with the production of a Higgs boson has been observed [19]. These results are under heavy scrutiny and the running of LEP was extended in an attempt to clarify the situation.

LEP has been particularly successful at testing the local gauge invariant properties of the Standard Model. It has been able to measure extremely precisely some of its free parameters such as the masses, widths and branching ratios of the W and Z bosons. A precise measurement of the width of the Z resonance enables the number of light neutrino species, N_ν, arising from the invisible decay of the Z boson, to be measured. The value, $N_\nu = 2.9835 \pm 0.0083$ [20], is consistent with only three fermion generations. Furthermore, the decay branching ratios and forward-backward asymmetries are important for measuring the couplings between the fermions and the massive bosons.

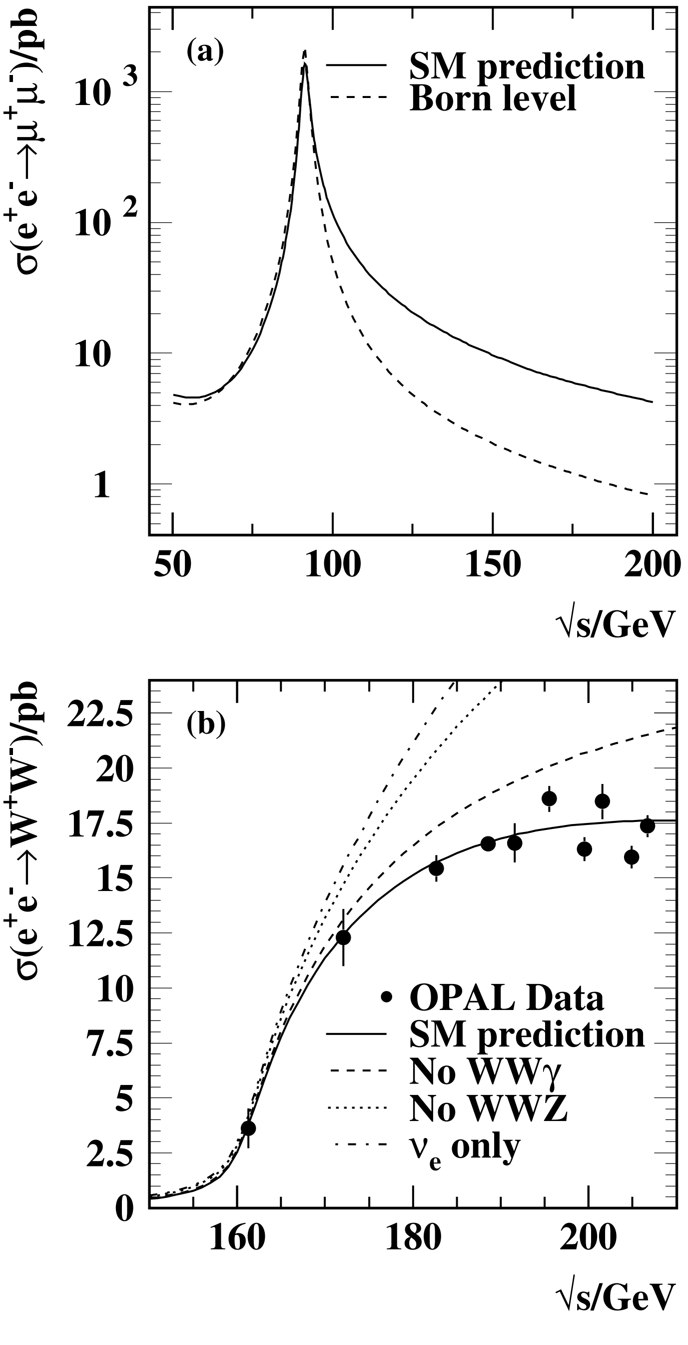

Figure 1.4: The cross-section as a function of the centre-of-mass energy, $\sqrt{s}$, for the electroweak processes (a) $\mathrm{e^+e^-}\!\to\!\mu^+\mu^-$ and (b) $\mathrm{e^+e^-}\!\to\!\mathrm{W^+W^-}$. The Standard Model predictions for muon pair production is obtained using ZFITTER, and this is shown together with the Born level prediction excluding radiative corrections. The Standard Model predictions for W-pair production is obtained using GENTLE. The OPAL measurements are shown with the expected results *excluding* some of the CC03 vertices.

1.4 Beyond the Standard Model

The current Standard Model theory of the particles and their interactions is based on the $SU(2)_L \otimes U(1)_Y \otimes SU(3)_C$ group. Despite its great success at predicting experimental results, it is not generally viewed as the final theory. The reason for this lies in its complex structure, the large number of free parameters which need to be measured to make it work, and its failure to explain certain observations. For example, the Standard Model is unable to explain the masses of the fermions and the Higgs boson, the mixing between the quarks, the presence of three generations of particles and the violation of parity in the weak interaction. In the same way that Newtonian mechanics is a low energy approximation of relativistic mechanics, the Standard Model may be a part of a greater theory. There are a number of extended and alternative theories being developed which offer solutions to some of these problems and these theories sometimes predict the existence of additional particles which may be observed at current energies. The search for such particles, which may demonstrate new physics phenomena beyond the Standard Model, is an active area of experimental investigation.

The most obvious shortfall of the Standard Model is its omission of gravity which is problematic as attempts are made to unify the forces. At much higher energies than those accessible by accelerators in the near future, the strengths of the couplings for the different forces is expected to converge, this suggests some underlying principle governing the behaviour of all of the forces. The so called 'Grand Unification Theories' offer possible mechanisms for this to happen, but none of them have predictions which are testable at current energies. A more testable theory, and one which is currently most theoretically favoured, is that of Supersymmetry (SUSY). The simplest is the Minimal Supersymmetric Standard Model (MSSM) in which there exists a symmetry between the fermions and the bosons, and so each known particle has a superparticle partner. So far there have been no indisputable confirmations of phenomena which cannot be incorporated into the Standard Model and so it continues to be the best description of the particles and their interactions.

Chapter 2

Experimental Framework

The analyses presented in this thesis make use of data collected by the OPAL detector which records events produced by the LEP accelerator. OPAL is one of four large experiments installed at the LEP accelerator at CERN. This chapter begins with a description of the chain of accelerators which deliver electrons and positrons to LEP, and the LEP accelerator itself. The OPAL detector is then described with particular attention given to its various components and to some of the physical principles involved in detecting the particles. Finally, the tools used to process the data generated by the events are introduced.

2.1 LEP Collider

The LEP (Large Electron Positron) machine [21, 22] is a circular synchrotron accelerator with a circumference of 26 659 m. It is situated inside an underground tunnel of diameter 3.8–5.5 m which is at a depth of between 51 m and 143 m below the surface. It straddles the French-Swiss border near to Geneva in Switzerland, extending from the Jura mountain range in French territory to the suburbs of the city of Geneva. The beams consist of bunches of electrons and positrons circulating in opposite directions around the machine inside an evacuated beam pipe, this reduces beam losses due to collisions with gas molecules. They cross at eight interaction points around the ring, and at four of the points are situated experimental detectors which are designed to record the products of these e^+e^- collisions.

LEP was designed to accelerate and collide beams at centre-of-mass energies in the range 80–200 GeV [23]. Its construction began in 1983 and the first circulation of a beam around LEP took place on 14 July 1989. The first collisions between electrons and positrons took place on 13 August 1989, and on the same day the first Z event was seen by the OPAL collaboration. In the period until October 1995, LEP collided beams at and around the energy of the Z boson (~ 91 GeV), this phase of running is referred to as LEP1. In subsequent years, the so-called LEP2 phase, LEP was upgraded to enable the centre-of-mass energy to be increased. During the year 2000 running a great effort has been made to extract the maximum possible centre-of-mass energy.

During a typical year of running, LEP operates between about April and November since the cost of electricity during the winter is too high. The winter period provides an opportunity to perform maintenance and upgrades to the accelerator and detectors, but during the rest of the year much of the time is spent providing physics events for the experiments. During this period the time is shared between filling the accelerator with electrons and positrons, accelerating them, and keeping the beams in high energy collision. The time spent in each mode of operation depends on many factors, in particular the energy of the particles and the beam currents. During data taking at LEP1, a single fill of leptons may provide up to 18 hours of physics events, whereas at 200 GeV the fills may only be up to 3 hours in duration, this makes the 1 hour of LEP filling and acceleration time a much more significant proportion of the running time. Following the decommissioning of LEP in 2000/1, the LHC (Large Hadron Collider) will be built inside the present tunnel producing proton-proton collisions at a centre-of-mass energy of 14 TeV.

2.1.1 LEP Injector Chain

Before reaching collision energy, the particles must first be collected and then accelerated, this is performed in a series of steps using a sequence of accelerators called the 'injector chain'. The principle used to accelerate the charged particles is the same in all cases. The charged particle is subject to a potential difference, and in practice this is provided by a travelling electromagnetic wave. A schematic diagram of the LEP accelerator and injector chain is shown in figure 2.1.

- Electrons and positrons are produced by the LIL (Lep Injector Linac) which consists of two LINAC's (LINear ACcelerator). Electrons are produced initially by thermionic emission from a heated filament and are accelerated to 200 MeV by the first LINAC. Positrons are created from this high intensity beam by photonic e^+e^- pair production in a tungsten target and they are then separated by a magnetic field. The bunches of electrons and positrons are accelerated by another LINAC to 600 MeV.

- The particles are then directed into the 126 m circumference EPA (Electron Positron Accumulator) storage ring. The particles circulate at 600 MeV until a sufficient number of particles have been accumulated.

- The bunches are then transferred into the first of two synchrotron machines, called the PS (Proton Synchrotron). This is 630 m in circumference and accelerates the electrons and positrons to 3.5 GeV.

- Finally, before injection into LEP, the bunches of particles enter the second, larger, synchrotron called the SPS (Super Proton Synchrotron) where they are accelerated to an energy of 20–22 GeV. The SPS is 6.9 km in circumference, and before LEP was built it was the largest accelerator at CERN, used for proton-antiproton collisions. It is still used to accelerate protons for fixed target experiments as well as for final pre-acceleration for LEP.

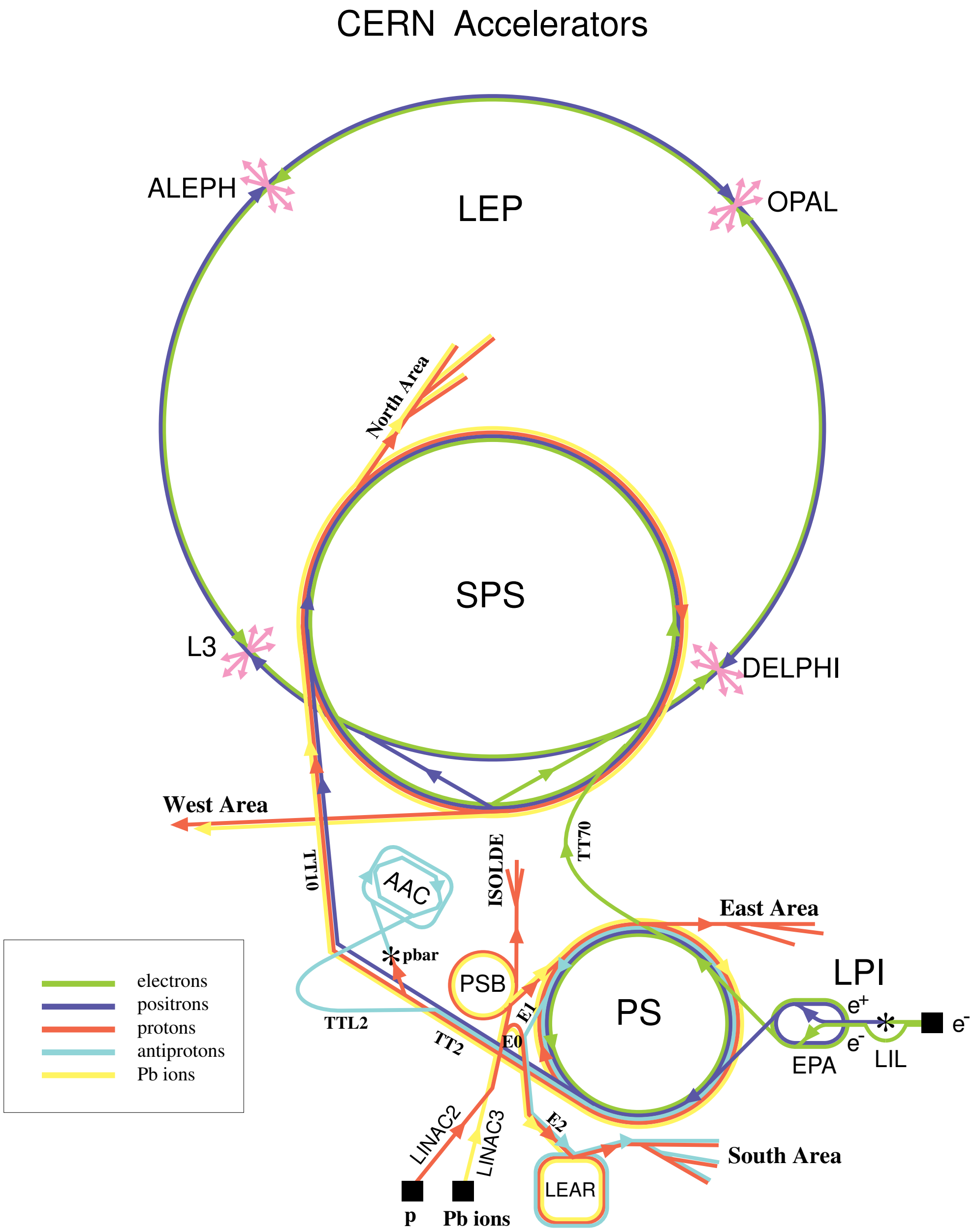

LEP: Large Electron Positron collider
SPS: Super Proton Synchrotron
AAC: Antiproton Accumulator Complex
ISOLDE: Isotope Separator OnLine DEvice
PSB: Proton Synchrotron Booster
PS: Proton Synchrotron
LPI: Lep Pre-Injector
EPA: Electron Positron Accumulator
LIL: Lep Injector Linac
LINAC: LINear ACcelerator
LEAR: Low Energy Antiproton Ring

Rudolf LEY, PS Division, CERN, 02.09.96

Figure 2.1: A diagram of the LEP accelerator and injector chain.

2.1.2 LEP Accelerator

During normal operation, LEP circulates bunches of electrons and positrons in opposite directions around the machine. There are four bunches per beam, referred to as $4+4$ mode, although in some of the LEP1 running there were eight bunches per beam, some with bunch trains. The bunches contain of the order of 10^{11} particles each, and they circulate around the ring 11 246 times per second. The particles need not only to be accelerated and maintained at high energy, but also constantly kept in orbit.

When light charged particles are accelerated along a curved path they undergo large energy loss through the emission of synchrotron radiation. The synchrotron radiation energy loss per revolution, ΔE, is given by

$$\Delta E = \frac{4\pi}{3}\frac{e^2\beta^2\gamma^4}{R},$$

where e is the magnitude of the charge of the electron, β is the particle velocity as a fraction of the speed of light, $\gamma = (1-\beta^2)^{-1/2}$ is the Lorentz factor, and R is the radius of curvature of the trajectory. For high energy electrons and positrons

$$\Delta E \propto \frac{E^4}{R},$$

where E is the energy of the particle. At LEP, the particle energy loss is approximately 128 MeV per orbit at 45 GeV, rising rapidly as the energy of the beam is increased. The beam must be accelerated not only to replace the energy which is continuously lost from it, but also to increase its centre-of-mass energy. Only a tiny fraction of the energy delivered to the beam is actually used to increase its energy in a typical 10 GeV step.

During the LEP1 phase, particle acceleration was provided by 128 copper radio frequency cavities which were powered by sixteen 1 MW klystrons. The klystrons, situated in short tunnels parallel to the main LEP tunnel, transferred energy to the cavities via waveguides. These cavities were able to provide 400 million volts of accelerating voltage per turn and they dominated the large power requirement of the LEP accelerator. From the end of 1995, as LEP moved into its higher energy phase of running, these copper cavities were gradually replaced by new superconducting niobium cavities. These are cooled by liquid helium to a temperature of about 4 K at which point the niobium becomes superconducting thus reducing the power consumption. During October 1995, 60 new accelerating cavities replaced 8 of the old ones, this allowed data to be taken at centre-of-mass energies of 130 and 136 GeV. During the winter of 1995–6 another 84 superconducting cavities were installed providing events at a centre-of-mass energy of 161 GeV. In the following years, more than 100 new cavities were added, replacing the old ones, and data has been recorded with centre-of-mass energies up to 202 GeV. For the beginning of the latest run, some of the old copper cavities were re-installed in an attempt to extract the highest possible beam energies from the machine. Data has now been recorded at a range of energies above 202 GeV, with the highest energy achieved so far of 209.0 GeV on 10 October 2000.

The beams are steered around LEP by 3 368 dipole magnets and are focused by 816 quadrupole, 504 sextuple and 700 correcting magnets. The deflection of the beam due to the dipole magnets produces appreciable synchrotron radiation which is undesirable near to the detectors. For this reason the LEP ring is not exactly circular, but is composed of a series of arcs with straight sections either side of the detectors. The dipole magnets are located at the arcs, thus suppressing the quantity of synchrotron radiation produced near to the experiments. A quadrupole magnet produces simultaneous focusing and defocusing of the beam particles along perpendicular axes transverse to the beam direction. A series of perpendicularly oriented magnets produces an overall focusing of the beam to give an optimised beam profile. The bunches must be tightly focused at the centre of the experiments, where the beams are brought into collision, in order to increase the rate of interaction between the electrons and positrons. At these points the beams are focused to 10 μm and 250 μm in the vertical and horizontal directions and they have a length of a few millimetres.

2.2 OPAL Detector

The OPAL (Omni Purpose Apparatus for LEP) detector [24] is one of four detectors at LEP together with ALEPH [25], DELPHI [26] and L3 [27]. OPAL was designed to enable the study of all detectable processes which are known to occur in electron-positron interactions at LEP energies. A cut-away perspective view of OPAL, giving an idea of its scale, is shown in figure 2.2. Its aim is to identify and measure the energies and momenta of the particles resulting from the interactions. This is achieved using a solenoid magnet and a series of detection modules, usually referred to as 'subdetectors'. OPAL is cylindrical in layout with the subdetectors arranged in concentric cylinders centred around the beam axis, called the 'barrel', and closed at the ends by the 'endcaps'. A diagram of a cross-section through the OPAL detector, showing this layout, is given in figure 2.3. The various layers of subdetectors produce signals in response to the passage of the particles propagating through them. Furthermore, the nature of the signals provides information about the type of particle which produced them. With this setup, and using information from all of the subdetectors together, OPAL is able to accurately reconstruct the events and identify the particles within them over a solid angle close to 4π.

The OPAL spatial positioning is defined using a right-handed Cartesian co-ordinate system. The z axis points along the electron beam direction which circulates anti-clockwise around LEP when viewed from above. The x axis lies in the plane of the LEP ring and points towards its centre. The y axis is therefore approximately vertically upwards, the deviation being due to the small incline of the LEP ring. The nominal interaction point is at the origin of this co-ordinate system. The polar angle, θ, is measured from the positive z axis. The use of $\cos\theta$ is common since it is a natural quantity to use when a solid angle is being considered. The azimuthal angle, ϕ, is measured from the x axis in the $x-y$ plane, and it is sometimes referred to as an $r-\phi$ measurement.

In the following sections a more detailed description is given of the individual subde-

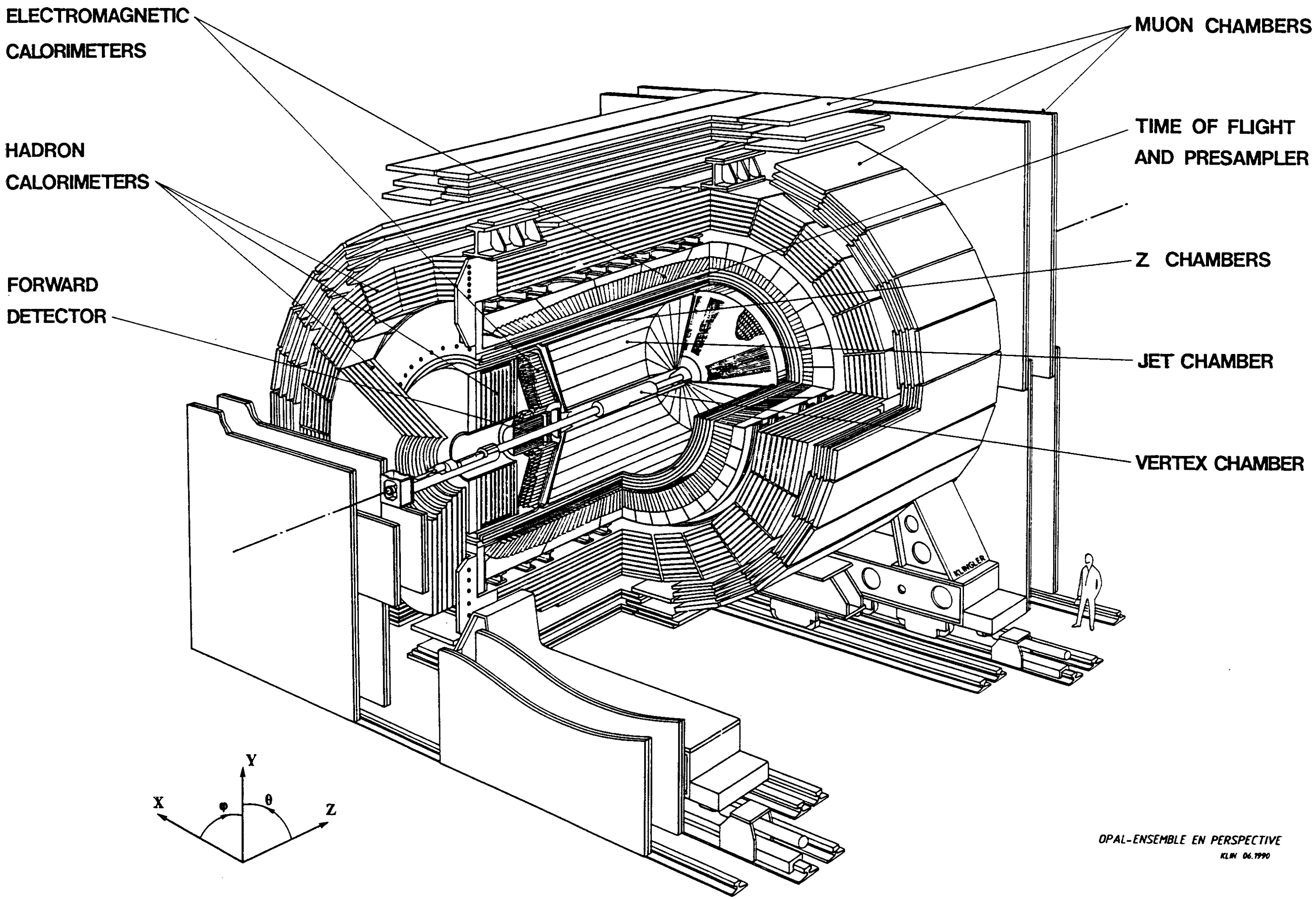

Figure 2.2: A cut-away perspective view of the OPAL detector.

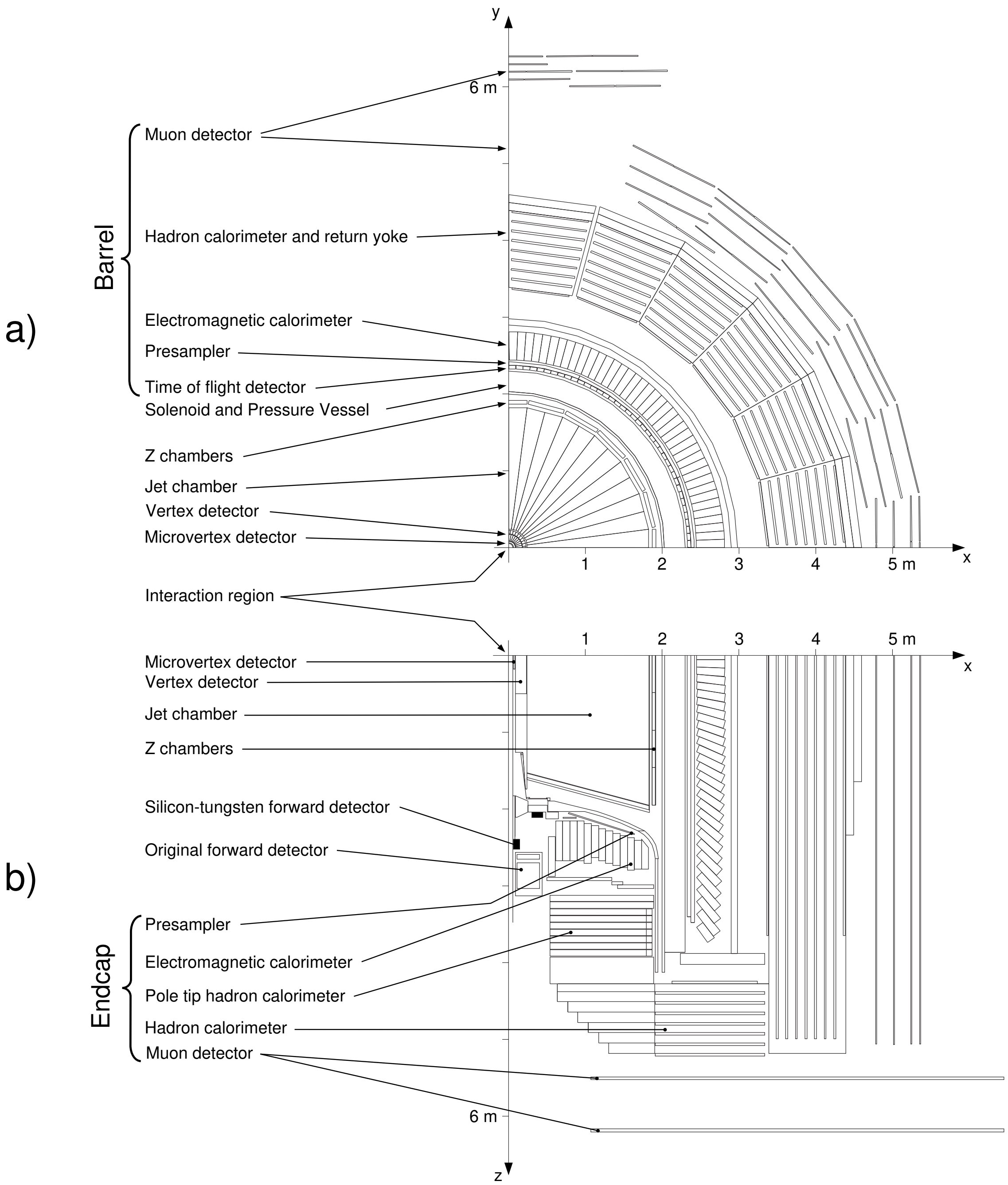

Figure 2.3: A diagram of a cross-section through the OPAL detector showing the subdetectors in (a) the barrel and (b) the endcap regions.

tectors which make up OPAL. The tour begins at the centre of the detector near to the interaction point where the particles created in the event originate. The tour follows the same sequence of subdetectors as encountered by the particles as they travel outwards through OPAL. In general, those subdetectors nearest to the interaction point aim to precisely measure the trajectories of the charged particles, without actually stopping them, as they traverse a magnetic field. This information is useful in reconstructing their momenta as well as for their identification. The particles are subsequently absorbed by the next layers of subdetectors which provide energy measurements and more particle identification information. Finally, the most penetrating particles are detected by the outermost layers of OPAL. Several other subdetectors, designed for specific functions such as measuring the timing of events or measuring the luminosity, are encountered on the tour. The angular coverage of the main subdetectors in OPAL are summarised in table 2.1.

2.2.1 Central Tracking Detectors

The innermost subdetectors of OPAL are devoted to measuring the trajectories of the outgoing charged particles near to the interaction point. They include the silicon microvertex detector, the vertex chamber, the jet chamber and the z chambers. The latter three instruments are of drift chamber design and are housed in a cylindrical pressure vessel, holding a pressure of 4 bar. The pressure vessel sits inside the main solenoid magnet of OPAL which produces a uniform magnetic field of strength 0.435 T throughout the volume of the central tracking detector, with field lines parallel to the z axis.

A charged particle propagating through a magnetic field experiences the Lorentz force which acts in a direction perpendicular to both the field lines and its direction of motion. The perpendicular component of the momentum, $p_\perp$, in GeV/c is given by

$$p_\perp = 0.3Br,$$

where B is the magnetic field strength in Tesla and r the radius of curvature of the

Subdetector	Angular coverage: Polar	Angular coverage: Solid angle
Central tracking detectors		
Silicon microvertex detector	$\mid \cos\theta \mid < 0.89$	86%
Vertex chamber	$\mid \cos\theta \mid < 0.95$	95%
Jet chamber	$\mid \cos\theta \mid < 0.98$	98%
Z chambers	$\mid \cos\theta \mid < 0.72$	67%
Electromagnetic and hadronic calorimeters		
Presampler barrel	$\mid \cos\theta \mid < 0.81$	98%
Presampler endcap	$0.83 < \mid \cos\theta \mid < 0.95$	
Electromagnetic barrel calorimeter	$\mid \cos\theta \mid < 0.82$	
Electromagnetic endcap calorimeter	$0.81 < \mid \cos\theta \mid < 0.98$	
Hadronic barrel calorimeter	$\mid \cos\theta \mid < 0.81$	97%
Hadronic endcap calorimeter	$0.81 < \mid \cos\theta \mid < 0.91$	
Hadronic Pole tip calorimeter	$0.91 < \mid \cos\theta \mid < 0.99$	
Muon detectors		
Muon Barrel detector	$\mid \cos\theta \mid < 0.72$	93%
Muon endcap detector	$0.67 < \mid \cos\theta \mid < 0.98$	

Table 2.1: The angular coverage of the main subdetectors at OPAL.

track in metres. A measurement of the position of the particle as it traverses this curved trajectory enables the momentum of the charged particle to be calculated. The direction in which the particle is deflected also reveals its charge.

The operation of the central tracking detectors at OPAL is based on the detection of the ionisation produced by the passing charged particles. The volume of the three drift chambers is filled with a gas mixture in which the charged particles leave a trail of ionisation. An electric field is configured inside this volume, normally by means of a potential difference between planes of wires. The ionisation drifts towards the anode wires under the influence of this field and induces signals upon them. The timing, positioning and magnitude of these signals are used to determine the properties of the particles which produced the ionisation. In the case of the silicon microvertex detector, the ionisation is detected directly. Each detected signal provides a single space-point measurement, called a 'hit'. These hits are linked together via a reconstruction procedure to produce a 'track' which approximates to the trajectory of the original particle.

- **Silicon Microvertex Detector**

  The silicon microvertex detector [28] was first installed in OPAL in 1991 and it was then improved in 1993 [29] and 1995 [30]. It was designed to provide a high precision measurement of the positions of the particles near to the interaction point. In particular it enables the reconstruction of events containing short lived particles, and particles with lifetime. An event containing a particle with sufficient lifetime for it to travel several millimetres before decaying is characterised by a set of particles which emerge from this decay point. This point is called the 'secondary vertex', and it is spatially separated from the interaction point which is also called the 'primary vertex'. The b quark is an example of such a particle and the silicon microvertex detector is important in identifying these types of events. Prior to the 1993 data taking period, the silicon microvertex detector was only capable of track direction measurements in the $r - \phi$ plane and provided no z direction information. After the silicon microvertex upgrade in 1993, full three dimensional track reconstruction was possible.

  A diagram showing a cross-section through the silicon microvertex detector is shown in figure 2.4. This detector sits between the beryllium beam pipe, which has an outer radius of 5.65 cm, and the drift chamber pressure vessel, with an inner radius of 8.0 cm. It consists of two concentric layers of silicon wafer modules called ladders, with an overall length of about 30 cm. The inner layer consists of 12 ladders, and the outer one of 15. The charged particles passing through the wafers create electron-hole pairs in the silicon. The electrons drift, and their charge is collected on microstrips which are implanted in the silicon wafers. The signal is read out from these strips. The wafers are oriented both parallel and

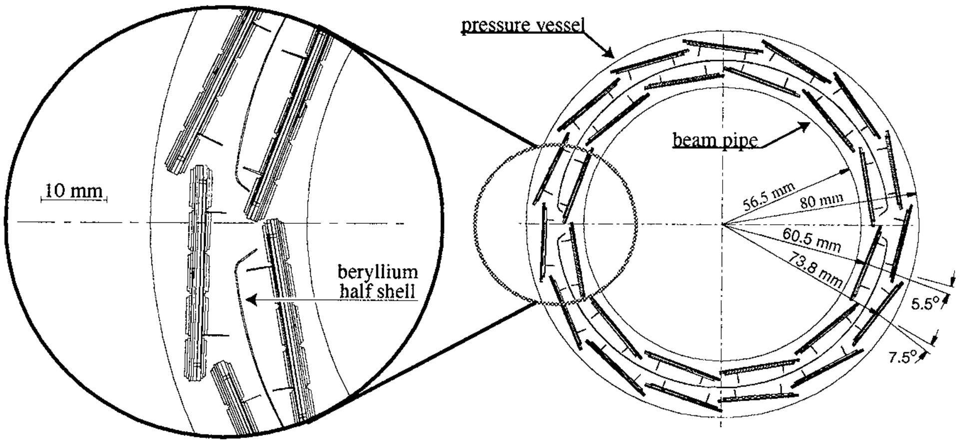

Figure 2.4: A diagram of the end view of the silicon microvertex detector.

orthogonal to the z axis and the reconstructed tracks have an overall resolution of about $10\,\mu$m in the $r-\phi$ plane and about $15\,\mu$m in the $r-z$ plane.

- **Vertex Chamber**

  The vertex chamber [31] surrounds the silicon microvertex detector covering a radius of 8.0 to 23.5 cm, and a length of about 1 m. It provides a precise measurement of the positions of tracks in the region close to the silicon microvertex detector, this allows the trajectories of tracks which were reconstructed by the latter to be matched to those reconstructed in the jet chamber beyond.

  This detector is cylindrical in design and consists of two concentric layers of drift chambers, with each layer divided into 36 sectors. The inner sectors house 12 wires oriented parallel to the z axis, these are called 'axial' wires, and in the outer sectors there are 6 wire at a $4°$ twist to the z axis, these are the 'stereo' wires. The stereo wires help to obtain a z co-ordinate measurement of the track positions. Tracks can be reconstructed with an overall resolution of about $50\,\mu$m in the $r-\phi$ plane and about $700\,\mu$m in the z direction.

- **Jet Chamber**

  The jet chamber [32] is the tracking chamber which occupies the largest region of space in the OPAL detector. It provides good spatial track resolution and particle identification over nearly all of the solid angle. The design of this detector was heavily based on a previous design tested at the JADE experiment at PETRA [33].

This detector is again cylindrical in design, it is 4 m long, with an inner radius of 23.5 cm and an external radius of 1.85 m. The volume of the detector is divided into 24 sectors, each containing a plane of 159 anode wires which are interleaved with potential wires. All of these wires run parallel to the z axis in lines running radially outwards from the beam direction. The anode wires have a radial separation of 10 mm and are slightly staggered with respect to the potential wire plane in order to resolve left-right ambiguities. A plane of cathode wires form the boundary between neighbouring sectors. The detector is filled with a gas mixture in which the ionisation due to the charged particles is produced. The precise ϕ position measurement is determined from the time taken for the ionisation to drift to the anode wire, and a charge division technique where the integrated charge collected at each end of the wire is used to determine the position along the z axis. Tracks in the jet chamber can be reconstructed with a spatial resolution in the $r-\phi$ plane of 135 μm and about 6 cm in the z direction.

One of the pieces of information which contributes to particle identification at OPAL is the $\mathrm{d}E/\mathrm{d}x$ measurement which describes the energy loss of the particle due to ionisation as it traverses the gaseous volume of the chamber. This value is derived from the measured charge collected at each space-point along the trajectory of the track. This depends upon the velocity of the particle, which combined with its measured momentum, allows the mass and hence the type of the particle to be derived. Figure 2.5 demonstrates how the measured $\mathrm{d}E/\mathrm{d}x$ value as a function of the particle momentum depends upon the type of particle. This technique, for example, enables the separation of electrons and pions in the momentum range $\sim 2.5 \rightarrow 13\,\mathrm{GeV}/c$.

- **Z Chambers**

The z chambers are the outermost tracking devices of the central detector. Their aim is to provide a precise measurement of the z co-ordinate of the tracks as they

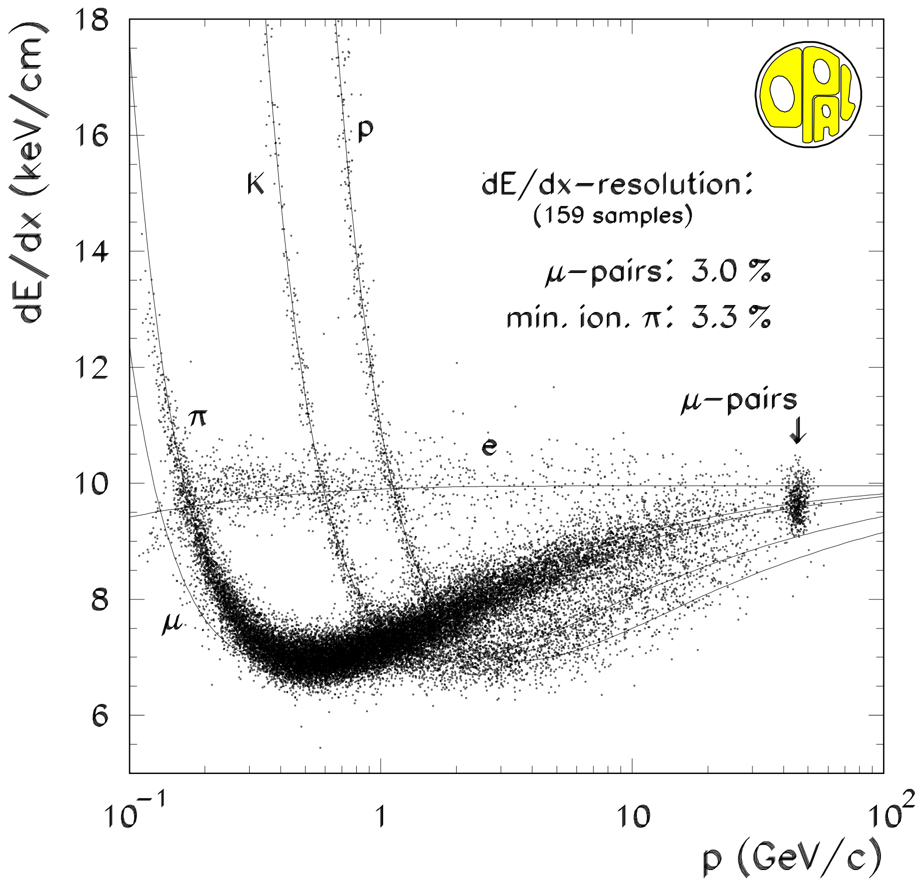

Figure 2.5: The distribution of the measured and expected $\mathrm{d}E/\mathrm{d}x$ energy loss per unit length for hadronic tracks and muon pairs as a function of particle momentum. The measurements shown were obtained using the jet chamber of the OPAL detector.

emerge from the jet chamber. The detector consists of 24 drift chambers 4 m long, 50 cm wide and 5.9 cm thick. Each chamber is divided along the z direction into 8 cells, each containing 6 wires oriented orthogonal to the z axis. Using this device, tracks can be reconstructed with a spatial resolution in the z direction of around 300 μm.

- **Magnet**

The magnet, which surrounds the central detector pressure vessel in the barrel region, is a self supporting, water cooled aluminium coil, carrying a current of 7 000 A. It generates an axial field with a strength of 0.435 T which is uniform to within $\pm 0.5\%$ throughout the volume of the central tracking detector. The iron of the hadronic calorimeter acts as the return yoke for the magnetic field.

- **Barrel Time-of-Flight Detector**

  Just outside the magnetic coil is a scintillator array called the time-of-flight system. This device measures the time-of-flight of the particles from the interaction point, it provides useful triggering information and is an important device for the rejection of background events not associated with e^+e^- interactions like cosmic rays or spurious interactions between the beam and residual gas or the beam pipe. It consist of 160 scintillation counters covering all of the $r - \phi$ plane and the region $|\cos\theta| < 0.82$. The scintillation light is fed out via perspex lightguides into photomultiplier tubes situated at each end of the devices. The time resolution of the detector estimated using di-muon events is 460 ps.

- **Tile Endcaps**

  The tile endcap subdetector complements the time-of-flight system in the endcap regions of OPAL. It was installed during the winter shutdown of 1995–6, enhancing the triggering capabilities in response to the higher background conditions expected at LEP2 energies. The detection modules are again layers of scintillator which are read out by wavelength shifting fibres to photomultiplier tubes situated outside the magnetic field of OPAL.

- **Minimum Ionising Particle Detector**

  This device is also a later addition to OPAL, having been installed for the start of 1997 [34]. It is designed to provide good time resolution and detection efficiency for single minimum ionising particles, such as muons, in the forward regions of OPAL. This detector is composed of four layers of 1 cm thick scintillator tiles which are divided into quadrants and octants in ϕ. The various layers are situated about 2.5 m away from the interaction point covering a polar angle of somewhere between 43 and 220 mrad.

2.2.2 Electromagnetic and Hadronic Calorimeters

The particles, after passing through the tracking chambers, encounter the calorimeter devices. These are designed to provide additional measurements of the particle energies and positions, particularly important for neutral particles such as photons which are not detected by the central tracking detectors. The calorimetry system is comprised of three main components, the presampler devices, the electromagnetic and the hadronic calorimeters. The latter two devices work in a similar manner by using absorbing material to cause the incident particles to undergo a process called 'showering'. In this process the particles lose energy by interactions with the material, in doing so they produce new particles which are detected. The localised regions of the calorimeters in which energy is deposited are sometimes referred to as calorimeter 'clusters'.

The electromagnetic calorimeter is made of lead-glass which acts as both the absorber and the detection medium. When electromagetically interacting particles with sufficiently high energy enter this material they undergo *electromagnetic showering* in which they interact with the charges in the penetrated material which results in the liberation of bremsstrahlung photons. These in turn can lead to electron-positron pair production and further photon emission and so on in a showering fashion. These particles are produced with velocities greater than the speed of light in the material and hence emit Čerenkov radiation which is then measured.

The hadronic calorimeter is constructed as alternating layers of absorbing material and detection devices which 'sample' the energy of the particles as they pass through. The absorbing material, which also serves as the return yoke of the magnetic field, produces *hadronic showering* which is similar in principle to the electromagnetic showering except that the cascade process is due to inelastic nuclear interactions between the incoming hadrons and the material. At high energy, this showering is characterised by multiparticle production and particle emission originating from the nuclear decay of excited nuclei.

There is already approximately two radiation lengths of material between the interaction point and the electromagnetic calorimeter which is mainly due to the pressure vessel and magnetic coil. Consequently, the electromagnetic showering will normally have started before the particles reach the calorimeters. In order to measure these showers, presampler devices situated immediately before the lead-glass calorimeter are employed. The electromagnetic calorimeter, which itself presents more than 20 radiation lengths of material, is intended to contain the electromagnetic showers. As such, the energy measured by it should correspond to the energy of the incoming electromagnetically interacting particle. The hadrons propagate through about 2.2 interaction lengths of material before reaching the hadronic calorimeter, and so the hadronic showering is also likely to have started before reaching it, probably within the electromagnetic calorimeter. Consequently, information from the two calorimeters together must be used to be able to correctly reconstruct and identify the particles producing the showers. The hadron calorimeter itself presents at least four interaction lengths of material to the incoming hadrons and the only detectable particles emerging from the calorimetry are the muons and possibly some remnants of the showers.

The lead-glass electromagnetic calorimeter consists of a barrel and two endcap components. The hadronic calorimeter consists of three parts, the barrel, two endcaps and two smaller endcaps called the pole tips.

- **Presamplers**

  The presampler barrel [35] consists of a cylinder of 16 chambers containing two layers of drift tubes with anode wires running parallel to the z axis. Signals are collected by cathode strips running along both sides of the tubes at $45°$ to the wires. The whole arrangement is 6.62 m in length and at a radius of 2.39 m. The presampler endcap is of a multiwire proportional counter design composed of 32 chambers arranged in 16 sectors covering all of ϕ.

  The spatial resolution achieved by these devices is about 10 cm and 5 mm in the z direction and $r - \phi$ plane respectively. This helps to improve the overall spatial and energy measurement resolution of the calorimetry system and provide additional γ/π^0 and electron/hadron discrimination.

- **Lead-Glass Electromagnetic Calorimeters**

  The total absorption lead-glass calorimeter has a barrel and two endcap components [36,37]. They measure the energy of electrons, positrons and photons, with energies greater than about 100 MeV, by detecting the Čerenkov light emitted by their showering as they pass through the lead-glass blocks. The lead-glass barrel consists of 9 440 such blocks about $10 \times 10 \times 37$ cm in size, accounting for 24.6 radiation lengths. They are arranged in a cylindrical array at a radius of 2.46 m with the long axis of each of the blocks pointing towards the interaction point. At the back of each block is a photomultiplier tube which collects the light.

  The endcap components consist of 1 132 lead-glass blocks arranged in a dome-shaped array all parallel to the z axis, and account for about 22 radiation lengths of material. The Čerenkov light is detected by vacuum photodiodes attached to the back of the blocks.

  The electromagnetic calorimeter system has an intrinsic energy resolution of $\sigma_E/E \simeq 0.2\% + 6.3\%/\sqrt{E}$ where E is the energy of the incoming particle measured in GeV. The overall resolution is somewhat degraded by the effect of the showering in the material before the calorimeter.

- **Gamma Catcher**

  This subdetector is designed to complement the lead-glass calorimeter by plugging the acceptance gap between the inner edge of the endcaps and the outer edge of the forward detectors. It consists of an arrangement of lead and scintillator layers.

- **Barrel and Endcap Hadronic Calorimeters**

  The barrel and endcap [38] hadron calorimeters are based on the same design, alternating layers of iron slabs and limited streamer tubes. In the barrel there are nine layers of tubes and eight layers of 10 cm thick iron, the endcap consists of eight layers of tubes and seven layers of iron. The barrel occupies the region around the beam axis at a radius of 3.4–4.4 m from the beam, with a length of 10 m. The endcaps are also 1 m thick at a radius of 1.9–3.3 m. The signals left by hadronic showers as they propagate through the layers are picked up by large pads and strips located on the outer and inner surfaces of the streamer tubes. The spatial resolution of muon tracks is limited to 10 mm by the anode wire spacing inside the tubes.

- **Hadronic Pole Tip Calorimeter**

  The hadronic pole tip calorimeter [39], having two components, extends the angular coverage of the hadron calorimetry towards the beam pipe on either side of the interaction point. It is similar in configuration to the barrel and endcaps, consisting of nine layers of iron, with the sensitive regions given by ten layers of multiwire proportional chambers. Readout is again by means of pads and strips located on the chambers.

2.2.3 Muon Detectors

The outer subdetectors at OPAL are the muon barrel and muon endcaps which efficiently locate $> 3\,\mathrm{GeV}$ muons over 93% of the solid angle. The muons also leave small energy deposits in the calorimetry as they pass through.

- **Muon Barrel**

  The muon barrel detector [40] consists of 110 large area drift chambers, it is 10.4 m in length with an external radius of about 5.5 m. A resolution in the $r-\phi$ plane of about 1.5 mm is achieved by using the drift time of the ionisation as the muon passes through the chamber. The z co-ordinate is determined by diamond shaped cathode pads with a resolution of $\sim 2\,\mathrm{mm}$.

- **Muon Endcaps**

  The muon endcap detector [41] consists of two planes of detector, positioned perpendicular to the beam pipe, about 5.5 m either side of the interaction point. It consists of four layers of limited streamer tubes which cover a total area of

$\sim 150\,\mathrm{m}^2$. In total there are eight $6 \times 6\,\mathrm{m}$ quadrants and four $3 \times 2.5\,\mathrm{m}$ patches with overlapping regions which achieve a resolution of about 1 mm.

2.2.4 Luminometers

The intensity of the $\mathrm{e^+e^-}$ beams when they are in collision is indicated by a parameter which is referred to as the instantaneous luminosity. This parameter depends upon factors such as the number of electrons and positrons per bunch, the number of bunches, their revolution frequency and the cross-sectional area of the bunches at the collision point. During data taking at a centre-of-mass energy of 91 GeV, the experiments typically see luminosities of $\sim 1.8 \times 10^{31}\,\mathrm{cm^{-2}\,s^{-1}}$, and the typical luminosities at LEP2 are $\sim 5 \times 10^{31}\,\mathrm{cm^{-2}\,s^{-1}}$. The expected event rate, $\mathrm{d}N/\mathrm{d}t$, for a reaction $\mathrm{e^+e^-} \to \mathrm{X}$ which has a cross-section, σ, is given by

$$\frac{\mathrm{d}N}{\mathrm{d}t} = \mathcal{L}\sigma,$$

where $\mathcal{L}$ is the measured luminosity. The cross-section is normally expressed in units of nanobarns (nb) or picobarns (pb) where $1\,\mathrm{barn} \equiv 10^{-24}\,\mathrm{cm}^2$. In fact the luminosity is integrated over time and expressed in terms of inverse picobarns ($\mathrm{pb^{-1}}$), so an integrated luminosity of $10\,\mathrm{pb^{-1}}$ is equivalent to expecting 10 events having a cross-section of 1 pb.

At the LEP experiments the luminosity is measured by counting small angle Bhabha events ($\mathrm{e^+e^-} \to \mathrm{e^+e^-}$). In these events the electrons and positrons in the beams scatter against each other electromagnetically. This is a pure QED processes and therefore its cross-section can be calculated precisely. Detectors are installed in these forward regions close to the beam pipe to detect the rate of this scattering process, and these are called the luminometers. At OPAL, in the region between 47 and 120 mrad, there is a clean acceptance for these events since the only obstruction comes from the beam pipe and 2 mm of aluminium from the central detector pressure vessel. The forward detector and the silicon tungsten luminometer are installed in these regions to provide the luminosity measurement.

- **Forward Detector**

  The two modules of the forward detector [24] are located at ± 2.6 m from the interaction point covering the very small angles of 40–150 mrad from the beam. They are made of 35 sampling layers of lead-scintillator sandwich representing about 24 radiation lengths of material. They also complement the electromagnetic calorimeter in the regions not covered by it, providing an energy resolution of $\sigma_E/E \simeq 17\%/\sqrt{E}$, where E is measured in GeV. The precision of the luminosity measurement from the forward detector is about 0.5%.

- **Silicon-Tungsten Luminometer**

  The installation of the silicon-tungsten luminometer [42] in 1993 improved the precision of the OPAL luminosity measurement to about 0.07%. This was necessary to achieve higher precision measurements using the data recorded at the Z resonance. The two modules of this detector are located next to the forward detector at 2.4 m from the interaction point covering an angle of 25–59 mrad from the beam. It consists of 19 layers of silicon detectors sandwiched between 18 layers of tungsten which acts as absorber. Its luminosity measurement is superior to the forward detector because the position of the scattered electrons or positrons can be measured more precisely. This is due both to the low lateral spread of electromagnetic showers in tungsten and to the use of the silicon layers to locate them.

2.3 Data Acquisition and Event Reconstruction

During LEP running, an electron-positron bunch crossing occurs every $22\,\mu$s at each of the four experiments. Each crossing may result in an interaction, and the particles resulting from it may travel outwards through the detector. The subdetectors at OPAL consist of a large number of different sectors, wires and channels, and each may produce some type of signal in response to the particles passing through it. The large number of signals together with the high beam interaction rate, means that an enormous amount of information needs to be collected and processed quickly. To do this a sophisticated system of electronics is employed, structured in several sequential steps including a trigger, an event builder and a filter. A software package is used for event reconstruction, and another system enables the transfer and storage of the final data.

- **Trigger**

  The time taken to readout the information generated by an event from the various subdetectors is typically around 5 ms. It is therefore not possible to record information from each bunch crossing. Conversely, not every bunch crossing results in an interaction, and even less likely an interaction which is worth recording. The trigger [43, 44] is responsible for selecting a set of events which are of interest and suitable for further processing, while also keeping the acquisition rate down to a manageable level. The trigger system must be fast so that it can respond to all beam crossings. It must also be efficient at retaining as many of the events which are of physical interest, in particular those in which a reaction has taken place. At the same time it must attempt to reject background events such as those from cosmic rays, spurious interactions between the beams and residual gas molecules inside the beam pipe, or even with the beam pipe itself, and also subdetector signals resulting from noise in their electronics systems.

  The trigger performs this function by imposing a set of rather simple criterion on some of the raw signals coming from various subdetectors. For example, the requirement for hits in a subdetector to be aligned helps to reject events caused by electronic noise, and the requirement that the signals have a time coincidence with the beam bunch crossing helps to reject cosmic rays. The result of the trigger is simply the acceptance or rejection of the event. The OPAL trigger has a very high efficiency for selecting interesting physics events and rejecting background events, this allows the LEP e^+e^- bunch crossing rate of 45 kHz to be translated into an event rate of about 10 Hz which can be handled by the data acquisition chain.

- **Event builder**

  When an event is selected by the trigger, a signal containing an event number is sent to each of the subdetectors. Each subdetector then reads out its data, reformats it to reduce its size, and passes it onto the OPAL event builder [45]. This system receives all of the information from the subdetectors and from it produces a single set of information for each event, this is called the event record.

- **Filter**

  The event record is transferred to a high-performance software based processor called the filter [46]. The filter looks at the whole event and functions as a monitor for the data. In addition, it acts as a second trigger by performing a classification of the events. This is used to identify a subset of uninteresting events which are discarded. The filter also compresses the event before recording it, this achieves a reduction in the data size by approximately a factor of five.

- **Event reconstruction**

  The information describing the selected event is mostly in the form of the raw numbers of hits and the magnitudes of electronic signals produced by the subdetectors. This information is converted into a set of quantities which are more useful for physics analysis by a software package called ROPE (Reconstruction of OPal Events) [47]. ROPE is responsible for linking together the information obtained from the various subdetectors to determine the characteristics of the complete events. For example, it reconstructs the trajectories, momenta and energies of the particles from the chain of raw hits observed in the central tracking detectors, and the energy deposits in the calorimeters. It also attempts to identify the particles. For example, the charged particles can be separated from the neutral ones by virtue of their appearance in the central tracking detectors. The different species can be separated by their $\mathrm{d}E/\mathrm{d}x$ measurement, the time-of-flight information, the pattern of energy deposits in the calorimeters, and by hits in the muon chambers.

The ROPE software makes use of a calibration database called OPCAL (OPal CALibration) to reconstruct the data correctly. This contains information such as the drift velocities in the drift chambers, the energy calibration of the calorimeters and timing offsets, as well as electronic pedestal and detector alignment information. The output of ROPE constitutes the DST (Data Summary Tape) [48] which is stored on disk. It is this information which is accessed when an offline physics analysis is being performed on data. After an event has been recorded, if a problem has subsequently been found with a subdetector which affects that event, or if the calibration information for the subdetector has been updated, the information can be readily incorporated into the DST by reperforming the reconstruction of the event with an updated OPCAL database.

2.4 Data Samples

During the operation of OPAL it has recorded more than $1\,\mathrm{fb}^{-1}$ of data. About $175\,\mathrm{pb}^{-1}$ of data was recorded during the LEP1 phase of running which provided very precise electroweak measurements of the Z boson. The LEP2 phase is focused on precise measurements of the W boson and on searches for new particles including the Higgs boson and supersymmetric particles. During this period, W-pair production has taken place at a range of centre-of-mass energies and the corresponding integrated luminosity recorded by OPAL is summarised in table 2.2. The progress in the collection of the

Year	1996		1997	1998	1999				2000
E_{CM}[GeV]	161	172	183	189	192	196	200	202	200–209
$\mathcal{L}$[pb^{-1}]	10	10	57	187	30	78	79	38	210

Table 2.2: The approximate integrated luminosity, $\mathcal{L}$, recorded by OPAL at each centre-of-mass energy, E_{CM}, during the LEP2 phase.

luminosity as a function of time within each year or LEP running is shown in figure 2.6. The data set for each LEP experiment comprises more than 4 million hadronic events at the Z energy and around 10 000 W-pair candidates.

2.5 Monte Carlo Event Simulation

In experimental high energy physics, the analysis of real data is normally performed in conjunction with that of simulated data. Simulated data is created in a series of steps beginning with a Monte Carlo event generator. The events are then treated so that a DST is produced which mimics the response of the OPAL detector to the events as if they were observed after real interactions. Simulated data provides a useful and important approach to performing tests and cross-checks on the data.

- **Monte Carlo Event Generators**

  A Monte Carlo event generator is a software package which embodies the physical process occurring in a particle interaction as described by theoretical and statistical models. There are several event generators written by various authors available for use in particle physics analyses worldwide. Typical examples of generators which are of particular importance in the analyses described in this thesis are those called JETSET/PYTHIA [49], EXCALIBUR [50] and KORALW [51,52]. The generators employed by the LEP collaborations calculate the e^+e^- interaction process described by the Standard Model and by other theories. Given a set of quantities such as the centre-of-mass energy of the collision and the particle masses and widths, the generator is able to create a set of events containing final state particles with the rates and configurations predicted by the theoretical models. The output consists of a set of four-vectors and types describing the final state particles produced in each simulated event.

Generators often specialise in calculating particular processes, such as W-pair or quark production. Some are more focused on the precise modelling of specific parts of the interaction, such as the TAUOLA [53] package for tau decays, and the hadronisation packages JETSET/PYTHIA and HERWIG [54] for the hadronisation of quarks. In performing an analysis, data from real events are often compared to those simulated by a range of generators since this helps to understanding the processes and the techniques being used to study them. Since these events reflect the underlying theory which was used to generate them, the use of events generated using a theory in which parameters have been adjusted provides a route to performing a measurement of those parameters.

- **Event Simulation**

The particles described by the four-vectors which are generated by the Monte Carlo generator would travel out from the interaction point through the various components of OPAL. The GEANT [55] software package propagates these particles out through the detector and simulates their interactions with the various materials. GEANT runs within a programme called GOPAL (Geant at OPAL) [56] which contains all of the information particular to the OPAL detector, namely its geometry and the types of materials which make up its volume. GOPAL simulates the response of the subdetectors to these outgoing particles and produces the raw signals analogous to that produced by a real physics event. This information is processed by ROPE in exactly the same way as for real data. The result is a DST analogous to that of the real data except in addition it contains all of the information describing the actual physics of the generated event. This includes the physical process which took place in the event, the true four-momentum and identity of each particle, and a pointer to the particle from which it originated.

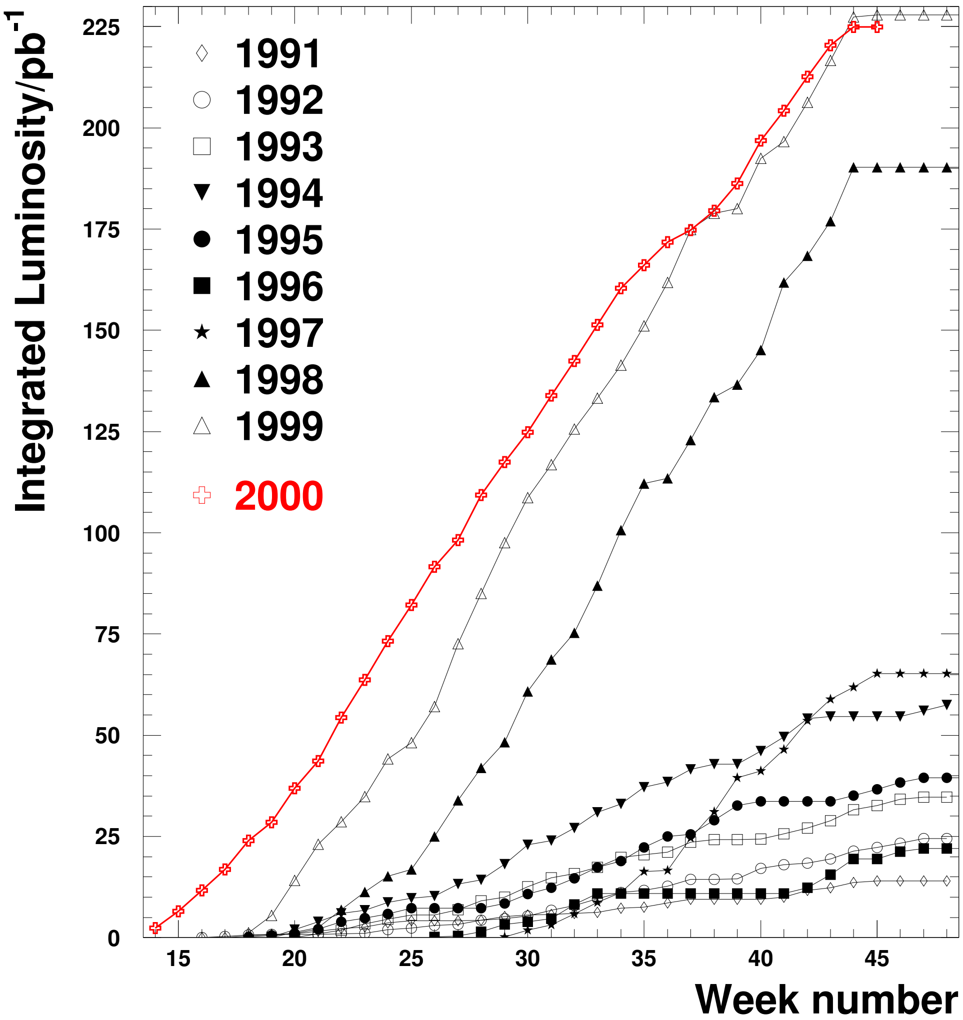

Figure 2.6: The development of the integrated luminosity recorded by OPAL as a function of time, for each year of LEP running.

Chapter 3

Inclusive b and B_J^* Reconstruction

During the LEP1 phase, events were recorded at centre-of-mass energies at and around the Z peak. About 70% of the Z bosons decay hadronically, producing quark-antiquark pairs of which about 22% are $b\bar{b}$ pairs. This data set comprises of more than four million hadronic Z decays and represents the data presented in this chapter.

The production of b quarks is investigated in several OPAL analyses, and this chapter concentrates on their inclusive reconstruction. The goal is to precisely reconstruct the direction and energy of the primary b quark from the Z decay, with the aim of using the scheme to measure the characteristics of the decays of orbitally excited B mesons, the so called B_J^* states. This measurement also requires the reconstruction to be highly efficient to maximise the use of the available data. If the reconstructed mass spectrum for these B_J^* resonances is well understood then it may enable the masses, widths, and relative decay rates of some or all of the states to be measured.

This chapter begins with a brief discussion of the physics of b quark decays, and then it describes their inclusive reconstruction which represents the main focus of the work. It then describes the nature of the orbitally excited B meson states and how their invariant mass distribution is reconstructed. Some of the results obtained applying these reconstruction techniques are presented.

3.1 b Physics Framework

The $q\overline{q}$ pairs produced in hadronic events undergo fragmentation and hadronisation. Quark confinement ensures that the primary $q\overline{q}$ pair are not observed alone. As the pair move apart, additional quark pairs are formed spontaneously from the vacuum. This can be visualised as a string connecting the parting q and $\overline{q}$ representing the colour field lines of the strong force of this QCD process. The string increases in length until it breaks, producing a new $q\overline{q}$ pair. The process continues and more $q\overline{q}$ pairs are created. The primary quark itself is said to 'dress' with one or two other quarks, so a primary b quark may form a b hadron such as a B^0, $\overline{B^0}$ or $B^{\pm}$. This process gives the event a characteristic signature consisting of two or more collimated groups of hadrons called 'jets'.

The b quarks are further characterised by the fact that they have significant lifetime which allows them to travel a mean distance of approximately 3 mm at LEP before decaying into lighter quark species. The decay itself yields further hadrons and so this process manifests itself as a set of particles emerging from a secondary vertex which is spatially displaced from the interaction point, or primary vertex, from which the fragmentation particles emerge. A secondary vertex provides a signature for the production of b hadrons.

The distance of closest approach between a reconstructed track and some point in space is known as the 'impact parameter'. To measure this, the track trajectory may need to be extrapolated backwards beyond the point at which the particle was first measured. In three dimensions, the impact parameter can be quantified into two separate values namely d_0 and z_0. The d_0 impact parameter is the distance of closest approach projected onto the $r-\phi$ plane. The z_0 impact parameter is the separation measured along the z axis. The impact parameter is normally signed relative to the primary vertex. If the reconstructed track trajectory crosses the axis defined by the direction of the b hadron on the same side of the primary vertex as the b quark itself, then the track is given a positive signed impact parameter. Conversely, the track is assigned a negative signed impact parameter if the track appears to cross this axis in the hemisphere away from the direction of the b hadron. Tracks from b hadron decays emerge from the secondary vertex and tend to have larger signed impact parameter values than those originating from other quark flavours or from the fragmentation process.

3.2 Inclusive b Reconstruction

To study b hadron spectroscopy, such as orbitally excited B mesons, a reconstruction of the four-momentum of the primary b hadron is necessary [57–64]. The inclusive reconstruction investigated in this chapter is relevant to the most recent B_J^* analysis [65], which utilises all of the $140\,\mathrm{pb}^{-1}$ of data recorded by OPAL during LEP1.

3.2.1 Event Selection and Reconstruction

The OPAL selection for hadronic events is based on the requirement for a high charged track multiplicity and the observation of energy clusters in the electromagnetic and hadronic calorimeters. Tracks are required to have at least 20 hits in the central jet chamber and their reconstructed trajectory must pass within 2 cm of the beam axis. Energy clusters in the barrel region are required to have a minimum energy of 100 MeV, while those in the endcap regions must have an energy of at least 200 MeV. A hadron candidate must have at least five tracks, at least seven energy clusters, and a total energy deposited in the lead glass calorimeters of at least 10% of the centre-of-mass energy. The efficiency for the selection of hadronic events is estimated, using simulated data, to be $(98.4 \pm 0.4)\%$ with a total background of less than 2%, arising mainly from tau pair and hadronic two-photon events. About four million hadronic events are selected from the OPAL LEP1 data. An example of a hadronic event reconstructed from OPAL data is shown in the upper part of figure 3.1. Also shown is a close-up of a reconstructed $\mathrm{b\overline{b}}$ event generated by Monte Carlo.

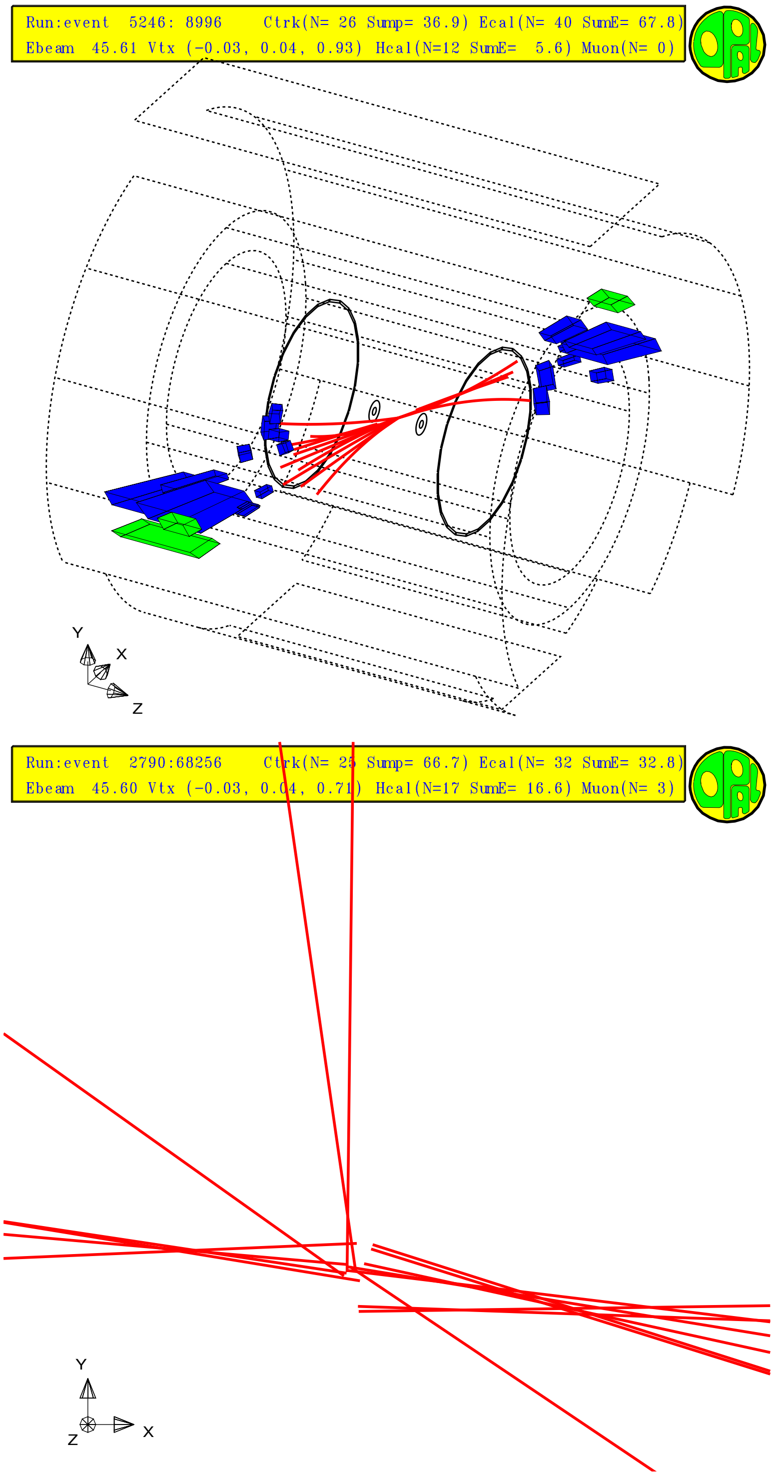

Figure 3.1: A reconstructed hadronic event recorded by OPAL (upper) with large energy deposits in the calorimeters denoted by the filled blocks, and a close-up of the interaction point of a reconstructed $b\bar{b}$ Monte Carlo event (lower) showing a displaced secondary vertex.

Once the event has been selected, the tracks and clusters which have been identified within it are grouped together by virtue of their spatial localisation by a jet finding algorithm. For this analysis the so called the 'cone' algorithm [66] is used since it provides the best b hadron energy and direction resolution compared to other jet finders. This algorithm defines a jet as a set of particles that have a total energy greater than a cut-off, ε, and momentum vectors that lie within a cone of half angle, R. The set of tracks and clusters which define the cone are found by means of an iterative procedure and the cone axis is obtained by the vectorial momentum sum of the particles. In this analysis $R = 0.65\,\mathrm{rad}$ and $\varepsilon = 5.0\,\mathrm{GeV}$. The two most energetic jets identified in each event are assumed to contain the b hadrons.

The significant lifetime of the b quark is exploited by using a 'b-tagging' algorithm which searches for particles with significant lifetime, such as b hadrons, within the jets. The silicon microvertex detector, which was described in section 2.2.1, is an important device for identifying such events since it is able to measure the positions of tracks close to the interaction point. The event is divided into two hemispheres defined according to a thrust axis determined from the directions of the tracks in the event. A b-likelihood is calculated for each hemisphere using three independent techniques, namely a lifetime tag, a high transverse momentum lepton tag and a jet-shape tag [67]. These are combined into a single discriminator whose value reflects the probability that the tracks and clusters resulted from a b hadron decay. The requirement for a large b-likelihood for the whole event is used to increase the b purity of the sample. This, together with requiring that the direction of the thrust axis, θ_{T}, satisfies $|\cos\theta_{\mathrm{T}}| < 0.8$, yields a $\mathrm{Z}^0 \to \mathrm{b}\overline{\mathrm{b}}$ event purity of about 96%, with a selection efficiency of about 49%, evaluated using simulated events. The two highest energy jets from each event in this sample provide about 750 000 b hadron candidates.

The position of the primary vertex is determined for each event by using the observed tracks to locate a common point. The fit procedure used for this includes two pseudo-tracks which constrain the vertex position to the average position of the beam spot. A secondary vertex finding algorithm is used to identify tracks which originate from a common displaced vertex. The so called 'build-up' algorithm [68] is used which forms a seed vertex from the two tracks with the most significant separation from the primary vertex. Tracks which have been measured with a separation significance from the primary vertex of more than 2.5 standard deviations are also taken as seeds. Vertex candidates which are separated from the primary vertex are found by considering the various pairings of seed tracks. Other tracks are added to this vertex nucleus providing that they match this vertex better than the primary vertex. The decay length is calculated for each vertex by means of a fit to the primary vertex position and the seed vertex position. Further criteria are used to select the best secondary vertex from the different candidates. The reconstructed secondary vertices arising from non-$\mathrm{b\overline{b}}$ events are dominated by c hadron decays.

The four-momentum of the b hadron is reconstructed using a procedure which employs a technique where a 'vertex weight' value is assigned to each track and cluster in the event [69]. The weight, whose value varies between zero and one, reflects the probability that the track or cluster was a product of the b hadron decay rather than from the fragmentation process. A weighted sum of the track and cluster four-momenta provides an estimate of the b hadron direction and energy. Of course, some of the particles in the event may have been created at the primary vertex without being a part of the fragmentation process, or others at some displaced vertex without being a decay product of the b hadron. The goal, however, is to try to assign individual tracks and clusters to one of the two vertices so that the four-momentum of the b hadron itself can be estimated.

The reconstructed b hadron momentum, $\vec{p}_{\mathrm{vtx}}$, is obtained using the expression

$$\vec{p}_{\mathrm{vtx}} = \sum_{i=1}^{N_{\mathrm{track}}} \omega_{\mathrm{track},i} \cdot \vec{p}_{\mathrm{track},i} + \sum_{i=1}^{N_{\mathrm{ecal}}} \omega_{\mathrm{ecal},i} \cdot \vec{p}_{\mathrm{ecal},i} + \sum_{i=1}^{N_{\mathrm{hcal}}} \omega_{\mathrm{hcal},i} \cdot \vec{p}_{\mathrm{hcal},i}, \tag{3.1}$$

where N_{track} is the number of tracks reconstructed in the jet, N_{ecal} the number of electromagnetic calorimeter clusters and N_{hcal} the number of hadronic calorimeter clusters. The appropriate vertex weight of each track or cluster, i, is denoted by ω_i, and each has a corresponding reconstructed momentum, $\vec{p}_i$. For tracks and clusters which are not in the same hemisphere as the b hadron candidate, ω_i is set to zero.

An estimate of the error on the momentum sum is calculated analytically by considering the weights of each of the contributing tracks and clusters in the sum. The uncertainty $\sigma(\vec{p}_{\rm vtx})_\psi$ in the reconstruction of the b hadron direction angle, ψ, using the momentum sum $\vec{p}_{\rm vtx}$ is obtained from the root mean square deviation of the angle relative to the reconstructed direction. Here, ψ represents either the polar angle, θ, or the azimuthal angle, ϕ, which were introduced in section 2.2. The value of $\sigma(\vec{p}_{\rm vtx})_\psi$ is given by

$$\sigma(\vec{p}_{\rm vtx})_\psi = \sqrt{\sum_{i=1}^{N}(1-\omega_i)\Delta\psi_i^2 + \omega_i\left[(1-\omega_i)\frac{\Delta\psi_i}{\omega_i}\right]^2}, \tag{3.2}$$

where $N = N_{\rm track} + N_{\rm ecal} + N_{\rm hcal}$ and $\Delta\psi_i$ is the change in the ψ angle of $\vec{p}_{\rm vtx}$ when the effect of track or cluster i is removed from the momentum sum $\vec{p}_{\rm vtx}$. The first term is the probability that track or cluster i did not come from the secondary vertex multiplied by the square of the error which its inclusion caused. The second term is the probability that this track or cluster did come from the secondary vertex multiplied by the square of an estimate of the error caused by only including a fraction ω_i of this track or cluster in $\vec{p}_{\rm vtx}$. This momentum error estimate can be used to improve the resolution of the reconstructed b hadron momentum, but no cut is applied to it at this stage.

The evaluation of the vertex weights is described in detail in the following section.

3.2.2 Vertex Weight Evaluation

The vertex weights have been estimated using algorithms which have been developed independently and used normally for different purposes. Four alternative methods are presented for estimating the track vertex weights, $\omega_{\rm track}$, and one method for the calorimeter cluster vertex weights, $\omega_{\rm ecal}$ and $\omega_{\rm hcal}$. Several algorithms employ artificial neural networks, sometimes referred to as 'NN' [70]. These aim to best combine a set of discriminators to highlight particular features of the data, in this case the output of the neural networks, with values varying between zero and one, reflect the probability that a given track is from the weak decay of a b hadron. The most powerful discriminators for separating b hadron decay products from fragmentation products include the track momenta and their impact parameter values relative to the primary and secondary vertices.

A comparison and evaluation of these various vertex weight estimation techniques has been carried out in order to determine their relative performances. A description of the different techniques is given followed by a comparison of the performance of the b hadron reconstruction achieved by each. Special attention is given to the quality of the resolution of the θ, ϕ and energy reconstruction since these are the most important elements when using the techniques in the inclusive b reconstruction for the B_J^* investigation. The samples of events which simulated the processes being investigated are inclusive Z decays generated using the JETSET Monte Carlo program [49]. These include about ten million mixed hadronic Z decays and two million $Z^0 \rightarrow b\bar{b}$ decays.

- **Impact Parameter Significance**

  In b hadron candidates in which there is a well reconstructed secondary vertex with a positive decay length, the track vertex weight, ω_{IP}, is calculated from the significance of the tracks to both the primary and secondary vertices [58]. This weight is given by

$$\omega_{\mathrm{IP}} = \frac{R_{\mathrm{sec}}(b/\eta)}{R_{\mathrm{sec}}(b/\eta) + R_{\mathrm{prim}}(d/\sigma)}.$$

  The variables b and η are the d_0 impact parameter and their error with respect to the secondary vertex, and d and σ are the same quantities with respect to the primary vertex. R is a symmetric function describing the impact parameter significance distribution with respect to the fitted vertex. Independent parameters are extracted for the primary and secondary vertices, R_{prim} and R_{sec}.

  The track vertex weight distribution for all tracks in a hemisphere with a reconstructed secondary vertex is shown in figure 3.2. The tracks arising from fragmentation only are also indicated. The distribution observed in simulated events agrees well with that observed in data. It can be seen that this weight method gives clear resolving power between the two classes of tracks. Some tracks are assigned to either the secondary vertex, large ω_{IP}, or to the primary vertex, small ω_{IP}. Those tracks with intermediate values are not unambiguously assigned to either vertex, either the track matches both vertices or neither of them. Tracks which cannot be assigned to either vertex are assigned a weight near to 0.5.

- **Neural Network 1**

  The track vertex weight, ω_{NN1}, is determined using an artificial neural network which is trained to discriminate between b hadron decay products and fragmentation tracks. The input variables to this artificial neural network, performed on a track-by-track basis are:

  - the scaled momentum, $x_p = p/E_{\mathrm{beam}}$,
  - the transverse momentum with respect to the jet divided by the total track momentum,
  - the d_0 impact parameter,
  - the z_0 impact parameter,
  - the signed d_0 impact parameter significance with respect to the primary vertex $(d_0/\sigma(d_0))$,
  - the signed z_0 impact parameter significance with respect to the primary vertex $(z_0/\sigma(z_0))$.

  This weight is calculated independently of any secondary vertex and therefore even in the absence of one. The track vertex weight distribution is shown in figure 3.2. It also indicates a good level of separation between the two track classes and demonstrates similar features to those of ω_{IP}.

- **Neural Network 2**

  The track vertex weight, ω_{NN2}, is determined using an artificial neural network trained using the same criterion as used to calculate ω_{NN1}. The inputs are also the same except for the second input variable, 'transverse momentum with respect to the jet divided by the total track momentum' which is replaced by the 'track rapidity relative to the estimated b hadron direction'. The rapidity, y, of a particle relative to an axis is given by

$$y = \frac{1}{2}\ln\left(\frac{E + p_{\mathrm{L}}}{E - p_{\mathrm{L}}},\right)$$

where E is the energy of the particle and p_{L} is its longitudinal momentum along the axis. In general, the directions of tracks from b hadron decays are similar to that of the primary b hadron. This alignment is reflected in the rapidity value, and so it provides a useful variable in separating b hadron products from fragmentation products. Tracks with negative rapidity are given a zero track vertex weight. As with ω_{NN1}, this weight is calculated independently of any secondary vertex. The track vertex weight distribution is shown in figure 3.2. The results are rather similar to those obtained for ω_{NN1} except for the absence of an excess of weights close to 0.5, arising from tracks which are not unambiguously assigned to either vertex. The track rapidity helps to differentiate between the two vertices.

- **Neural Network 3**

  The track vertex weight, ω_{NN3}, is determined using an artificial neural network trained using the same criterion as for ω_{NN1} and ω_{NN2}. For each track in the jet, the input variables are:

  - the total momentum,
  - the transverse momentum with respect to the jet containing the vertex divided by the total track momentum,
  - the d_0 impact parameter significance with respect to the secondary vertex,
  - the z_0 impact parameter significance with respect to the secondary vertex,
  - the d_0 impact parameter significance with respect to the primary vertex,
  - the z_0 impact parameter significance with respect to the primary vertex.

  A secondary vertex must have been reconstructed within the candidate jet in order to calculate ω_{NN3}. The track vertex weight distribution is shown in figure 3.2.

The separation is not as good as that obtained from the first three methods since the impact parameter significance is not included in its determination. This weight is not considered any further.

- **Cluster Rapidity Weight**

  The cluster vertex weights, ω_{ecal} and ω_{hcal}, which were introduced in equation 3.1, are assigned to each cluster detected in the electromagnetic and hadronic calorimeters in the hemisphere of the b hadron candidate. The weight is based on the rapidity of each cluster relative to an estimate of the b hadron direction. This estimate is initially taken from the first summation term of equation 3.1 using the track vertex weights alone, and then re-evaluated, including the effect of the clusters, in an iterative procedure. The value of the cluster rapidity weight is taken from the b hadron decay product purity, obtained from parameterising the corresponding quantity in simulated events as a function of the cluster energy. The possibility of double counting energy deposits in the calorimeter layers is avoided by including corrections which are returned by an algorithm which measures the flow of energy through the detector and attempts to match electromagnetic and hadronic calorimeter clusters to each other and to charged tracks reconstructed in the central tracking detectors [71].

The track vertex weights, ω_{track}, which enter equation 3.1 can thus be obtained from ω_{IP}, ω_{NN1} or ω_{NN2}, and the cluster vertex weights ω_{ecal} and ω_{hcal} are evaluated using the cluster rapidity.

3.2.3 Direction and Energy Reconstruction

The aim is to precisely reconstruct the direction and energy of the b hadron for all of the LEP1 data in all jets regardless of the presence of a well reconstructed secondary vertex. To further improve the four-momentum reconstruction, the different track vertex weights may be combined together. The individual track weight, ω_{a}, obtained

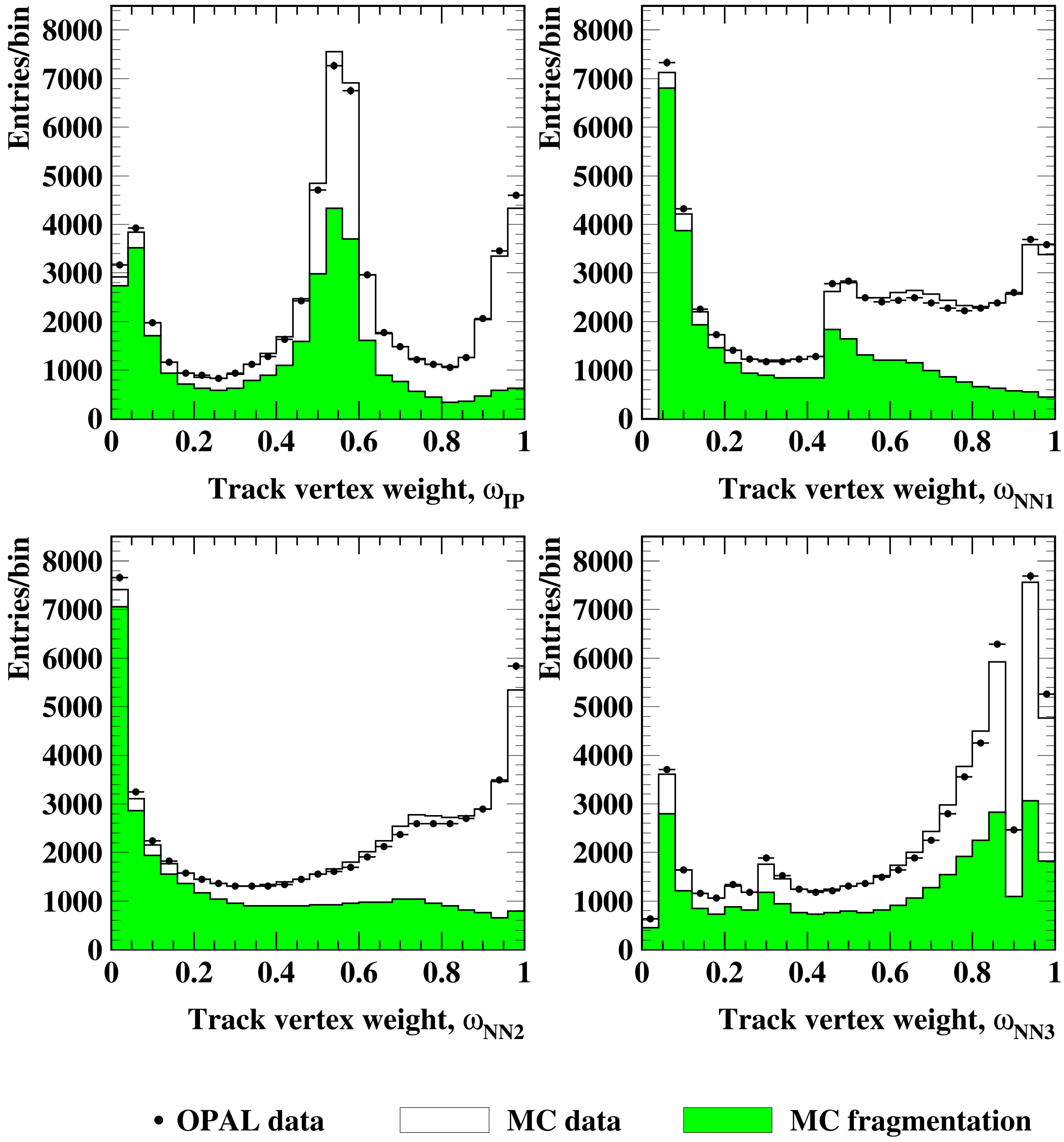

Figure 3.2: The distribution of track vertex weights for reconstructed tracks in real and Monte Carlo data. The distributions are for the weights estimated using the impact parameter significance, ω_{IP}, neural net 1, ω_{NN1}, neural net 2, ω_{NN2}, and neural net 3, ω_{NN3}. The Monte Carlo distribution for all the tracks, and the subset of fragmentation tracks, are shown.

by one method can be combined with the track weight, $\omega_{\rm b}$, from another, to give an overall track weight, $\omega_{\rm c}$, which can be calculated using

$$\omega_{\rm c} = \frac{\omega_{\rm a}\omega_{\rm b}}{(1-\omega_{\rm a})(1-\omega_{\rm b}) + \omega_{\rm a}\omega_{\rm b}}. \tag{3.3}$$

This new track weight then replaces $\omega_{\rm track}$ in equation 3.1. Equation 3.3 treats $\omega_{\rm a}$ and $\omega_{\rm b}$ as discriminators and not as true probabilities since they are correlated and would require a more complex technique to combine them correctly. One of the track vertex weight algorithms, $\omega_{\rm IP}$, relies on the presence of a secondary vertex in the jet, but since about 25% of the 750 000 or so real data b hadron candidates do not have a well reconstructed secondary vertex, the combined weight for these events is set equal to the weight from the technique not requiring the secondary vertex.

In jets where a secondary vertex has been reconstructed, a 'flight direction' vector for the b hadron can be calculated from the difference in the reconstructed positions of the primary and secondary vertices calculated in the $r-\phi$ plane and the z direction separately. The precision of this measurement is aided by the use of the silicon microvertex detector. This detector was upgraded during LEP1, as discussed in section 2.2.1, and so for data recorded prior to 1993, which represents about a quarter of the total LEP1 data, only ϕ direction information is available from this detector, whereas for the remaining data both θ and ϕ information is available. The flight direction provides a separate direction estimate from that obtained from the weighted momentum sums. In order to make best use of the two available estimators, the uncertainty on each must be calculated. The uncertainty on the flight direction estimate is calculated from the covariance matrices of the primary and secondary vertex positions. The uncertainty on the momentum sum was given in equation 3.2. The combined angle, $\psi_{\rm comb}$, obtained from these two reasonably uncorrelated estimated angles, ψ_1 and ψ_2, is given by the weighted average

$$\psi_{\rm comb} = \frac{\frac{\psi_1}{\sigma(\psi_1)^2} + \frac{\psi_2}{\sigma(\psi_2)^2}}{\frac{1}{\sigma(\psi_1)^2} + \frac{1}{\sigma(\psi_2)^2}} \tag{3.4}$$

where $\sigma(\psi_1)$ and $\sigma(\psi_2)$ are the uncertainties on the angles being combined. Furthermore, the uncertainty in the combined angle, $\sigma(\psi_{\rm comb})$, is given by

$$\sigma(\psi_{\rm comb}) = \sqrt{\frac{1}{\frac{1}{\sigma(\psi_1)^2} + \frac{1}{\sigma(\psi_2)^2}}}. \tag{3.5}$$

Again, as with equation 3.2, ψ represents either the polar angle, θ, or the azimuthal angle, ϕ. The value of $\sigma(\psi_{\rm comb})$ is a measure of the quality of the b direction reconstruction which can be improved by selecting small values. The optimal b direction can now be reconstructed using information from both the flight direction of the b hadron and also from the weighted sums of the tracks and clusters associated to it.

The energy of the b hadron is obtained by applying a beam energy constraint where the total energy in the event is set equal to the centre-of-mass energy, $E_{\rm CM}$. The total energy in the event is divided into two components, the total energy of the decay products of the b hadron candidate and the total energy of everything else, also called the 'recoil' energy. Assuming a two-body decay of the Z, the reconstructed b hadron energy, $E_{\rm B}$, is given by

$$E_{\rm B} = \frac{E_{\rm CM}^2 - M_{\rm recoil}^2 + M_{\rm B}^2}{2E_{\rm CM}}, \tag{3.6}$$

where the mass of the b hadron is set to the B meson mass, $M_{\rm B} = 5.279\,{\rm GeV}$. The recoil mass, $M_{\rm recoil}$, and the recoil energy, $E_{\rm recoil}$, are calculated in the same way as the weighted momentum sum of equation 3.1 except that the tracks and clusters are weighted by $(1-\omega_i)$. The initial estimate of the recoil mass, $M_{\rm recoil(old)}$, is calculated by assuming the pion mass for all charged particle tracks. To correct for undetected energy in the event, due for example to neutrinos, the recoil mass is scaled by the ratio of the expected energy of the recoil products to the measured value. The rescaled recoil mass, $M_{\rm recoil(new)}$, is then given by

$$M_{\rm recoil(new)} = M_{\rm recoil(old)} \cdot \frac{E_{\rm CM} - E_{\rm B}}{E_{\rm recoil}}. \tag{3.7}$$

This is substituted into equation 3.6 and the calculation of $E_{\rm B}$ is iterated.

The quality of the reconstruction can be determined from the resolution peak which is the distribution of the difference in the reconstructed quantity from its corresponding generated value in simulated events. This can be quantified by measuring the *full width at half maximum* (FWHM) and the *root mean square deviation from the mean* (RMS). The resolution curve is obtained from the sum of a wide Gaussian function and a narrow Breit Wigner function which is fitted to the central portion of the peak. The resolution peaks are constructed for the polar and azimuthal angles as well as for the b hadron energy. A better reconstruction method should yield both small FWHM and RMS values.

- **Direction Resolution**

  The FWHM and RMS values for the ϕ and θ resolution curves obtained using the different vertex weight algorithms are shown in table 3.1. The results using different weights combined show a small improvement in resolution compared to the algorithms used alone. Only the track vertex weight, ω_{IP}, requires a secondary vertex to have been reconstructed explicitly. Despite this extra information, the direction resolution achieved by it shows no gain compared to the other techniques since it contains no information about the track momentum. The flight direction measurement alone, which requires a secondary vertex to have been identified, offers a superior ϕ FWHM measurement compared to the other techniques. This resolution curve does, however, have a large RMS value resulting from jets in which the position of the secondary vertex has been particularly badly measured. Using this flight direction information significantly improves the ϕ reconstruction of the b hadron since the uncertainty on the measurement is used in combining the different angle estimates. The quality of the θ angle, applicable to 1993–5 LEP1 data, is poor compared to that obtained using the vertex weight technique. The use of this information is optimised by requiring that there are at least three hits recorded in the z planes of the detector.

- **Energy Resolution**

  The FWHM, RMS and mean values for the b hadron energy resolution curves obtained using the different vertex weight algorithms are shown in table 3.1. To improve the energy resolution a loose cut of a minimum reconstructed energy of 15 GeV is applied. The relative performance of the different methods and combinations are similar to those observed for the direction reconstruction. The energy resolution is best when the vertex weights are combined, and the three combinations are similar in performance. Since the flight direction information only improves the direction reconstruction, the numbers for E_{B} at the bottom of the table are unchanged. The offset of the mean energy from zero can be corrected for by the addition of the mean deviation to the reconstructed energy.

The results indicate that the three techniques which use combined weights together with information from the flight direction give the best quality b hadron direction and energy reconstruction. These three techniques are similar in performance to each other. The possibility of combining the most powerful discriminators into a new artificial neural network is favourable, but the gain in doing this is expected to be small. The inclusive b reconstruction using the combined ω_{IP} and ω_{NN2} together with the flight direction has been incorporated into an algorithm which is available for use in any OPAL analysis [72]. This algorithm returns for *any* given jet a reconstructed b hadron four-vector. This algorithm has been employed in the investigation of the decay of orbitally excited B mesons which is described in the next section.

Track vertex weight	Direction and energy resolution						
	ϕ [mrad]		θ [mrad]		E_{B} [GeV]		
	FWHM	RMS	FWHM	RMS	FWHM	RMS	Mean
ω_{IP}	49.9	47.0	46.7	45.3	12.1	6.5	-3.8
ω_{NN1}	44.3	43.0	42.2	40.8	9.0	5.3	-5.6
ω_{NN2}	44.2	41.1	41.1	39.1	9.0	5.2	0.1
ω_{IP} & ω_{NN1} combined	44.6	41.8	42.3	40.4	8.5	5.4	-0.6
ω_{IP} & ω_{NN2} combined	43.5	40.4	41.1	38.7	8.4	5.3	-0.2
ω_{NN1} & ω_{NN2} combined	42.6	39.7	40.4	38.4	8.6	5.0	1.3
Flight direction only	35.9	53.2	59.6	65.3	—		
ω_{IP} & ω_{NN1} with f.d.	33.0	50.0	41.2	47.0	Unchanged		
ω_{IP} & ω_{NN2} with f.d.	33.0	48.6	41.1	46.2			
ω_{NN1} & ω_{NN2} with f.d.	32.9	47.2	40.0	44.9			

Table 3.1: The FWHM and RMS results for the ϕ and θ direction and energy resolution for the inclusive b hadron reconstruction. For the b hadron energy reconstruction, E_{B}, the mean offset is also given. The results obtained using the different techniques for evaluating the track vertex weights are presented together with various combinations of the weights. The improvement in the direction resolution achieved using flight direction (f.d.) information is presented, the θ information is available only for LEP1 data recorded during 1993–5. This information does not affect the energy reconstruction.

3.3 B_J^* Framework

The name B_J^* refers to a family of four P-wave B meson states. Quarks possess a spin angular momentum of 1/2 and therefore the meson spin angular momentum, S, is either 0 or 1. The orbital angular momentum of the meson, L, depends upon the relative angular momenta of the quarks, $\mathrm{L} = 0, 1, 2\ldots$ The total angular momentum of the meson, J, is given by the vectorial addition of the spin and orbital angular momenta, $\vec{\mathrm{J}} = \vec{\mathrm{L}} + \vec{\mathrm{S}}$. A P-wave state is defined as having an orbital angular momentum of $\mathrm{L} = 1$ and therefore the total angular momentum can have the values $\mathrm{J} = 0$, 1 and 2. Furthermore, the $\mathrm{J} = 1$ case actually represents two separate states with the quark pairs having $\mathrm{S} = 0$ or 1. These four B_J^* states therefore have spin-parity values of $\mathrm{J^P} = 0^+$, 1^+, 1^+ and 2^+, and they are labelled B_0^*, B_1, B_1 and B_2^*, according to the convention set out by the Particle Data Group [3], where the subscript label gives the total angular momentum J value. These states are sometimes also referred to as B^{**}, and their analogous states where the b quark is coupled to an s quark is labelled B_{sJ}^*, but these latter states are not considered in this investigation.

The behaviour of hadrons containing one heavy quark, here the b quark is considered sufficiently heavy, is predicted by the Heavy Quark Effective Theory (HQET) [73]. In this theory the mesons are described by the spin of the heavy quark, $\mathrm{S_Q}$, the total angular momentum of the light quark $\mathrm{j_q} = \mathrm{S_q} + \mathrm{L}$ and the total angular momentum $\mathrm{J} = \mathrm{j_q} + \mathrm{S_Q}$. In these expressions $\mathrm{S_q}$ and L denote the spin and orbital angular momentum respectively of the light quark. In this framework the b quark is considered to be sufficiently massive that it is treated as being stationary relative to the other quark of the pair. The four B_J^* states are then grouped into two doublets corresponding to $\mathrm{j_q} = 1/2$ and $\mathrm{j_q} = 3/2$.

A B_J^* state decays via the strong interaction to an $\mathrm{L} = 0$ state which can be either a B^* ($\mathrm{J} = 1$) or a B ($\mathrm{J} = 0$). This is accompanied by the ejection of a pion. The B^* itself will decay electromagnetically into a B with the emission of a photon whose energy has been measured to be $45.78 \pm 0.35\,\mathrm{MeV}$ [3]. The B mesons will then decay weakly

State ($J^P_{j_q}$)	Predicted properties mass [GeV/c^2]	width [GeV/c^2]	decay mode	Monte Carlo values mass [GeV/c^2]	width [GeV/c^2]
B_0^* ($0^+_{1/2}$)	5.738	0.20-1.00	$(B\pi)_{\mathrm{S-wave}}$	5.750	0.300
B_1 ($1^+_{1/2}$)	5.757	0.25-1.30	$(B^*\pi)_{\mathrm{S-wave}}$	5.770	0.300
B_1 ($1^+_{3/2}$)	5.719	0.021	$(B^*\pi)_{\mathrm{D-wave}}$	5.725	0.020
B_2^* ($2^+_{3/2}$)	5.733	0.025	$(B^*\pi)_{\mathrm{D-wave}}$	5.737	0.025
			$(B\pi)_{\mathrm{D-wave}}$		

Table 3.2: Theoretical predictions for the masses, widths and dominant decay modes of the B_J^* states and the corresponding values used in the Monte Carlo generated samples.

into stable hadrons. From angular momentum and parity conservation arguments, only certain $B_J^* \to B^{(*)}$ transitions are allowed[a] and these are shown in figure 3.3. The 0^+ state can only decay to $B\pi$ via an S-wave transition, the $1^+_{1/2}$ to $B^*\pi$ via an S-wave transition, the $1^+_{3/2}$ to $B^*\pi$ via a D-wave transition, and the 2^+ state can decay to both $B\pi$ and $B^*\pi$ via D-wave transitions only. The total angular momentum changes of the S-wave and D-wave transitions are 0 and 2 respectively. Since an S-wave transition undergoes no change in angular momentum there is a large overlap between the initial and final states, the decay is expected to be rapid and the width of the resonance to be large. In contrast, resonances decaying only by D-wave transitions are predicted to be narrow [74]. The HQET predictions for the masses and widths of these states are summarised in table 3.2 [74–76]. Also in this table are the values which were used to generate the Monte Carlo events which simulate this process.

[a] $B^{(*)}$ denotes the state B^* or B.

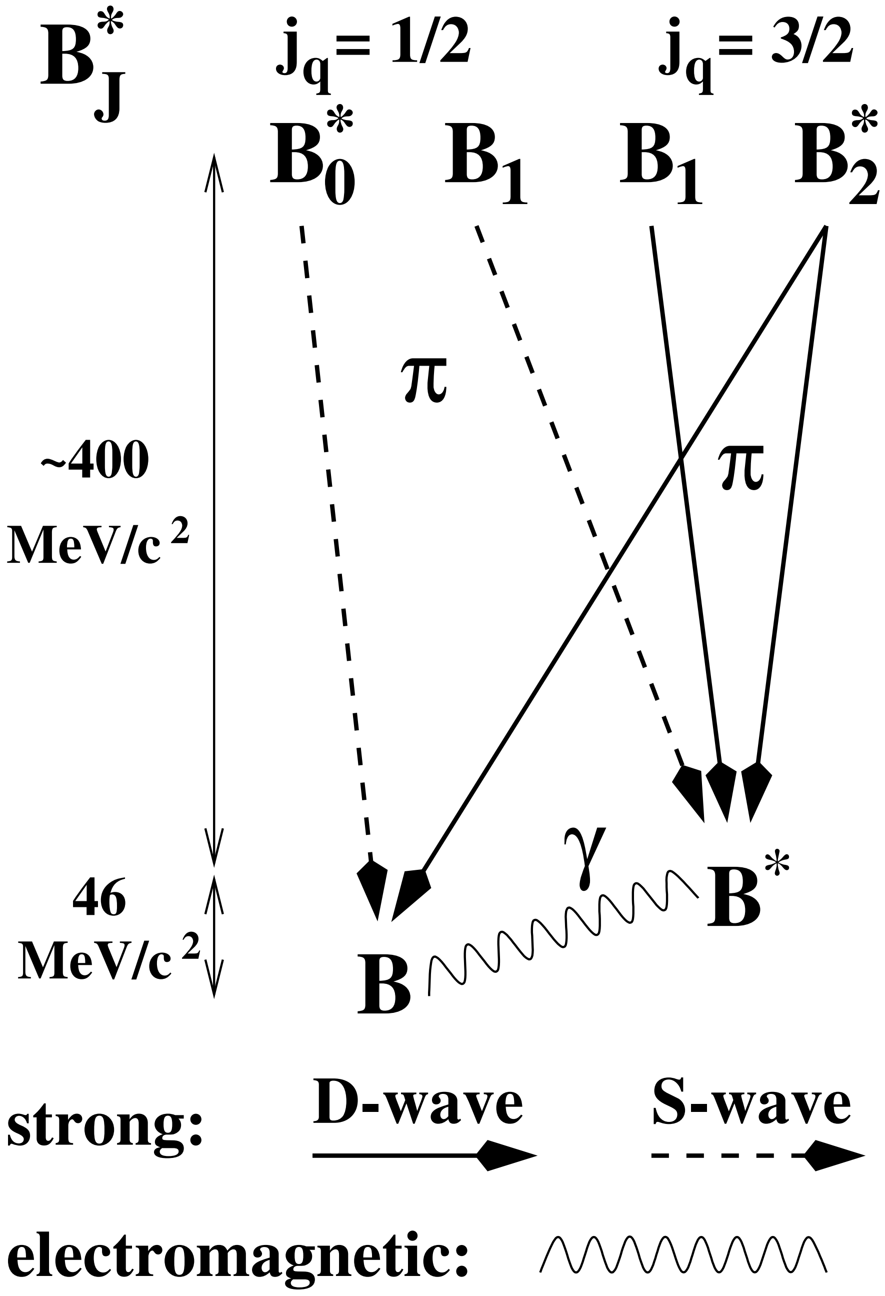

Figure 3.3: The four B_J^* states and their decays to the ground states B and B^*. The solid lines indicate D-wave transitions and the dashed lines S-wave transitions via single pion emission. The B^* decays to a B electromagnetically.

3.4 B_J^* Reconstruction

Following the creation of a B_J^* state from the primary b quark, it decays weakly by one of the allowed transitions to give a ground state B or B^* meson and a pion. If produced, the B^* itself emits a photon in its transition to a B. The jet of particles emerging from the primary vertex consists of the B meson, the so called 'transition' pion arising from the B_J^* decay, and many fragmentation products. The weak decay of the B meson gives rise to a group of particles which emerge from a secondary vertex. In summary, a B_J^* event is characterised by a hemisphere having a jet containing a secondary vertex with a transition pion originating from the primary vertex and a possible signal photon. In practice, the transition pion is difficult to distinguish from the fragmentation particles and most analyses do not look for the photon since it is even more difficult to identify.

Using the b hadron and transition pion candidates it is possible to reconstruct the invariant mass of the B_J^*. The structure of this invariant mass distribution is predicted theoretically and the expected relative masses and widths of the states, indicated in table 3.2, predict that the states will be very close together in mass and will overlap each other. This together with the limited resolution of the detector implies that the reconstructed invariant mass distribution of the various states will have a large overlap and therefore the detailed mass structure may not be resolvable. The theoretical predictions can, however, be used to provide assumptions which may help interpret the spectrum.

In most analyses performed to date [57, 60–62] the B_J^* mesons have been reconstructed in the $B\pi$ final state only. This has resulted in the observation of just a single peak in the invariant mass spectrum which is insufficient to resolve any substructure for the individual states. Furthermore, in this scheme the final state photon in the $B_J^* \to B^*\pi \to B\gamma\pi$ decay is not identified. This photon is expected to have an energy of $\sim 46\,\mathrm{MeV}$ and so in the case of the $B_J^* \to B^*\pi$ decays, part of the invariant mass spectrum is shifted to lower mass by this value.

In the most recent OPAL analysis the photon in the decay $B^* \to B\gamma$ is included in the treatment, but the B_J^* is not reconstructed in the $B\gamma\pi$ final state since the combinatorial background is too large. An attempt has been made to statistically separate the $B_J^* \rightarrow B^*\pi$ from $B_J^* \rightarrow B\pi$ transitions by searching for these photon candidates [65]. The total B_J^* sample is then divided into two samples, one enriched and one depleted in the decay $B_J^* \rightarrow B^*\pi(X)$. Using this technique a measurement of the branching ratio $BR(B_J^* \rightarrow B^*\pi(X))$ has been performed. The label $B^*\pi(X)$ is used since X is not explicitly excluded. This accounts for the small contribution expected from decays such as di-pion transitions into $B^{(*)}\pi\pi$, possibly via an intermediate state such as $\rho \rightarrow \pi\pi$ [76]. This value of $BR(B_J^* \rightarrow B^*\pi(X))$ provides further insight into the decomposition of the B_J^* states in the mass spectrum since the two states decaying to $B\pi$, namely B_0^* and B_2^*, can be separated from the other states which can only decay to $B^*\pi$. An interpretation of the invariant mass spectrum requires the background component to be precisely assessed which is particularly important since the difficulty in identifying the transition pion gives rise to a large *combinatorial* background. It should also be noted that the procedure only calculates the invariant mass using a single transition pion and so any di-pion decays, $B_J^* \rightarrow B^{(*)}\pi\pi$, will give rise to a low mass satellite peak since the second pion is omitted from the calculation of the invariant mass. This decay process has also being investigated using OPAL data [77].

Once the b hadron candidate has been reconstructed along with a candidate transition pion track, they can be combined to form the B_J^*. The reconstructed B_J^* mass is obtained from the invariant mass, $m(B\pi)$, which is given by

$$m(\mathrm{B}\pi) = \sqrt{m_{\mathrm{B}}^2 + m_\pi^2 + 2E_{\mathrm{B}}E_\pi - 2\vec{p}_{\mathrm{B}} \cdot \vec{p}_\pi}.$$

In this expression, m_{B} and m_π are the b hadron and pion masses, E_{B} and E_π are their reconstructed energies, and $\vec{p}_{\mathrm{B}}$ and $\vec{p}_\pi$ their reconstructed momentum vectors. These values for the b hadron are determined by the inclusive b reconstruction, and a transition pion must also be selected. The transition pion will emerge from the primary vertex and it is expected to lie within the candidate b hadron jet. Its properties are expected to be similar to those of the fragmentation particles which are mainly also pions. A loose pion selection is imposed by requiring that the measured $\mathrm{d}E/\mathrm{d}x$ energy loss of the particle due to ionisation in the jet chamber, discussed in section 2.2.1, is consistent with the expected value for a pion within 2.6 standard deviations. To suppress candidates arising from B decays, the track is required to come from the primary rather than from the secondary vertex by requiring that the combined ω_{IP} and ω_{NN2} track vertex weights, evaluated in section 3.2.2, are smaller than 0.9. The track with the largest longitudinal momentum with respect to the reconstructed b hadron direction is retained so that a single pion candidate is obtained for each B hadron candidate.

The event sample used for this investigation is the same as that used in the inclusive b reconstruction of section 3.2. It includes additional loose cuts on the uncertainty of the b hadron direction estimate which removed about 20% of the B candidates leaving a data sample comprising of about 570 000 jets with a b purity of 96%.

3.4.1 Background

The majority of entries in the invariant mass distribution are not from B_J^* decays where the genuine B^* or B candidate has been combined with the true signal transition pion, but rather from background. These sources of background can be characterised as follows:

- fake B_J^* candidates from events in which the primary quark was either light or a charm quark,
- fake B_J^* candidates arising from true b hadrons combined with a pion from the weak decay of the b hadron itself,
- fake B_J^* candidates formed by combining true b hadrons with fragmentation tracks which have not come from the B_J^* resonance.

In simulated events, the shape of the invariant mass distribution for the true background is very similar in shape to that including signal entries. It is therefore necessary to perform an accurate estimation of this background contribution in order to extract the signal. It is unfavourable to take the true background distribution from simulated events since the transition pion tracks are reasonably indistinguishable from the fragmentation tracks which are known to be poorly modelled. A solution is to try to obtain an estimate of the shape of the background using real data. If a good reproduction of the true background shape can be achieved using simulated events treated as data, then applying the same technique to real data can yield an equivalent background estimate. Only the reproduction of the *shape* of the distribution is important since the normalisation can be performed in the high mass region of the invariant mass spectrum, also called the sideband, away from where the B_J^* mass peaks are expected.

An understanding of the background shape and how to estimate it is a demanding aspect of the B_J^* analysis. Several different techniques have been attempted in previous OPAL analyses. The first OPAL B_J^* analysis [57] exploited the fact that the charges of the B jet and the transition pion are correlated. A sample of events suppressed in B_J^* was then extracted. As an extension to this technique, simulated events were used to combine the reconstructed charge and the error associated with it into a single value which reflects the probability that the vertex was due to a charged B meson [78]. An OPAL B^* measurement [58] made use of an anti b-tag in which the requirement for a jet to contain little or no lifetime information returned a sample of jets which have a lower b purity, and therefore a low B_J^* purity. This provides a sample which can estimate the background shape due to events in which the primary quark was light. Another OPAL analysis measuring the properties of $D^{*\pm}$ decays [79] which also decays via the emission of a transition pion, employed a technique in which the candidate transition pion which is selected to form the B_J^* is taken from another jet, either the other jet in the event or from another event. This candidate pion is rotated about the reconstructed primary vertex so that its direction relative to the b axis (or c axis in the case of $D^{*\pm}$) of the jet into which it is being rotated is the same as it was relative to the jet from which it was taken. In order to remove the correlation between a possible true B_J^* and signal pion, the pion direction is smeared. The candidate tracks which are from fragmentation should be reasonably unaffected by this smearing. This technique provided a good estimate of the background shape in B^*_{sJ} events but not for B^*_J [69].

For the analysis described here, the background estimate provided by simulated events was tested, and if necessary reweighted, by developing test samples which were strongly enhanced in the background source under study. In these samples the B^*_J signal was suppressed by about a factor of eight compared to the original B^*_J signal. These test samples addressed the three sources of background listed above separately by inverting various cuts in the original B^*_J selection.

3.4.2 Measurement of BR($B^*_J \to B^*\pi(X)$)

This and the following section reports a published OPAL paper which uses some of the techniques already described, and more details can be found in [65]. A model-independent measurement of $\mathrm{BR}(B^*_J \to B^*\pi(X))$ was performed by identifying photon candidates from the decay $B^* \to B\gamma$ to statistically separate the $B^*_J \to B^*\pi$ from the $B^*_J \to B\pi$ transitions. These photons have an energy of about 46 MeV in the rest frame of the B^*, corresponding to a photon with an energy of less than 800 MeV in the detector, and so the selection was optimised for the low energy region. Photons are reconstructed as conversions in the central tracking detectors and as energy deposits from electromagnetic showers in the barrel electromagnetic calorimeter. The conversion probability within the OPAL tracking system for such photons is about 8%. On average 0.82 photon conversion candidates were selected for each B candidate with an efficiency for detecting photons from the decay $B^* \to B\gamma$ of $(2.70 \pm 0.01)\%$. Similarly, on average 4.59 calorimeter photon candidates were selected for each B candidate with an efficiency for detecting photons from the decay $B^* \to B\gamma$ of $(14.52 \pm 0.03)\%$.

Using information from the conversion and calorimeter photon candidates together a probability was assigned to each B candidate representing the probability that it was a daughter of a B^* meson. Imposing requirements on this probability enables the sample to be divided into parts enriched and depleted in B^* mesons. By counting the number of entries in the two samples and also evaluating the efficiencies for the reconstruction of B_J^* decaying into $B^*\pi$ and to $B\pi$, the first measurement [65] of this branching ratio was determined as

$$\mathrm{BR}(B_J^* \to B^*\pi(X)) = 0.85^{+0.26}_{-0.27} \pm 0.12,$$

where the first error is statistical and the second systematic [65]. The uncertainty due to the variation in the range of the sideband used to normalise the background is included in the statistical error on the result. The systematic error is dominated by the uncertainty in the knowledge of the efficiencies for the reconstruction of B_J^* decaying into $B^*\pi$ and to $B\pi$ and the modelling of the combinatorial $B\pi$ background. This result is in agreement with theoretical predictions and the measured B^* and B_J^* production rates at LEP.

3.4.3 Measurement of the $B\pi$ Mass Spectra

Once the background shape has been estimated and normalised in the sideband region to the total $B\pi$ invariant mass distribution, it can be subtracted from it. The distribution must also be corrected for the mass dependence of the reconstruction efficiency before an interpretation of the B_J^* mass peaks can be performed. A fit to the total mass spectrum has been attempted before [80], but in the latest OPAL analysis [65] a simultaneous fit is performed to the two mass distributions which were obtained for the measurement of $\mathrm{BR}(B_J^* \to B^*\pi(X))$. As previously discussed, the sample depleted in the decay $B_J^* \to B^*\pi(X)$ is expected to have a larger contribution from the two states decaying to $B\pi$, namely B_0^* and B_2^*, compared to the other sample.

Several assumptions are made on the nature of the observed signal to reduce the number of free parameters in the fit. For example, it is first assumed that the signal excess arises from B_J^* decays only and that the predictions of the HQET hold for the four B_J^* states and therefore five different mass peaks are expected from single pion transitions. The contribution from di-pion transitions are estimated from simulated events and various HQET motivated assumptions are imposed on the mass splitting between the various states based on results from measurements of the D_J^* [3]. Furthermore, the fit yields a measurement of $\mathrm{BR}(\mathrm{B}_J^* \to \mathrm{B}^*\pi)$ which can be indirectly compared to the model-independent measurement of $\mathrm{BR}(\mathrm{B}_J^* \to \mathrm{B}^*\pi(\mathrm{X}))$.

With these constraints in place, the remaining free parameters are the sum of the number of entries in the B^* enriched and the B^* depleted samples, $M(\mathrm{B}_1(3/2))$, $\Gamma(\mathrm{B}_1(3/2))$, $M(\mathrm{B}_0^*)$, $\Gamma(\mathrm{B}_0^*)$, $\mathrm{BR}(\mathrm{B}_J^* \to \mathrm{B}^{(*)}\pi\pi)$ and $\mathrm{BR}(\mathrm{B}_J^* \to \mathrm{B}^*\pi)$. The fit to the mass spectra is performed in the $\mathrm{B}\pi$ mass region of $5.40 - 6.10\,\mathrm{GeV}/c^2$. The best fit for these two samples is shown in figures 3.4 and 3.5 and the fit results are:

$$
\begin{aligned}
M(\mathrm{B}_1(3/2)) &= (5.738^{+0.005}_{-0.006} \pm 0.007)\,\mathrm{GeV}/c^2, \\
\Gamma(\mathrm{B}_1(3/2)) &= (18^{+15+29}_{-13-23})\,\mathrm{MeV}/c^2, \\
M(\mathrm{B}_0^*) &= (5.839^{+0.013+0.034}_{-0.014-0.042})\,\mathrm{GeV}/c^2, \\
\Gamma(\mathrm{B}_0^*) &= (129^{+27}_{-23} \pm 63)\,\mathrm{GeV}/c^2, \\
\mathrm{BR}(\mathrm{B}_J^* \to \mathrm{B}^{(*)}\pi\pi) &= (0.245^{+0.027+0.107}_{-0.028-0.121}), \\
\mathrm{BR}(\mathrm{B}_J^* \to \mathrm{B}^*\pi) &= 0.74^{+0.12+0.21}_{-0.10-0.15},
\end{aligned}
$$

where the uncertainties are statistical and systematic, respectively [65]. The same systematic uncertainties affecting the measurement of $\mathrm{BR}(\mathrm{B}_J^* \to \mathrm{B}^*\pi(\mathrm{X}))$ also dominate the results for the simultaneous fit to the two mass spectra, particularly at low $\mathrm{B}\pi$ mass values. The uncertainty on the fit results for $M(\mathrm{B}_0^*)$, $\Gamma(\mathrm{B}_0^*)$ and $\mathrm{BR}(\mathrm{B}_J^* \to \mathrm{B}^{(*)}\pi\pi)$ are dominated by their systematic errors. The fit results are compatible with the predictions of HQET models reflecting the higher mass of the broad states.

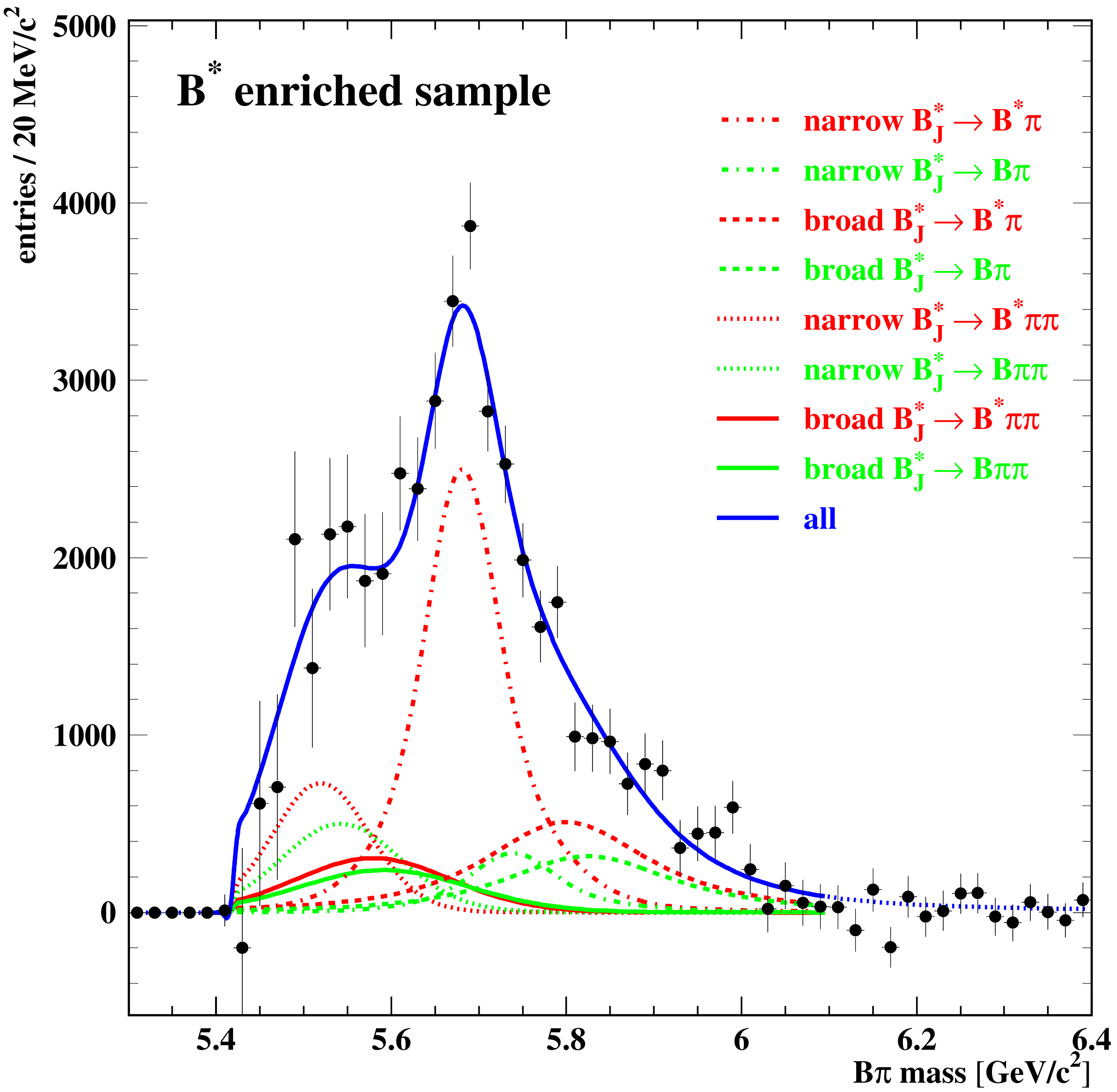

Figure 3.4: The fit to the $\mathrm{B}\pi$ invariant mass spectrum for B_J^* candidates enriched in the transition $\mathrm{B}_J^* \to \mathrm{B}^*\pi(\mathrm{X})$. The results arise from a simultaneous fit to the enriched and depleted $\mathrm{B}\pi$ mass spectra (see also figure 3.5).

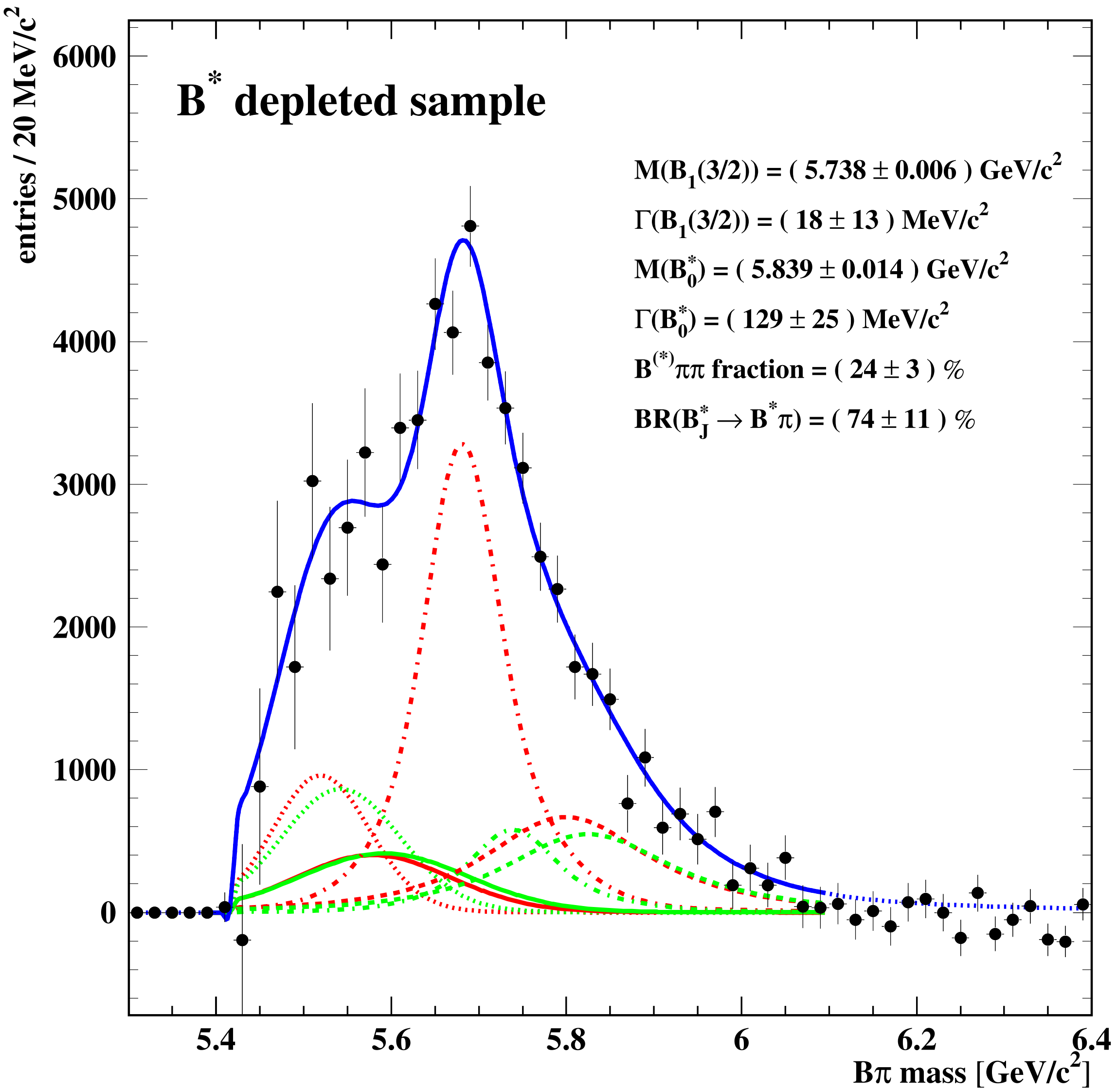

Figure 3.5: The fit to the $B\pi$ invariant mass spectrum for B_J^* candidates depleted in the transition $B_J^* \to B^*\pi(X)$. The results arise from a simultaneous fit to the enriched and depleted $B\pi$ mass spectra (see also figure 3.4).

Chapter 4

Triple Gauge Couplings in W Events

During the LEP2 phase of data-taking, events are recorded at a range of centre-of-mass energies above the threshold for the production of W-pairs. At these energies there are several processes which contain a coupling between three gauge bosons. By studying the properties of the events produced by these processes it is possible to determine the strengths of these couplings. At LEP2, the events which are sensitive to the WWZ and WWγ vertices are those in which a W-pair, a single-W or a single-γ are produced. In particular, the rate at which these events occur and the angular distributions of their final state particles provide a route to studying the coupling strengths. In this and the following chapter a measurement of the triple gauge couplings, also called TGCs, is performed using the angular distributions in WW $\rightarrow \ell\nu\ell\nu$ events recorded by OPAL at centre-of-mass energies in the range 192–202 GeV.

This chapter begins with a discussion of the couplings between three gauge bosons and how they arise in the Standard Model. In the following section the W-pair events which are sensitive to these couplings are introduced, together with the way in which they are reconstructed in order to make the measurement. The selection of the WW $\rightarrow \ell\nu\ell\nu$ events which are used for the measurements presented in this thesis is then described. The procedure adopted for extracting the values of these couplings is described in the next chapter. This leads on to a discussion of the tests which are performed to check the validity and robustness of the technique. Finally, following a discussion of the systematic uncertainties associated with the measurement, the results for the coupling values extracted from the data are presented. These results are combined with those measured using data from other decay channels and recorded during previous years as well as those from other collaborations.

4.1 Triple Gauge Coupling Framework

The Feynman diagrams for W-pair, single-W and single-γ production which contain couplings between three gauge bosons are given in figures 4.1. These diagrams arise as a consequence of the triple gauge boson vertices WWγ and WWZ[a] which are expected due to the non-Abelian gauge structure of the electroweak theory. W-pair events involving the s-channel γ and Z exchange are sensitive to couplings associated with both the WWγ and WWZ vertices. At LEP2, this process provides the largest statistics for such vertices and therefore the best TGC measurements. In single-W production the dominant amplitude involving a triple gauge coupling arises from the radiation of a virtual photon from the incident electron or positron, interacting with a virtual W radiated from the other incident particle. The equivalent diagram with the WWZ coupling is strongly suppressed due to the large mass of the Z boson. These events are therefore sensitive to the couplings associated with the WWγ vertex. In single-γ events each incoming particle radiates a virtual W which fuse to produce an outgoing photon. In this process the WWγ vertex is studied independently of the WWZ vertex. Although the W-pair events dominate the measurement of the couplings, the single-W and photonic events offer clean signatures and can provide complementary information. Other vertices involve three neutral gauge bosons and they include the ZZZ, ZZγ and Z$\gamma\gamma$ vertices. These vertices are not expected in the Standard Model but limits have been placed on the values of their couplings by OPAL [81–83]. Limits on the quartic

[a]The WWγ and WWZ vertices are more generally labelled WWV ($V \equiv \gamma, \mathrm{Z}$)

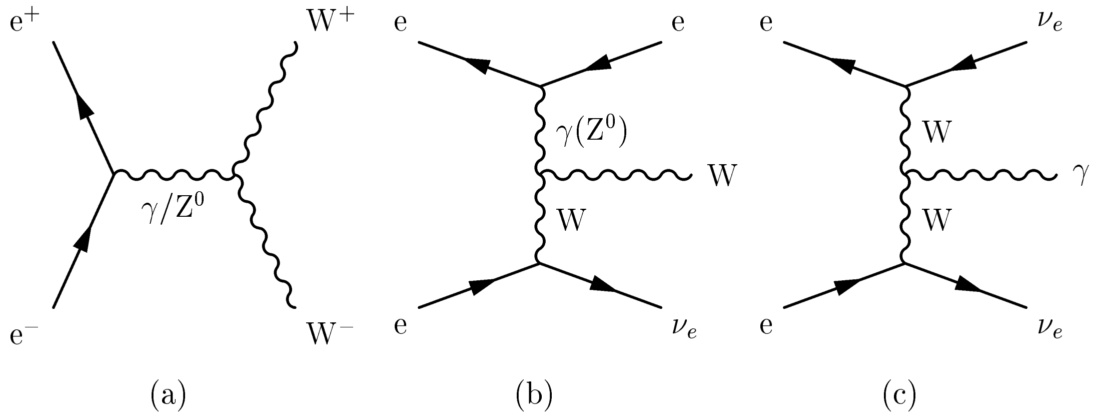

Figure 4.1: Feynman diagrams containing triple gauge boson couplings. The processes are referred to as (a) W-pair, (b) single-W and (c) single-γ production.

gauge couplings in the WW$\gamma\gamma$ and WWγZ vertices have also been made [84, 85], in the following only the WWV vertices are considered.

As discussed in section 1.3, anomalous triple gauge coupling values affect the total cross-section for these processes. By precisely measuring the cross-section and comparing it with the theoretical expectation, limits on the range of values for the coupling strengths can be determined. Anomalous TGC values also give different contributions to the different helicity states of the outgoing W bosons. This consequently affects the angular distributions of the W bosons and their decay products. Again, by measuring the angular distribution of the final states in these events and comparing them with theoretical expectations, the strengths of the couplings can be measured. The angular information in W-pair events is more sensitive to the TGCs than the cross-section and therefore provides a more precise measurement. By investigating both the rate and shape of these events, the TGC values can be measured. Because of the different experimental signatures, the different W-pair decay channels are analysed separately. In this analysis only the shape of the WW $\rightarrow \ell\nu\ell\nu$ events are used to determine the TGC values.

The values of these couplings are predicted by the Standard Model and measuring them is important as a confirmation of this theory. The values of the couplings may also be sensitive to new physics beyond the Standard Model and so their measurement is also an important approach to probing for such effects. Any theory which incorporates new physics while including the electroweak theory as an effective low energy limit, may introduce small deviations in some of the TGC values from their Standard Model values [86].

The nature of the couplings between the three gauge bosons WWZ and WWγ can be described by a total of 14 coupling parameters, seven for each vertex [87]. The most general Lorentz-invariant Lagrangian for this reaction is given by

$$\begin{aligned} i\frac{\mathcal{L}_{\text{eff}}^{WWV}}{g_{WWV}} &= [\; g_1^V V^\mu (W_{\mu\nu}^- W^{+\nu} - W_{\mu\nu}^+ W^{-\nu}) \\ &+ \kappa_V W_\mu^+ W_\nu^- V^{\mu\nu} \\ &+ \frac{\lambda_V}{M_{\text{W}}^2} V^{\mu\nu} W_\nu^{+\rho} W_{\rho\mu}^- \\ &+ i g_5^V \epsilon_{\mu\nu\rho\sigma}((\partial^\rho W^{-\mu}) W^{+\nu} - W^{-\mu}(\partial^\rho W^{+\nu})) V^\sigma \\ &+ i g_4^V W_\mu^- W_\nu^+ (\partial^\mu V^\nu + \partial^\nu V^\mu) \\ &- \frac{\tilde{\kappa}_V}{2} W_\mu^- W_\nu^+ \epsilon^{\mu\nu\rho\sigma} V_{\rho\sigma} \\ &- \frac{\tilde{\lambda}_V}{2m_W^2} W_{\rho\mu}^- W_\nu^{+\mu} \epsilon^{\nu\rho\alpha\beta} V_{\alpha\beta} \;] \end{aligned} \tag{4.1}$$

where $V^{\mu\nu} = \partial^\mu V^\nu - \partial^\nu V^\mu$, $W^{\mu\nu} = \partial^\mu W^\nu - \partial^\nu W^\mu$ and $V \equiv \gamma$ or Z. The overall coupling strength is g_{WWV} where $g_{WW\gamma} = -e$ and $g_{WWZ} = -e \cot\theta_W$, e being the electron charge magnitude and θ_W the electroweak mixing angle. The couplings are g_1^V, κ_V, λ_V, g_5^V, g_4^V, $\tilde{\kappa}_V$ and $\tilde{\lambda}_V$. Their charge conjugation (C) and parity (P) invariance properties together with their tree level values in the Standard Model are summarised in table 4.1. The couplings g_1^V, κ_V and λ_V conserve C and P separately, while g_5^V violates C and P, but conserves CP. Finally, g_4^V, $\tilde{\kappa}_V$ and $\tilde{\lambda}_V$ conserve only one of C or P and violate CP conservation. The couplings g_1^V and κ_V have non-zero values, and often their *deviations* from their expected Standard Model values, Δg_1^V ($\equiv g_1^V - 1$) and $\Delta\kappa_V$ ($\equiv \kappa_V - 1$), are discussed.

These 14 couplings provides a large parameter space to investigate, however, certain justified assumptions are made which enable the total number of measured couplings to be reduced. The couplings related to the WWγ vertex determine the static electromagnetic properties of the W, such as its charge, Q_{W}, its magnetic dipole moment,

Coupling	C	P	CP	SM value
g_1^V	$+$	$+$	$+$	1
κ_V	$+$	$+$	$+$	1
λ_V	$+$	$+$	$+$	0
g_5^V	$-$	$-$	$+$	0
g_4^V	$-$	$+$	$-$	0
$\tilde{\kappa}_V$	$+$	$-$	$-$	0
$\tilde{\lambda}_V$	$+$	$-$	$-$	0

Table 4.1: The symmetry properties of the triple gauge couplings describing the WWV vertex. Their Standard Model values are also given.

μ_{W}, and the electric quadrupole moment, q_{W}, via the relationships given by

$$\begin{aligned} Q_{\mathrm{W}} &= e g_1^\gamma, \\ \mu_{\mathrm{W}} &= \frac{e}{2M_{\mathrm{W}}}(g_1^\gamma + \kappa_\gamma + \lambda_\gamma), \\ q_{\mathrm{W}} &= -\frac{e}{{M_{\mathrm{W}}}^2}(\kappa_\gamma - \lambda_\gamma). \end{aligned}$$

It follows from the requirement of electromagnetic gauge invariance, or charge conservation in weak decays, that g_1^γ is equal to unity. At LEP2 energies, the observation of C, P or CP violation is expected to be unlikely, and therefore only the symmetry conserving couplings are retained [88], leaving a total of five couplings; g_1^Z, κ_γ, κ_Z, λ_γ and λ_Z. Nevertheless, the CP violating WWγ couplings $\tilde{\lambda}_\gamma$ and $\tilde{\kappa}_\gamma$ have already been tightly constrained by measurements of the neutron electric dipole moment to $\mid \tilde{\lambda}_\gamma \mid, \tilde{\kappa}_\gamma < 10^{-3}$ [89]. The remaining parameters can be related to each other by requiring $\mathrm{SU(2)_L} \otimes \mathrm{U(1)_Y}$ gauge invariance which leads to the constraints

$$\begin{aligned} \kappa_Z &= g_1^Z - \tan^2\theta_W(\kappa_\gamma - 1), \\ \lambda_Z &= \lambda_\gamma, \end{aligned}$$

and reduces the number of parameters to three. By restricting measurements to g_1^Z, κ_γ and λ where $\lambda = \lambda_Z = \lambda_\gamma$ the sensitivity to new physics effects is restricted to those arising only from operators within the effective WWV Lagrangian which are C, P and

CP conserving, which satisfy $\mathrm{SU(2)_L} \otimes \mathrm{U(1)_Y}$ and which have not been excluded by previous measurements. If anomalies are observed in LEP2 data then the measurement of more than these three couplings, or even of all of the couplings is desirable. This would allow the relationship between the couplings to be established, which would aid the identification of the underlying new physics.

In the TGC results from the LEP collaborations, measurements are generally presented for the three couplings g_1^Z, κ_γ and λ, although some of the other couplings have also been measured. At the OPAL collaboration, W-pair and single-W events have been analysed to measure these standard couplings [90–95] as well as the CP violating triple gauge couplings [96]. At ALEPH, measurements have been performed at LEP2 using W-pair, single-W and single-γ events [97–101]. At 189 GeV ALEPH used W-pair events to measure the C and P violating couplings g_4^V, g_5^V, $\tilde{\kappa}_V$ and $\tilde{\lambda}_V$. Similarly, a range of couplings in addition to the three standard ones have been measured at LEP2 by the DELPHI [102–105] and L3 [106–112] collaborations. Using Tevatron data, the couplings κ_γ and λ have been measured by the D0 [113] and CDF [114] collaborations.

4.2 W-Pair Events

A W boson decays into a fermion-antifermion pair, either a quark-antiquark or a lepton-neutrino pair. For example, a W^- can decay into $\mathrm{e}^-\overline{\nu}_\mathrm{e}$, $\mu^-\overline{\nu}_\mu$, $\tau^-\overline{\nu}_\tau$, or one of the three colours of $\mathrm{\overline{u}d}$ or $\mathrm{\overline{c}s}$ pairs. Since the masses are negligible and the couplings of the fermions to the W are the same, each decay channel is approximately equally probable, $\sim 11\%$, although small deviations from this arise due to higher order Feynman diagrams. In events where a W-pair is created the W bosons decay independently, they may both decay to quark-antiquark pairs, these are the so called 'fully hadronic' events. Events where one W decays leptonically and the other hadronically are called 'semi-leptonic' events, and those where both W bosons decay leptonically are the 'fully leptonic' events. A list of the branching ratios to the various single-W and W-pair final states are given in table 4.2.

Single-W

BR($W \to q\overline{q}$)	67.5%
BR($W \to e\nu_e$)	10.8%
BR($W \to \mu\nu_\mu$)	10.8%
BR($W \to \tau\nu_\tau$)	10.8%

W-pair

Fully hadronic	
BR($WW \to q\overline{q}q\overline{q}$)	45.6%
Semi-leptonic	
BR($WW \to q\overline{q}e\nu_e$)	14.6%
BR($WW \to q\overline{q}\mu\nu_\mu$)	14.6%
BR($WW \to q\overline{q}\tau\nu_\tau$)	14.6%
BR($WW \to q\overline{q}\ell\nu$) ($\ell$ = e, μ or τ)	43.9%
Fully leptonic	
BR($WW \to e\nu_e e\nu_e$)	1.2%
BR($WW \to e\nu_e\mu\nu_\mu$)	2.3%
BR($WW \to e\nu_e\tau\nu_\tau$)	2.3%
BR($WW \to \mu\nu_\mu\mu\nu_\mu$)	1.2%
BR($WW \to \mu\nu_\mu\tau\nu_\tau$)	2.3%
BR($WW \to \tau\nu_\tau\tau\nu_\tau$)	1.2%
BR($WW \to \ell\nu\ell\nu$) (ℓ = e or μ)	4.7%
BR($WW \to \ell\nu\ell\nu$) (ℓ = e, μ or τ)	10.5%

Table 4.2: Expected W decay branching ratios for single-W and W-pair events.

The topologies of the W-pair events are characterised according to the decay modes of the two decaying Ws. The $W \rightarrow q\overline{q}$ decay produces two hadronic jets of particles whereas the $W \rightarrow \ell\nu$ decay results in a single lepton with missing energy as a result of the undetected neutrino. The three lepton species have characteristic signatures, the electron and muon appear as single tracks in the detector whereas the tau with its short lifetime decays within the detector. The tau may decay hadronically or leptonically which introduces respectively one or two further unseen neutrinos into the set of final state particles. In general, the W-pair events in which the decays are fully hadronic contain four jets, the semi-leptonic events contain two jets plus an energetic lepton with missing energy, and the fully leptonic events contain just two leptons with missing energy.

4.2.1 Production and Decay Angles

In the determination of the TGC parameters using the event shape approach, in the limit of no initial state radiation and an on-shell W, all of the information in a W-pair event is contained within a set of five angles. The definition which is usually adopted for these angles is that described in [86,88]. These angles are labelled as $\cos\theta_{\mathrm{W}}$, $\cos\theta_1^*$, ϕ_1^*, $\cos\theta_2^*$ and ϕ_2^* and they are illustrated in figure 4.2. The event consists of the incoming electron and positron which interact to produce a back-to-back W^- and a W^+. The production angle, $\cos\theta_{\mathrm{W}}$, is defined as the angle between the direction of the incoming electron and the outgoing W^- boson. Each W decays into a fermion-antifermion pair and the polar and azimuthal angles are defined for each within the framework of two right-handed sets of orthogonal axes associated with each boson in their respective rest frames. For the W^- decay the angles θ_1^* and ϕ_1^* are the polar and azimuthal decay angles of the outgoing *particle*, this is the ℓ^- lepton or d-quark in the W^- rest frame. Similarly, θ_2^* and ϕ_2^* are the same decay angles for the *antiparticle*, ℓ^+ or $\overline{\mathrm{d}}$-quark, in the W^+ rest frame. This set of angles fully defines the angular distribution of the W-pair event.

Consider the case of a fully leptonic W-pair event. In these events, if the charged

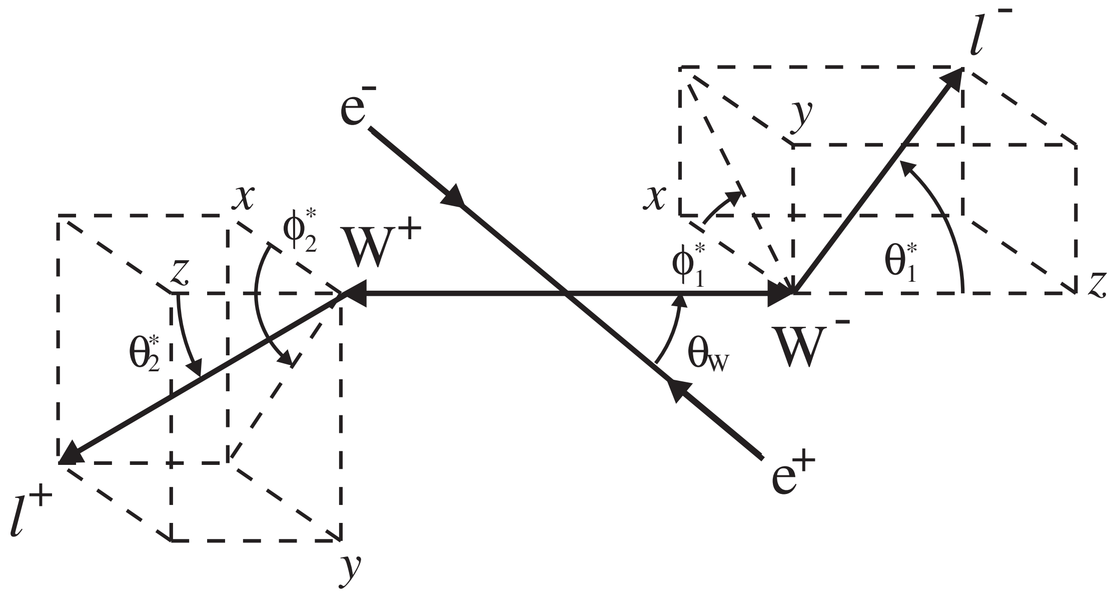

Figure 4.2: The five-angle definition for the final state particles in W-pair events used to measure the triple gauge boson couplings.

leptons are either electrons or muons, then the set of final state particles consist of two charged leptons and two neutrinos. Since the neutrinos are undetected, only two charged leptons are observed together with significant missing energy in the event. These leptons are labelled ℓ^- and ℓ^+ in figure 4.2. The reconstruction of the W momenta in these events uses the three-momenta of the two charged leptons, $\mathbf{p}_{\ell^-}$ and $\mathbf{p}_{\ell^+}$, the mass of the W, M_{W}, and the beam energy, E_{beam} [115]. If the finite width of the W is ignored and so they are considered to be on-shell, and assuming that there is no initial state radiation, the magnitude of the momenta of the two Ws are equal and also known from E_{beam} and M_{W}. This also means that they are produced back-to-back in the laboratory frame of reference. The W^- four-momentum, for example, is the sum of the four-momenta of the ℓ^- and $\overline{\nu}$. The W^+ four-momentum is the reflection through the origin of that of the W^- which is also equal to the sum of the four-momenta of the ℓ^+ and ν. Since the momenta of the two neutrinos are directly related, only one needs to be reconstructed. The momentum of the $\overline{\nu}$, $\mathbf{p}_{\overline{\nu}}$, can be calculated as a linear combination of the momenta of the two charged leptons plus or minus a component which is perpendicular to the plane containing these two momenta, such that

$$\mathbf{p}_{\overline{\nu}} = a\mathbf{p}_{\ell^-} + b\mathbf{p}_{\ell^+} \pm d\mathbf{p}_{\ell^-} \times \mathbf{p}_{\ell^+}.$$

The sign ambiguity means that there are actually two solutions for $\mathbf{p}_{\overline{\nu}}$, assuming $d \neq 0$, corresponding to a reflection of both neutrinos in the plane defined by the charged leptons. In terms of the reconstructed five-angle set, this means that the angles θ_1^* and θ_2^* are known unambiguously, but $\cos\theta_{\mathrm{W}}$, ϕ_1^* and ϕ_2^* in general have two solutions. The coefficients a, b and d are determined from $\mathbf{p}_{\ell^-}$, $\mathbf{p}_{\ell^+}$, E_{beam} and M_{W} using the expressions

$$\begin{aligned}
a &= \frac{m|\mathbf{p}_{\ell^+}|^2 - n\mathbf{p}_{\ell^-}\cdot\mathbf{p}_{\ell^+}}{|\mathbf{p}_{\ell^-}\times\mathbf{p}_{\ell^+}|^2}, \\
b &= \frac{n|\mathbf{p}_{\ell^-}|^2 - m\mathbf{p}_{\ell^-}\cdot\mathbf{p}_{\ell^+}}{|\mathbf{p}_{\ell^-}\times\mathbf{p}_{\ell^+}|^2}, \\
d^2 &= \frac{(E_{\mathrm{beam}} - |\mathbf{p}_{\ell^-}|)^2 - a^2|\mathbf{p}_{\ell^-}|^2 - b^2|\mathbf{p}_{\ell^+}|^2 - 2ab\mathbf{p}_{\ell^-}\cdot\mathbf{p}_{\ell^+}}{|\mathbf{p}_{\ell^-}\times\mathbf{p}_{\ell^+}|^2}, \\
m &= E_{\mathrm{beam}}|\mathbf{p}_{\ell^-}| - |\mathbf{p}_{\ell^-}|^2 - \frac{1}{2}{M_{\mathrm{W}}}^2, \\
n &= -E_{\mathrm{beam}}|\mathbf{p}_{\ell^+}| - \mathbf{p}_{\ell^-}\cdot\mathbf{p}_{\ell^+} + \frac{1}{2}{M_{\mathrm{W}}}^2.
\end{aligned}$$

Using these expressions and assuming an on-shell W with no initial state radiation, two sets of five-angles can be reconstructed for each $\mathrm{WW} \to \ell\nu\ell\nu$ event in which the charged leptons are electrons or muons. Either one of these sets carry the angular information needed for measuring the TGC values, therefore both sets must be used. Despite the presence of additional neutrinos in events containing tau final states which makes a unique reconstruction of the five-angle set impossible, these events still carry useful TGC information in their angular distribution without significantly biasing the results.

To reconstruct the five-angle set for a W-pair event, the minimum information which is required are the directions of the W decay products and also their charges so that the W^- can be distinguished from the W^+. The accessibility of this information depends on the W-pair decay channel:

- The **fully hadronic** W-pair events have a four jet topology with no missing energy and so the kinematics of the event can be fully reconstructed. The difficulty lies in assigning the jet pairs to the correct W boson decay. Furthermore, in the absence of any quark charge determination, the W^- cannot be distinguished from the W^+. In addition, the fermion cannot be distinguished from the antifermion which results in an ambiguity in the reconstructed angles for each pair of jets.

- In **semi-leptonic** W-pair events containing a pair of jets with one isolated energetic lepton and significant missing energy, the charge of the lepton allows the charges of the decaying W bosons to be determined. The quark pair still produces an ambiguity in the reconstructed polar and azimuthal angles for the hadronically decaying W, but the lepton defines the other set uniquely.

- In **fully leptonic** W-pair events the charges of the leptons enable the charges of the W^- and W^+ to be determined unambiguously. However, it has already been discussed that the two neutrinos lead to a two solution ambiguity in the reconstructed direction of the two W bosons.

These constraints consequently affect the sensitivity of each channel to the triple gauge couplings. The kinematic reconstruction is further complicated, and the sensitivity reduced, by the presence of additional neutrinos from the production of a tau in the leptonically decaying Ws. In table 4.2 it can be seen that W-pair events are predominantly shared between those decaying hadronically and those decaying semi-leptonically. Due to the large branching ratio, the relative ease in precisely reconstructing the event, and the better available kinematics in semi-leptonic events, this channel is the most powerful in which to study TGCs in W-pair events. The large statistics of the hadronic channel also make it an important channel to study. Finally, despite the smaller statistics of the fully leptonic channel, the precision with which the leptons can be reconstructed means that the channel is also important for TGC studies.

4.2.2 Reconstruction

The ease with which the five-angles for a selected event can be reconstructed is limited by several factors beyond those already described, these are discussed in the following.

The most important ones are described and then the measures which are taken in order to overcome them are discussed for each W-pair decay channel. The ability to reconstruct the five-angles for a W-pair event is affected by:

- the limited resolution of the detector for the reconstruction of the jet and lepton energies and directions,
- the difficulty in accurately determining the charge of the quarks produced by hadronically decaying Ws when attempting to determine the charge of the W,
- the presence of initial state radiation, where a photon is emitted from the incoming electron or positron prior to the collision, reducing the effective centre-of-mass energy of the collision,
- the presence of events passing the selection which are from a process other than the one being studied,
- the presence of undetected neutrinos from Ws decaying leptonically and from tau decays.

In an attempt to overcome these difficulties, constraints are applied when reconstructing the events. The constraints used in the OPAL analyses for extracting the TGC values from W-pair events [92, 94, 95] include:

- requiring the conservation of energy and momentum, so that the total energy of the final particles is equal to the centre-of-mass energy, and the total momentum in the laboratory frame of reference is zero. This actually corresponds to four separate constraints,
- requiring constraints on the masses of the two decaying Ws obtained from the reconstructed invariant mass of the decay products from each such that:
  - the masses of the two Ws are equal to each other,

– the masses of the two Ws are equal to the expected W mass, for example the world average value or that measured at the Tevatron.

These constraints neglect the presence of any initial state radiation in the event thus assuming that the e^+ and e^- interact at the full beam energy. Furthermore, the W mass constraint neglects the finite width of the W to some degree. The application of these constraints for the different channels is described in the following.

Fully hadronic events

In the OPAL analysis which measures TGCs in fully hadronic W-pair events, each WW $\rightarrow$ qqqq candidate is reconstructed as four jets. These can be paired together to form the two W bosons in three possible ways. A kinematic fit requiring the conservation of energy and momentum, and the equality of the two reconstructed W masses is applied to each of these combinations. A likelihood technique is then used to determine the correct jet pairing combination. Furthermore, at least one of these jet pairings must have a reconstructed W mass in the range 70–90 GeV. For the analysis performed using 189 GeV data [94], the final probability for obtaining the correct pairing was 87%. The W charge is assigned by comparing the sum of the charges of the particles in the two jets coming from the same W. This is used to correctly identify the W^- and W^+ systems with a probability of 82%. This channel also suffers from a 12% background contribution.

Semi-leptonic events

In the OPAL analysis which measures TGCs in semi-leptonic W-pair events, the sample of events in which the leptonically decaying W produces an electron or muon is treated separately from those events containing a tau. In WW $\rightarrow$ qq$e\nu$ and WW $\rightarrow$ qq$\mu\nu$ candidate events, the isolated lepton is required to be well reconstructed in the tracking chambers. The taus in the WW $\rightarrow$ qq$\tau\nu$ candidates are reconstructed from the one or three tracks assigned to it. The remaining tracks in the event are grouped into two jets and the requirement for the conservation of energy and momentum is applied. Requiring the additional constraint for the equality of the reconstructed W masses with a value equal to that measured at the Tevatron improves the angular resolution of the $q\overline{q}e\nu$ and $q\overline{q}\mu\nu$ events. The remaining background fraction for the semi-leptonic final state analysis is 4.6%.

Fully leptonic events

In more than half of the WW $\rightarrow \ell\nu\ell\nu$ events a tau lepton is present whose decay produces further neutrinos which makes the precise reconstruction of the five-angles more difficult. Nevertheless, a reconstruction of the tau can be attempted and the five-angles calculated in the same way, but the angular information tends to become distorted. In fact, in the measurements presented in this thesis, those events with a tau in the final state are removed from the sample. This gives rise to a loss in statistics but an improvement in the quality of the angular information. The efficiency with which these tau events can be rejected is not critical since these events do still carry information about the triple gauge couplings in their angular distributions.

Since the presence of initial state radiation and the finite width of the W are ignored in the WW $\rightarrow \ell\nu\ell\nu$ reconstruction scheme already described, and also since the detector has a finite resolution, the value for d^2 in the algebra presented in section 4.2.1 may have a negative value. This results in a complex solution for the value of $\mathbf{p}_{\overline{\nu}}$, in fact about 26% of the events reconstructed have these non-physical solutions. Excluding these events from the sample introduces significant biases in the determination of the coupling values. These events are included by setting the imaginary part to zero and allowing the real part to provide the solution. In this way the bias is effectively removed [115]. Another feature of the reconstruction of the WW $\rightarrow \ell\nu\ell\nu$ events is that the five-angle set has two distinct solutions. Both of these solutions must be used since either of them may be a true representation of the event, therefore in these events both sets of five-angles enter with a weight of a half.

The minimum and maximum energies of the two charged leptons can be calculated by considering the extreme cases where the lepton and neutrino from a W are produced back-to-back along the flight direction of the W. Assuming that the e^+e^- collision took place at the full centre-of-mass energy, $\sqrt{s}$, and that the leptons are massless, the lepton energy, E_ℓ, extremes can be calculated using

$$E_\ell = \frac{\sqrt{s} \pm \sqrt{s - 4{M_\mathrm{W}}^2}}{4} \tag{4.2}$$

where M_W is the mass of the W boson, taken as the on-shell mass. In events where the lepton energy has been reconstructed with a value which is significantly larger that the maximum possible E_ℓ for that event, the lepton energy is truncated. For events recorded at a centre-of-mass energy of 189 GeV, the maximum lepton energy is $\sim 72 \pm 2$ GeV, where the uncertainty is determined by the width of the W. The truncation used is 80 GeV. A similar cut on the minimum lepton energy is applied during the event selection stage.

4.3 WW $\rightarrow \ell\nu\ell\nu$ Events

Since the centre-of-mass energy delivered by LEP exceeded the W-pair production threshold of 161 GeV in 1996, at OPAL more than 700 pb^{-1} of data have been recorded with the collection of around 10 000 WW candidate events. The measurement of the triple gauge boson couplings presented in this thesis is based on WW $\rightarrow \ell\nu\ell\nu$ events from data collected during 1999 at four separate centre-of-mass energies in the range 192–202 GeV. Throughout this thesis, the four energy points are given the labels 192, 196, 200 and 202 GeV, corresponding to the integer values closest to the actual energy. The data recorded at each point may itself have a range of energies and so a better indication of the true centre-of-mass energies is the luminosity weighted average which is given in table 4.3. The luminosity of the data at each energy was measured by recording small angle Bhabha scattering events in the silicon-tungsten luminometer [116], this detector was discussed earlier in section 2.2.4, and these values are also given in table 4.3

	Centre-of-Mass Energy			
	192	196	200	202
Average $\sqrt{s}$ [GeV]	191.6	195.5	199.5	201.6
$\int \mathcal{L}\,\mathrm{d}t$ [pb^{-1}]	29.3 ± 0.1	69.0 ± 0.2	76.5 ± 0.2	37.6 ± 0.1

Table 4.3: The luminosity weighted average centre-of-mass energy and recorded integrated luminosity, $\int \mathcal{L}\,\mathrm{d}t$, for the four data sets used in the TGC analysis.

4.3.1 Selection

The selection of a WW $\rightarrow \ell\nu\ell\nu$ event is based on the requirement of a pair of charged leptons, acoplanar with the beam axis, with significant missing energy. The OPAL selection for these events was developed at the beginning of 1996 when events were first recorded at energies above the W-pair production threshold [117]. The selection was improved [118] and used in conjunction with another acoplanar lepton selection which was developed independently [119]. The most recent descriptions of this selection can be found in [120–122]. The three W-pair event selections used in the OPAL TGC measurement are exclusive. Those events failing the WW $\rightarrow \ell\nu\ell\nu$ event selection are considered as possible WW $\rightarrow$ qq$\ell\nu$ candidates and only events failing both the WW $\rightarrow \ell\nu\ell\nu$ and WW $\rightarrow$ qq$\ell\nu$ selections are considered as possible WW $\rightarrow$ qqqq candidates.

Each of the charged leptons have a characteristic signature in the OPAL detector. The one with the cleanest signature is the muon since it interacts minimally with the material of the detector leaving a clear track in the central tracking detectors, small energy deposits in the calorimeters and hits in the outer muon detectors. The signature of the electron is a track in the central tracking chambers, and energy deposits in the electromagnetic calorimeters. The tau, however, is unstable and decays either leptonically or hadronically as it leaves the interaction point. Leptonic tau decays produce either a single electron or a muon whereas hadronic decays produce normally one or three charged hadrons.

The selection is performed in several stages as follows:

- **Preselection Cuts**

  Events with hadronic final states are removed from the sample by requiring them to be classed as being of low multiplicity and not of high multiplicity. Also, the functional status of those subdetectors which are most important to this analysis are required to be operational at the point in time at which the event was recorded. At least the central tracking detectors, the electromagnetic calorimeters, the luminometers and the muon detectors must be sufficiently functioning.

- **Quality Cuts**

  The tracks and clusters observed in the event are selected according to a set of quality cuts which ensure that the reconstructed quantities associated to them are suitable for use in the subsequent analysis. These quality cuts include:

  - $p_{\mathrm{T}} > 0.15\,\mathrm{GeV}/c$,

    where p_{T} is the transverse momentum of the track. This ensures that the track is located within the detector and is sufficiently well measured,

  - $|d_0| < 2\,\mathrm{cm}$ and $|z_0| < 25\,\mathrm{cm}$,

    where d_0 and z_0 are the impact parameters of the track in three dimensions, these were discussed in chapter 3. This cut ensures that the track is associated with the interaction point therefore helping to reject cosmic ray backgrounds,

  - $N_{\mathrm{CT\,hits}} > 20$,

    where $N_{\mathrm{CT\,hits}}$ is the number of hits associated with the track in the central tracking detectors, ensuring that there is sufficient information to reconstruct the track,

  - $E_{\mathrm{EB\,cluster}} > 0.1\,\mathrm{GeV}$ and $E_{\mathrm{EE\,cluster}} > 0.25\,\mathrm{GeV}$,

    where $E_{\mathrm{EB\,cluster}}$ and $E_{\mathrm{EE\,cluster}}$ are the energy of the cluster in the barrel and endcap electromagnetic calorimeters respectively,

- $E_{\mathrm{FD\,cluster}} > 5\,\mathrm{GeV}$, $E_{\mathrm{GC\,cluster}} > 5\,\mathrm{GeV}$ and $E_{\mathrm{SW\,cluster}} > 2\,\mathrm{GeV}$,

  where $E_{\mathrm{FD\,cluster}}$, $E_{\mathrm{GC\,cluster}}$ and $E_{\mathrm{SW\,cluster}}$ are the energy of the clusters in the forward detector, gamma catcher and silicon-tungsten luminometer subdetectors.

Algorithms which match tracks to clusters are adopted to avoid double counting of energy clusters associated with charged tracks. Energy clusters in the hadronic calorimeters are not used since the number of neutral hadrons in leptonic events is negligible.

- **Multiplicity Cuts**

  The lepton candidates are located in the event by grouping all of the reconstructed charged particles into jets using a cone jet finding algorithm. The cone half opening angle is 20° and the jet energy threshold is $2.5\,\mathrm{GeV}$. This procedure allows the taus as well as the electrons and muons to be identified despite their higher multiplicity. The cuts on the overall event multiplicity include:

  - $1 \leq N_{\mathrm{ch}} \leq 8$,

    where N_{ch} is the number of charged tracks reconstructed in the event,

  - $N_{\mathrm{cl}} \leq 7$,

    where N_{cl} is the number of energy clusters reconstructed in the event,

  - $N_{\mathrm{jet}} \leq 3$,

    where N_{jet} is the number of jet cones found in the event.

- **Event Shape Cuts**

  In the general acoplanar lepton selection, the sets of cuts applied to the events depend upon the value of N_{jet}. In this analysis, since the momenta of both of the leptons need to be reconstructed, the further requirement $2 \leq N_{\mathrm{jet}} \leq 3$ is imposed. The majority of these events are reconstructed as having two jets, but for those in which there are more than two cones, the two highest energy ones are retained. The following event shape cuts correspond to those used for events with $N_{\mathrm{jet}} = 2$ in the general selection.

Processes such as initial state radiation can lead to high energy particles escaping along the beam pipe leading to large missing momentum in this direction. The selection of candidate WW $\to \ell\nu\ell\nu$ events require that the total missing momentum vector is away from the direction of the beam axis. The main event shape cuts include:

- $\phi_{\mathrm{acol}} > 5°$,

  where ϕ_{acol} is the acollinearity angle of the two jets. The acollinearity angle is the complement of the opening angle between the two jet directions calculated in three dimensions and this cut ensures that there is missing momentum in the event,

- $x_{\mathrm{T}} > 0.05$,

  where x_{T} is the net transverse momentum of the di-jet system divided by the beam energy. Requirements are also imposed on the significance of x_{T}, and these cuts ensure that the event has significant missing transverse momentum.

Several other variables are defined to describe the direction of the missing momentum in the event, such as the acoplanarity, and the missing transverse momentum in the plane transverse to the thrust axis of the event. Cuts on these variables further improve the performance of the acoplanar lepton selection.

- **Background Rejection**

  A set of cuts are applied to reject events which are most likely to represent background. Events are rejected under the following criteria:

  - if there are selected tracks which are not associated with either of the jets,

  - if a track is observed in the muon endcap subdetector in the polar angle range $|\cos\theta| > 0.95$ and it lies outside the jet cones. Furthermore, the event is also rejected if any minimum ionising particle tracks are observed in the silicon-tungsten luminometer or minimum ionising particle detector,

– if the energy deposited in the forward detectors, the silicon-tungsten luminometers or the electromagnetic and hadronic calorimeters is greater than a certain fraction of the total centre-of-mass energy.

The selection described above provide a sample of acoplanar charged lepton events. In section 4.2 the problems associated with reconstructing the five-angles in the presence of a tau lepton in the $\ell\nu\ell\nu$ final state were discussed. For these reasons the events containing any taus are removed from the sample.

To do this, the events are first classified into one of the six dilepton types using a lepton identification procedure [121, 123]. The leptons in the selected events are assigned a particular type using standard OPAL lepton identification algorithms. Electron identification is based on the track momenta in the central detector and on the electromagnetic calorimeter cluster energy. Muons are also identified by their signal left in the central detector, and also by hits in the hadron calorimeters and muon chambers. Hadronically decaying taus are separated by means of hadron identification and track multiplicity criteria. Particular problems arise when taus decay to electrons and muons, for example, if a track is identified as an electron it is difficult to ascertain whether the electron was prompt from the decay of a W boson or came via the decay of a tau. A small improvement to the tau rejection is achieved by the application of acollinearity dependent momentum cuts so that electrons or muons with low momentum, consistent with the leptonic decay of a tau, are re-classified as taus. These cuts rely upon the correlation between the lepton energy and decay angle from the parent W. Finally, those events classed as having a tau lepton in the final state are rejected. The procedure also returns the lepton charge which is needed to reconstruct the five-angle set.

4.3.2 Backgrounds

Besides being very efficient at selecting events with acoplanar charged leptons, the event selection is also efficient at rejecting those where the process that occurs gives rise to some other final state. Nevertheless, a small fraction of events of this kind may survive the selection cuts and become a part of the sample used in the final analysis. Estimating this effect is achieved by applying the selection to events which simulated the background processes. A list of the Monte Carlo event generators used for this purpose is given in appendix A, some of them, namely the four-fermion generators, simulate all processes, while others simulate particular regions of phase space. The main sources of background are described below and the dominant ones are expected to be dilepton, single-W and Z-pair events. The number of these events which pass the selection cuts together with the integrated luminosities of the simulated data is used to calculate the expected background contamination in the real OPAL data, these are listed in table 4.4. Some Monte Carlo samples have low statistics which results in large statistical errors on the results.

- **Dilepton**

  One of the processes most likely to cause some background is dilepton production via s-channel neutral currents and t-channel scattering as shown in figure 4.3. The former produces pairs of oppositely charged leptons of the same species, and the latter gives rise to electron-positron pairs. In the s-channel process, if the collision between the electron and positron takes place at the full centre-of-mass energy, the lepton pairs are produced collinearly. In the presence of initial state radiation, where the incoming electron or positron radiates a photon before interacting, the four-momenta of the incoming leptons is asymmetric which results in the event being boosted in the laboratory frame, and the final state lepton pair are produced acollinearly. This acollinearity can also arise from final state radiation where the final state leptons emit a photon. The requirement for acoplanarity between the leptons in the selection ensures that the missing momentum is transverse to the beam axis, nevertheless, dilepton production still constitutes a source of background. The electron pair final states are simulated using BHWIDE [124] which includes both the s-channel and t-channel diagrams. The KORALZ [125] and KK2F [126] generators are used to simulate both muon and tau pair events.

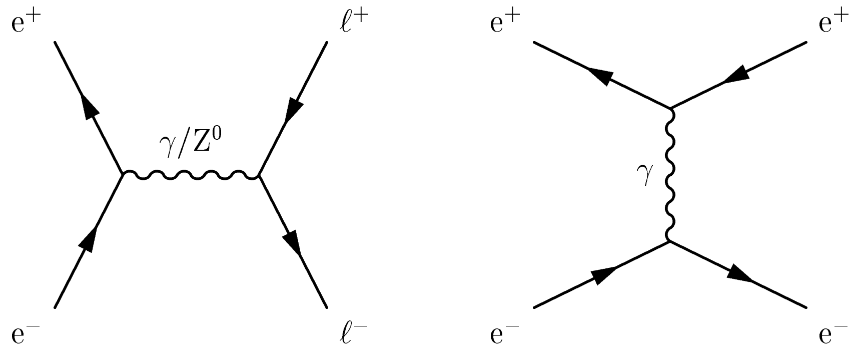

Figure 4.3: The Feynman diagrams for dilepton production via s-channel neutral current exchange and t-channel scattering.

- **Four-fermion**

  Other processes which are likely to cause some background contamination are those in which four fermions are produced, WW $\rightarrow \ell\nu\ell\nu$ events are themselves a subset of this class. W-pair production, the Feynman diagrams for which were shown in figures 1.3(b-c), has a cross-section of about 17 pb at 200 GeV, but this is not the only process leading to four fermions. Some of the four-fermion diagrams interfere with each other, therefore they are generated in the same Monte Carlo sample. The other most common four-fermion processes are:

  - **Single-W production** giving rise to a Weν final state as shown in the Feynman diagrams of figure 4.4(a-b). At 200 GeV this process has a cross-section of about 0.6 pb and in about 32% of the cases the W boson decays leptonically. The scattered electron is likely to be reasonably undeflected, but if it is observed in the detector it will have the opposite charge to the lepton from the W decay and is likely to be acoplanar with missing energy due to the neutrinos. These events do contain a triple gauge boson vertex WWV and therefore contain sensitivity to the couplings, in this sense these events constitute signal.
  - **Z-pair production**, shown in the Feynman diagram of figure 4.4(c), has a cross-section of about 1 pb at 200 GeV. It is an important background source at centre-of-mass energies above the Z-pair production threshold of about

182 GeV. In about 4% of cases, one Z decays to a pair of oppositely charged leptons, and the other invisibly to a neutrino pair, resulting in acoplanarity and missing energy in the event.

– **Single-Z production** giving rise to a $Z^0e^+e^-$ final state as shown in the Feynman diagram of figure 4.4(d). At 200 GeV this process has a cross-section of about 2 pb. If both of the initial state particles escape undetected, only the Z is observed in the detector, possibly resulting in a pair of oppositely charged acoplanar leptons with missing energy.

The Monte Carlo samples are actually divided up according to the final states which are produced, namely $e^+e^-e^+e^-$, $e^+e^-\mu^+\mu^-$, $e^+e^-\tau^+\tau^-$ and $e^+e^-q\overline{q}$ final states, and these are simulated using the GRC4F [127] Monte Carlo generator. Other samples simulate regions of phase space not already covered, namely $\ell\ell\ell\ell$[b], $\ell\ell q\overline{q}$[c] and $q\overline{q}q\overline{q}$ final states. The $\ell\ell q\overline{q}$ and $q\overline{q}q\overline{q}$ four-fermion final states are not expected to contribute any significant background.

- **Two-photon**

Another process which can give rise to background contamination is the photon-photon interaction where both of the incoming particles radiate photons as shown in figure 4.5. The electron and positron may only be minimally deflected, but the fermion pair may be charged leptons which are acoplanar. Also, one of the incoming particles may be deflected into the detector and a low angle e/μ produced, giving the same signature. The VERMASEREN [128] Monte Carlo generator is used to simulate the $e^+e^-e^+e^-$, $e^+e^-\mu^+\mu^-$ and $e^+e^-\tau^+\tau^-$ final states

- **Other**

Several other possible sources of background are investigated including neutrino pairs and radiative Bhabha events. These sources do not contribute significantly to the background.

[b] $\ell\ell\ell\ell$ samples simulate all four-lepton final states except $\nu\nu\nu\nu$ and $e^+e^-\ell^+\ell^-$ ($\ell = e, \mu$ or τ).
[c] $\ell\ell q\overline{q}$ samples simulate $\ell^+\ell^-q\overline{q}$ ($\ell = \mu$ or τ), $\nu\nu q\overline{q}$ and $\ell\nu q\overline{q}$ ($\ell = e, \mu$ or τ) final states together.

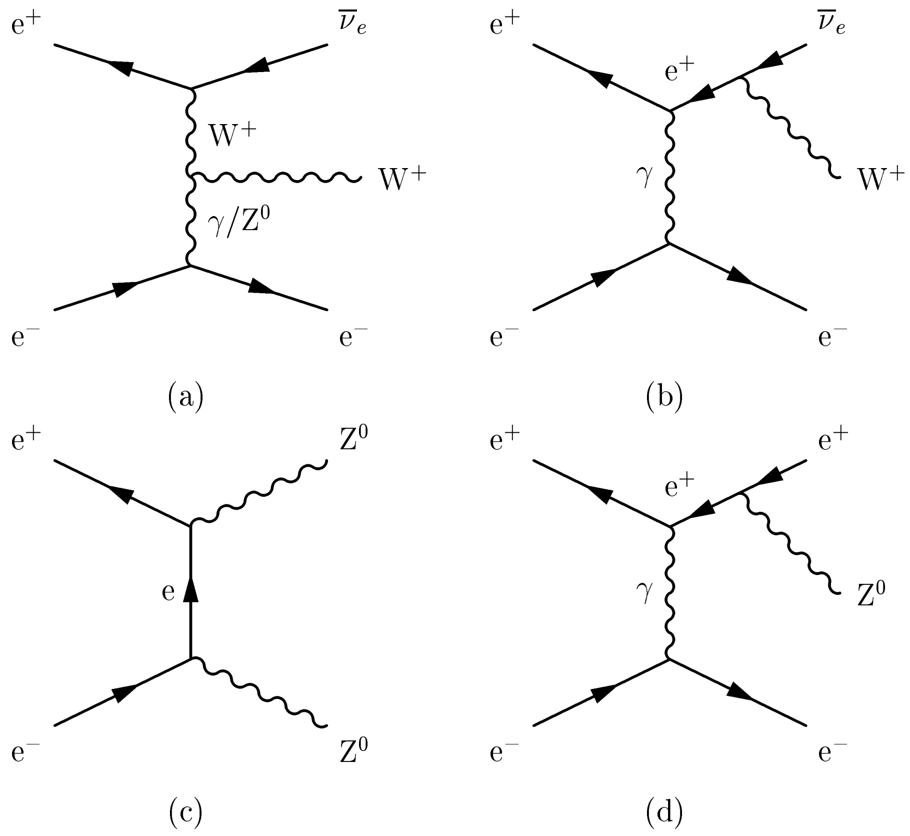

Figure 4.4: Examples of Feynman diagrams for the four-fermion processes (a-b) single-W production, (c) Z-pair production and (d) single-Z production.

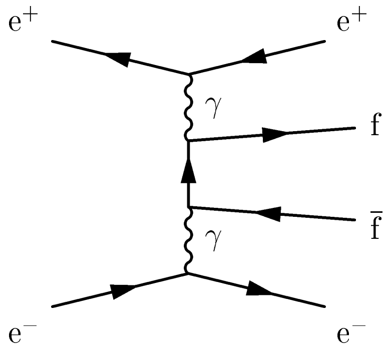

Figure 4.5: An example of a Feynman diagram for the two-photon process.

	Expected accepted cross-section for background events [fb]							
	192		196		200		202	
Process	$\mathrm{Sel}^{\ell\nu\ell\nu}$	$\mathrm{Sel}^{\mathrm{fin}}$	$\mathrm{Sel}^{\ell\nu\ell\nu}$	$\mathrm{Sel}^{\mathrm{fin}}$	$\mathrm{Sel}^{\ell\nu\ell\nu}$	$\mathrm{Sel}^{\mathrm{fin}}$	$\mathrm{Sel}^{\ell\nu\ell\nu}$	$\mathrm{Sel}^{\mathrm{fin}}$
Dilepton								
ee	5.8 ± 5.8	5.8 ± 5.8	2.3 ± 2.3	(2.3)	(2.7)	(2.7)	(2.6)	(2.6)
$\mu\mu$	2.6 ± 0.6	0.3 ± 0.2	1.5 ± 0.5	0.4 ± 0.3	1.9 ± 0.5	0.9 ± 0.3	1.7 ± 0.5	0.5 ± 0.2
$\tau\tau$	16.5 ± 1.6	1.1 ± 0.4	15.7 ± 1.5	1.5 ± 0.5	14.9 ± 1.4	1.8 ± 0.5	15.1 ± 1.5	0.6 ± 0.3
Four-fermion								
eeee	(0.2)	(0.2)	0.2 ± 0.2	(0.2)	0.2 ± 0.2	(0.2)	0.2 ± 0.2	(0.2)
ee$\mu\mu$	1.6 ± 0.6	0.6 ± 0.3	0.6 ± 0.3	0.2 ± 0.2	1.0 ± 0.4	(0.2)	0.6 ± 0.3	0.2 ± 0.2
ee$\tau\tau$	2.4 ± 0.7	(0.2)	3.2 ± 0.8	0.2 ± 0.2	3.8 ± 0.9	0.2 ± 0.2	3.0 ± 0.8	0.2 ± 0.2
$\ell\ell\ell\ell$	(12.0)	(12.0)	(11.3)	(11.3)	36.6 ± 21.1	(12.2)	26.5 ± 18.7	(13.2)
Two-photon								
eeee	2.0 ± 1.4	(1.0)	3.0 ± 1.7	(1.0)	3.0 ± 1.7	(1.0)	3.0 ± 1.7	(1.0)
ee$\mu\mu$	(1.0)	(1.0)	2.0 ± 1.4	(1.0)	3.0 ± 1.7	(1.0)	3.0 ± 1.7	(1.0)
ee$\tau\tau$	8.1 ± 2.9	(1.0)	11.0 ± 3.3	(1.0)	3.0 ± 1.7	(1.0)	3.0 ± 1.7	(1.0)
Other								
$\nu\nu(\mathrm{n}\gamma)$	2.2 ± 1.0	(0.4)	3.2 ± 0.5	0.1 ± 0.1	3.2 ± 0.5	(0.1)	2.0 ± 0.6	(0.2)
ee(γ)	6.9 ± 6.9	(6.9)	(4.3)	(4.3)	1.7 ± 1.7	(1.7)	(2.6)	(2.6)
Total	48.1 ± 9.8	7.8 ± 5.8	42.7 ± 5.0	2.4 ± 0.7	72.5 ± 21.5	2.9 ± 0.6	58.1 ± 19.0	1.5 ± 0.5

Table 4.4: The expected background contamination, expressed as the accepted cross-section in the selected OPAL data, from several different sources using both the standard acoplanar charged lepton selection ($\mathrm{Sel}^{\ell\nu\ell\nu}$), and the full selection including tau rejection ($\mathrm{Sel}^{\mathrm{fin}}$). Where no events are selected a figure is given in brackets which represents the contamination which one selected event would represent. The errors are statistical.

4.3.3 Summary

The event selection and tau rejection described in section 4.3.1 is applied to the OPAL data recorded during 1999. Table 4.5 indicates the performance of the selection by listing the selection efficiency together with the total number of events selected from the data. The results for the standard acoplanar charged lepton selection, $\mathrm{Sel}^{\ell\nu\ell\nu}$, are shown together with those for the final selection, $\mathrm{Sel}^{\mathrm{fin}}$, which include additional cuts particular to the TGC measurement as well as the tau rejection. The selection is the same for data recorded at all centre-of-mass energies. An example of such an event recorded by OPAL at a centre-of-mass energy of 192 GeV is shown in figure 4.6.

The efficiency of the event selection is estimated by applying it to samples of events which simulate W-pair production which have been generated using KORALW [51,52]. These samples are listed in appendix A. For this investigation the evaluation of the selection efficiency is not critical since the result is not used, this is to merely illustrate the performance of the selection. In all cases, the selection efficiency, ε, is calculated using

$$\varepsilon = \frac{N^{\mathrm{sel\,ev}}}{N^{\mathrm{true\,ev}}},$$

where $N^{\mathrm{sel\,ev}}$ is the number of $\mathrm{WW} \to \ell\nu\ell\nu$ events selected, and $N^{\mathrm{true\,ev}}$ is the total number of true $\mathrm{WW} \to \ell\nu\ell\nu$ events in the generated sample. The results are presented for both the cases where the final states in the generated samples do and do not include taus. The performance of the selection is found to be reasonably constant over this energy range. The proportion of $\mathrm{WW} \to \ell\nu\ell\nu$ events passing the final selection including tau rejection, which still contain a tau is shown and it can be seen that 14% of events still contain at least one tau lepton. As previously discussed, these events are not problematic since they can still contain useful information in the measurement of the triple gauge couplings.

The number of events selected from the OPAL data are summarised together with the expected results from simulated events. The five-angle set for these events is reconstructed using the procedure described in section 4.2.1. The number of events reconstructed with two real solutions is also given in the table. The distributions for each of the five-angles observed in the total 1999 data and in simulated events is shown in figure 4.7. Also shown are the distributions expected for events simulating anomalous values for the triple gauge coupling λ. In particular it can be seen that the distribution for $\cos\theta_{\mathrm{W}}$ is expected to be significantly flatter for $\lambda = -1.0$ compared to $\lambda = +1.0$. In general, the distributions observed in data are consistent with those expected from simulated events although from this it is not possible to draw any conclusions regarding the values of the couplings in data. Finally, in table 4.5 the total expected number of background events is given, which is found to be extremely small.

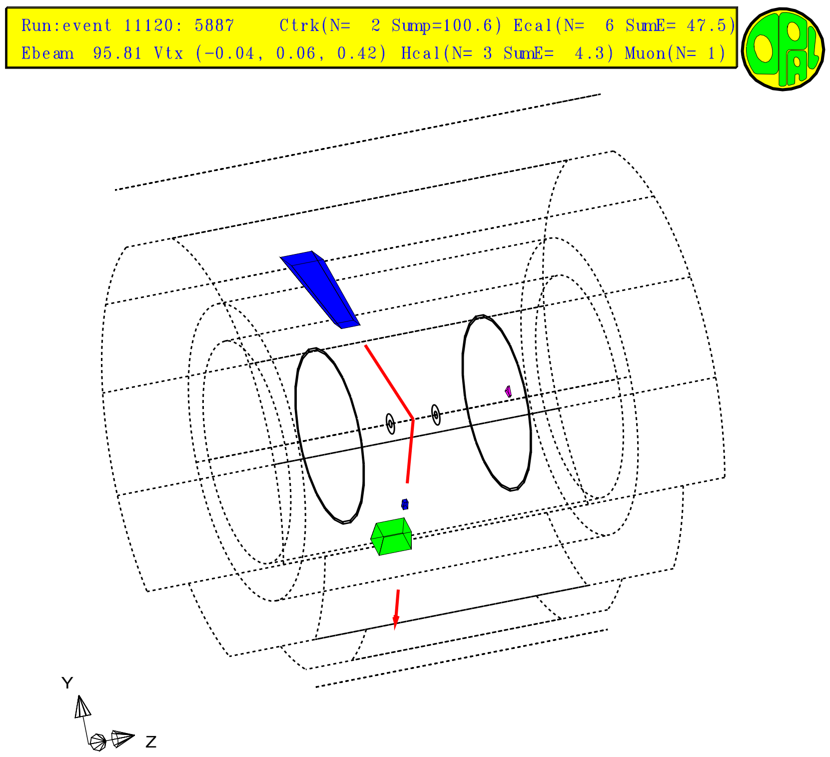

Figure 4.6: An example of an event recorded by OPAL at a centre-of-mass energy of 192 GeV which passes the $\mathrm{WW} \rightarrow \ell\nu\ell\nu$ selection and tau rejection. This event has the signature of an acoplanar electron-muon pair, where the upwards going electron leaves energy deposits in the electromagnetic calorimeter, denoted by the filled blocks, and the downwards going muon also leaves a signal in the muon chambers, indicated by the arrow.

	Event selection			
	192	196	200	202
Selection efficiency				
$\varepsilon(\mathrm{Sel}^{\ell\nu\ell\nu})$ for $\mathrm{WW} \to \ell\nu\ell\nu$ ($\ell = \mathrm{e}$, μ or τ)	$82.4 \pm 1.2\%$	$81.5 \pm 0.8\%$	$80.9 \pm 0.8\%$	$81.0 \pm 0.8\%$
$\varepsilon(\mathrm{Sel}^{\ell\nu\ell\nu})$ for $\mathrm{WW} \to \ell\nu\ell\nu$ ($\ell = \mathrm{e}$ or μ)	$87.0 \pm 1.8\%$	$85.7 \pm 1.3\%$	$85.5 \pm 1.3\%$	$86.1 \pm 1.3\%$
$\varepsilon(\mathrm{Sel}^{\mathrm{fin}})$ for $\mathrm{WW} \to \ell\nu\ell\nu$ ($\ell = \mathrm{e}$ or μ)	$73.0 \pm 1.6\%$	$69.6 \pm 1.1\%$	$68.7 \pm 1.1\%$	$67.9 \pm 1.1\%$
τ proportion	$14.1 \pm 0.6\%$	$13.9 \pm 0.5\%$	$14.2 \pm 0.5\%$	$14.0 \pm 0.5\%$
Selected number of events				
$\mathrm{Sel}^{\ell\nu\ell\nu}$	51	143	134	82
$\mathrm{Sel}^{\mathrm{fin}}$	19	55	52	31
Expected $\mathrm{Sel}^{\mathrm{fin}}$	20.0 ± 0.3	48.6 ± 0.6	53.3 ± 0.6	25.2 ± 0.3
$\mathrm{Sel}^{\mathrm{fin}}$ with two real solutions	15	41	37	23
Expected $\mathrm{Sel}^{\mathrm{fin}}$ with two real solutions	15.0 ± 0.3	36.2 ± 0.5	40.0 ± 0.6	19.1 ± 0.3
$\mathrm{Sel}^{\mathrm{fin}}$ Background	0.23 ± 0.17	0.18 ± 0.05	0.23 ± 0.05	0.05 ± 0.02

Table 4.5: The estimated selection efficiency and the selected number of events in the OPAL data for each energy point. The values are presented for the standard acoplanar charged lepton selection ($\mathrm{Sel}^{\ell\nu\ell\nu}$) and the final selection including tau rejection and other cuts ($\mathrm{Sel}^{\mathrm{fin}}$). The efficiencies are based on $\mathrm{WW} \to \ell\nu\ell\nu$ events where the final states either include or do not include taus. The total number of selected events is given together with the number reconstructed with two real solutions for the five-angles. The expected numbers determined using events simulated with all four-fermion final states are given with their Monte Carlo statistical error. The expected number of events arising from background processes is also given.

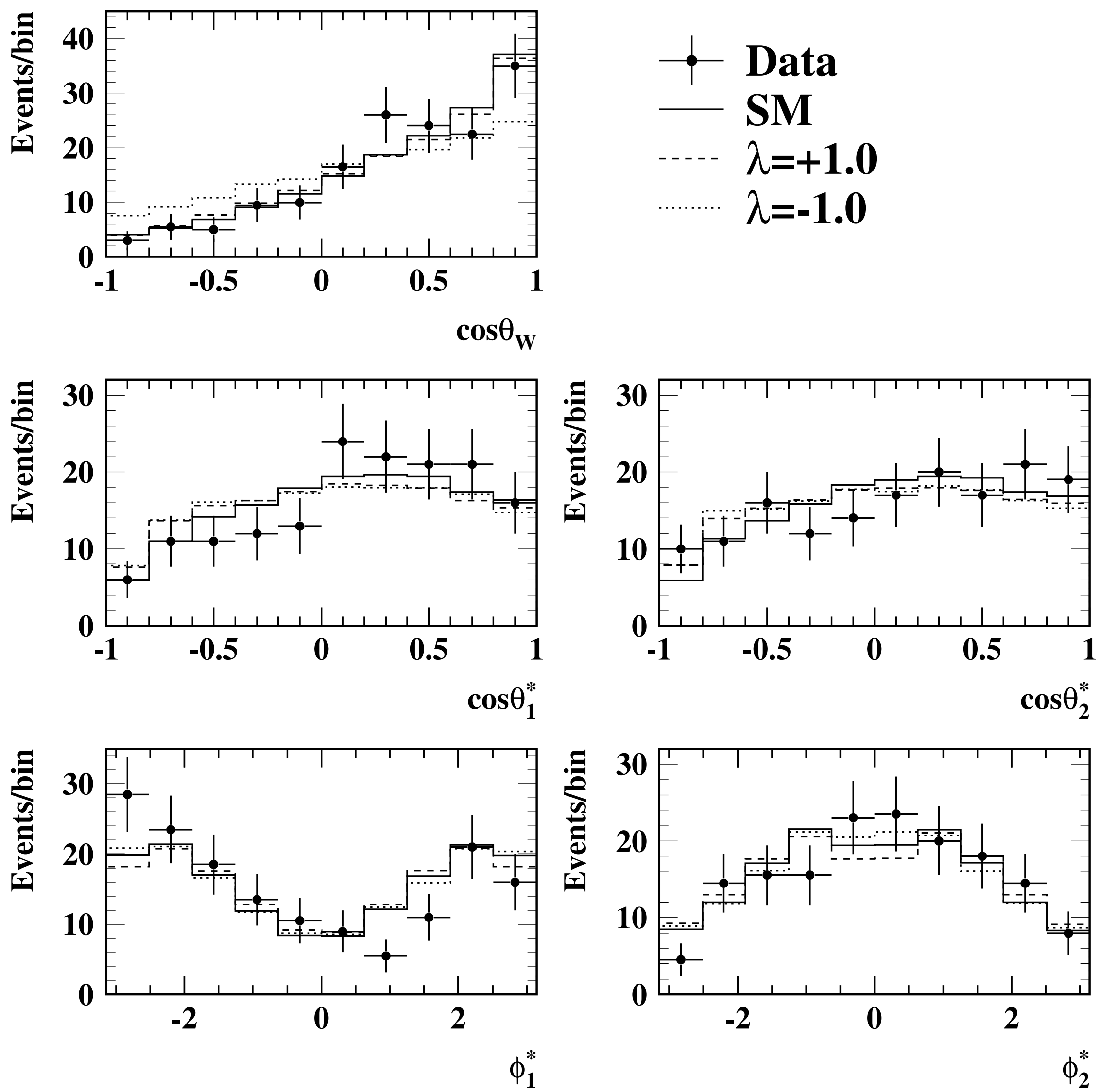

Figure 4.7: Distributions of the kinematic variables $\cos\theta_{\mathrm{W}}$, $\cos\theta_1^*$, ϕ_1^*, $\cos\theta_2^*$ and ϕ_2^* observed in $\mathrm{WW} \rightarrow \ell\nu\ell\nu$ events at OPAL. The angle $\cos\theta_{\mathrm{W}}$ is the production angle of the W^- boson. The angles $\cos\theta_1^*$ and ϕ_1^* ($\cos\theta_2^*$ and ϕ_2^*) are the polar and azimuthal decay angles of the charged lepton (antilepton) from the the W^- (W^+) in the rest frame of the W^- (W^+). All events enter with a weight of one including those events with two solutions for the five-angle set where each solution enters with a weight of a half. The histograms, normalised to the number of events observed in the OPAL data, show events simulated with Standard Model (SM) and anomalous couplings ($\lambda = \pm 1.0$)

Chapter 5

Extracting Triple Gauge Couplings

This chapter presents a measurement of the triple gauge boson coupling parameters using fully leptonic W-pair events recorded at OPAL during 1999. The selection of this sample of events was discussed in chapter 4. In general, the approach used to extract the TGC values from any sample of W-pair events is divided into two parts. The first uses a measurement of the total cross-section together with a knowledge of its dependence on the couplings to place limits upon them. The second and more powerful technique is presented in this chapter and examines the normalised multi-differential cross-sections.

At OPAL, the extraction of the TGC parameter values is performed for each W-pair channel separately since the treatment of the events differs greatly between channels. The different event topologies demand a separate event selection, reconstruction and five-angle set determination. However, since the standard OPAL W-pair TGC analyses make use of the 'Optimal Observables' technique to extract the couplings, once the five-angle set has been determined, the subsequent procedure for measuring κ_γ, λ and g_1^Z is similar for each channel. Each of the W-pair channels yields a separate set of measured couplings which can be combined to produce an overall measurement. Furthermore, these values can also be combined with those measured at other centre-of-mass energies and by other experiments to improve the constraints on them.

This chapter begins with a discussion of the techniques employed to extract the coupling values from event shape information. It then focuses on the application of the optimal observables technique to develop a fit procedure. Tests are done to evaluate its performance and systematic effects are evaluated. Finally, the results obtained when the fit is applied to OPAL data are presented.

5.1 Extraction Technique

The goal is to use the five-angle distributions shown in figure 4.7 to measure the triple gauge boson couplings. Several mathematical procedures exist to extract a parameter value from a sample of events. At OPAL, the optimal observables technique is used for W-pair events, but this is not the only one able to measure TGC values, for example, the couplings κ_γ and λ_γ are measured from single-W events using a binned maximum likelihood fit to the observed event rate and differential distributions [93]. Also at OPAL, semi-leptonic W-pair events are used to measure the CP violating couplings using a spin density matrix method [96]. At the other LEP collaborations, ALEPH performed a measurement of κ_γ, λ and g_1^Z at 189 GeV using an optimal observables method, and measured the C and P violating couplings with a generalised maximum likelihood analysis [100]. For 1999 data ALEPH employ the generalised maximum likelihood method [101]. The DELPHI collaboration uses both an extended and a binned maximum likelihood method making use of optimal variables to measure κ_γ, λ and g_1^Z at 189–202 GeV [104, 105]. The L3 collaboration uses both binned and unbinned maximum likelihood techniques for their measurements of κ_γ, λ and g_1^Z at 189–202 GeV [110, 112].

The effective Lagrangian which parameterises the TGCs was given in equation 4.1. This equation is linear in the coupling parameters and so the differential cross-section resulting from this Lagrangian has a quadratic dependence upon these couplings. This dependency may be parameterised as

$$\frac{\mathrm{d}\sigma}{\mathrm{d}\Omega}(\Omega, \vec{\alpha}) = S^{(0)}(\Omega) + \sum_i \alpha_i S_i^{(1)}(\Omega) + \sum_{i,j} \alpha_i \alpha_j S_{ij}^{(2)}(\Omega). \tag{5.1}$$

In this expression, the differential cross-section, $\frac{\mathrm{d}\sigma}{\mathrm{d}\Omega}$, is a function of the set of TGC parameters, $\vec{\alpha}$, and of Ω which is the set of phase-space variables. The term $\vec{\alpha}$ is a generic parameter representing the set of couplings being considered, in this analysis the set is $\{\vec{\alpha}\} \equiv \{\kappa_\gamma, \lambda, g_1^Z\}$. In equation 5.1 the α_i terms are defined so that their *deviations* from zero are being measured. For this reason the coupling set is usually $\{\Delta\kappa_\gamma, \lambda, \Delta g_1^Z\}$, these were introduced in section 4.1. The phase-space variables, denoted by Ω, which are considered in the case of an on-shell W decay is the five-angle set $\{\cos\theta_{\mathrm{W}}, \cos\theta_1^*, \phi_1^*, \cos\theta_2^*, \phi_2^*\}$ described in section 4.2. Finally, the S terms carry the information describing the $\vec{\alpha}$ dependence of $\mathrm{d}\sigma/\mathrm{d}\Omega$. Since equation 4.1 is linear in the coupling parameters, no further terms with higher powers of α are needed in the expansion of equation 5.1. Equation 5.1 has the form of a paraboloid in α, and if $\vec{\alpha}$ describes three different couplings, then the expression represents a three dimensional paraboloid function. The relevance of this functional form is important and will be discussed later.

Using the five-angle set, the aim is to measure $\vec{\alpha}$. This may be done by way of a 'maximum likelihood' fit in which $\vec{\alpha}$ is found when the product of the probability density function for the sample of events is at a maximum. The maximum likelihood has no sensitivity to the $\vec{\alpha}$ dependence of the total cross-section, but this can be included by performing an 'extended maximum likelihood' fit. This is a more direct way of estimating the parameters since it incorporates the whole of the kinematic information available, both the number of events and their distribution in phase-space. These methods, however, do not incorporate complications such as detector effects, initial and final state radiation and background events. All of these effects are most easily incorporated by using samples of Monte Carlo events which simulate them, and then comparing these events to the real data. This can be achieved by fitting the distributions of binned data within a 'binned maximum likelihood' fit. The problem with this approach is that since the phase-space variable set represents a five dimensional distribution, the number of bins rapidly becomes too large. If each of the five angular distributions is divided into just four bins, the total number of bins already exceeds 1 000, this means that an extremely large number of Monte Carlo events must be generated to populate them.

5.1.1 Optimal Observables Technique

An optimal observable is a variable which is defined to be maximally sensitive to the variation of a particular parameter. It was first used in the measurement of tau polarisation [129], and in triple gauge coupling analyses it is defined to be sensitive to the variation of a TGC parameter. The S terms in equation 5.1 dictate the TGC dependence of the differential cross-section. Consider a differential cross-section which is linearly dependent on a single parameter, α_1, such that $\frac{d\sigma}{d\Omega}(\Omega, \alpha_1) = S^{(0)}(\Omega) + \alpha_1 S_1^{(1)}(\Omega)$. The optimal observable for an event with a five-angle distribution, Ω, is defined as $\mathcal{O}(\Omega) = S_1^{(1)}(\Omega)/S^{(0)}(\Omega)$. The *mean* of the optimal observable, $\langle\mathcal{O}\rangle$, taken over the sample of events, alone contains the full information about the variation of the couplings [130, 131]. It can be seen from equation 5.1 that $S^{(0)}(\Omega)$ is the differential cross-section when $\vec{\alpha} = \vec{0}$, which is the Standard Model value, and $S_1^{(1)}(\Omega)$ describes its dependence on α_1. The result for the extraction of α_1 using this mean optimal observable will yield the maximum possible statistical precision on α_1. The important advantage over the binned maximum likelihood is the fact that $\langle\mathcal{O}\rangle$ is a single number, and not an angular distribution. So, for a sample of events, the optimal observables technique projects the five dimensional distributions onto a single variable without a loss in sensitivity to α_1, which is the parameter being measured.

A disadvantage of using the optimal observable is that the sensitivity of $\langle\mathcal{O}\rangle$ on the couplings is not actually linear and is only maximal for values of the couplings close to the point at which the differential cross-section has been expanded. In this case these are the Standard Model values. In the limit of small values of $\{\Delta\kappa_\gamma, \lambda, \Delta g_1^Z\}$, the full statistical information is available in $\langle\mathcal{O}\rangle$, but the sensitivity is less optimal for non-Standard Model values. To improve this, additional information contained in the quadratic dependence of the differential cross-section is included. Furthermore, where more than one parameter is being studied, the TGC sensitivity of Ω is contained in the complete set of observables [132, 133]

$$\begin{aligned} \mathcal{O}_i^{(1)}(\Omega) &= S_i^{(1)}(\Omega)/S^{(0)}(\Omega), \\ \mathcal{O}_{ij}^{(2)}(\Omega) &= S_{ij}^{(2)}(\Omega)/S^{(0)}(\Omega). \end{aligned} \tag{5.2}$$

$S^{(0)}(\Omega)$ is again the Standard Model differential cross-section, while $S_i^{(1)}(\Omega)$ and $S_{ij}^{(2)}(\Omega)$ parameterise its dependence on α_i and $\alpha_i\alpha_j$. $\mathcal{O}^{(1)}(\Omega)$ and $\mathcal{O}^{(2)}(\Omega)$ are called the first and second order optimal observables respectively.

In this treatment, the TGC parameter set has been defined so that they are all zero in the Standard Model. If a single parameter is to be extracted, it is allowed to vary from zero while restricting the remaining couplings to zero. In this case the only mean observables which carry information about α_1 for example are $\langle\mathcal{O}_1^{(1)}\rangle(\Omega)$ and $\langle\mathcal{O}_{11}^{(2)}\rangle(\Omega)$. If two TGC parameters are allowed to vary from their Standard Model values, there are a total of five observables; the two first order observables $\langle\mathcal{O}_1^{(1)}\rangle(\Omega)$ and $\langle\mathcal{O}_2^{(1)}\rangle(\Omega)$, the two diagonal second order observables $\langle\mathcal{O}_{11}^{(2)}\rangle(\Omega)$ and $\langle\mathcal{O}_{22}^{(2)}\rangle(\Omega)$, and the off-diagonal second order observable $\langle\mathcal{O}_{12}^{(2)}\rangle(\Omega)$ $(= \langle\mathcal{O}_{21}^{(2)}\rangle(\Omega))$. Finally, for fits in which three parameters are allowed to vary there are a total of nine observables. Most of the sensitivity to the TGCs lie in the first order observables, but the second order ones can still provide useful information in the fit.

5.1.2 Chi-squared Fit

The optimal observable values are calculated for each event separately and then the mean values of the observables, taken over the whole sample, are used in the fit procedure. To extract the couplings from these events, a sample of generated events, incorporating detector effects for example, are used in the fit. These generated events are called the 'reference' samples and they are used to determine a *calibration curve* to which the recorded data is compared. The idea is to use Monte Carlo generated events to produce calibration curves which directly relate the mean optimal observable values to the coupling values. The same mean optimal observable values from the recorded events are compared to the calibration curves so that the coupling values can be read off.

The calibration curves describe the expectation value, $E[\mathcal{O}](\alpha)$, of the observables as a function of the couplings. Take for example the case where one parameter, α_i, is allowed to vary from its Standard Model value, and only the calibration curve for the first order optimal observable, $\mathcal{O}_i^{(1)}$, is being used, then the limit of the expression

$$\Big(\langle\mathcal{O}_i^{(1)}\rangle - E[\mathcal{O}_i^{(1)}](\alpha_0)\Big) \rightarrow 0 \tag{5.3}$$

returns α_0 which is the best estimate of α_i. To reiterate, $E[\mathcal{O}_i^{(1)}](\alpha_i)$ is the calibration curve obtained from simulated events and $\langle\mathcal{O}_i^{(1)}\rangle$ is measured from the sample of events from which α_i is being extracted. In reality, the value of α_0 is extracted by performing the minimisation of the chi-squared function

$$\chi^2(\alpha_i) = \frac{\Big(\langle\mathcal{O}_i^{(1)}\rangle - E[\mathcal{O}_i^{(1)}](\alpha_i)\Big)^2}{\sigma^2}, \tag{5.4}$$

where σ here is the statistical uncertainty with which $\langle\mathcal{O}_i^{(1)}\rangle$ can be measured. A plot of the value of $\chi^2(\alpha_i)$ as a function of α_i is called the chi-squared curve. For a fit with a well defined convergence value, this curve should be approximately parabolic in shape with a symmetric minimum positioned at α_0. Fit techniques involving a minimum chi squared, and maximum log likelihood are actually quite similar, and in the case of a fit which behaves in a Gaussian fashion, the chi-squared and log likelihood curves are directly related, the chi-squared values are minus two times the log likelihood values. Furthermore, in the Gaussian case, the one sigma error on the α_0 estimation is readily obtained from the values of α at which the chi-squared curve rises to one unit above its minimum. This is the same as the points at which the log likelihood falls to 0.5 below its peak value.

In the chi-squared function of equation 5.4, one parameter is being extracted using only the first order mean optimal observable. Since not all of the TGC dependency of α_i is carried by $\langle\mathcal{O}_i^{(1)}\rangle$ it is useful to introduce a fit which allows also the second order optimal observable values to be employed. The χ^2 function to be minimised can be written out explicitly as

$$\begin{aligned}
\chi^2(\alpha_i) &= \left(\langle\mathcal{O}_i^{(1)}\rangle - E[\mathcal{O}_i^{(1)}](\alpha_i)\right)\left(V^{-1}(\alpha_i)\right)_{11}\left(\langle\mathcal{O}_i^{(1)}\rangle - E[\mathcal{O}_i^{(1)}](\alpha_i)\right) \\
&+ \left(\langle\mathcal{O}_i^{(1)}\rangle - E[\mathcal{O}_i^{(1)}](\alpha_i)\right)\left(V^{-1}(\alpha_i)\right)_{12}\left(\langle\mathcal{O}_{ii}^{(2)}\rangle - E[\mathcal{O}_{ii}^{(2)}](\alpha_i)\right) \\
&+ \left(\langle\mathcal{O}_{ii}^{(2)}\rangle - E[\mathcal{O}_{ii}^{(2)}](\alpha_i)\right)\left(V^{-1}(\alpha_i)\right)_{21}\left(\langle\mathcal{O}_i^{(1)}\rangle - E[\mathcal{O}_i^{(1)}](\alpha_i)\right) \\
&+ \left(\langle\mathcal{O}_{ii}^{(2)}\rangle - E[\mathcal{O}_{ii}^{(2)}](\alpha_i)\right)\left(V^{-1}(\alpha_i)\right)_{22}\left(\langle\mathcal{O}_{ii}^{(2)}\rangle - E[\mathcal{O}_{ii}^{(2)}](\alpha_i)\right). \quad (5.5)
\end{aligned}$$

Again, $E[\mathcal{O}]$ are the calibration curves describing the expectation value of $\mathcal{O}$ as a function of α_i and $\langle\mathcal{O}\rangle$ are the measured values for the sample of events from which α_i is being extracted. V is the covariance matrix which is a function of α_i. In this fit to a single parameter only $\mathcal{O}_i^{(1)}$ and $\mathcal{O}_{ii}^{(2)}$ is used to extract α_i since little extra information is expected to be gained from the other terms, $\mathcal{O}_j^{(1)}$, $\mathcal{O}_{ij}^{(2)}$ and $\mathcal{O}_{jj}^{(2)}$, with $j \neq i$.

For fits in which two or three parameters are allowed to vary simultaneously, some or all of the $\mathcal{O}_{ii}^{(2)}$ and $\mathcal{O}_{ij}^{(2)}$ observables will be utilised. For these multi-parameter fits it is easier to make a change of notation and denote the observables just by $\mathcal{O}_i$, where i represents either the first *or* second order observables, and any of the combinations ii, ij or ji. With this notation, the indices i=1–3 represent the first order observables, $\mathcal{O}_i^{(1)}$, the indices i=4–6 represent the second order diagonal observables, $\mathcal{O}_{ii}^{(2)}$, and i=7–9 represent the second order off-diagonal observables, $\mathcal{O}_{ij}^{(2)}$. The chi-squared fit of equation 5.5 is easily extended to fits in which several TGC parameters are evaluated simultaneously. In these fits more than one coupling is allowed to vary from its Standard Model value and then the chi-squared value depends upon several parameters so that

$$\chi^2(\vec{\alpha}) = \sum_i \sum_j \left(\langle\mathcal{O}_i\rangle - E[\mathcal{O}_i](\vec{\alpha})\right)\left(V_{ij}^{-1}(\vec{\alpha})\right)\left(\langle\mathcal{O}_j\rangle - E[\mathcal{O}_j](\vec{\alpha})\right). \quad (5.6)$$

The chi-squared function for this multi-parameter fit is nearly identical to that for the one parameter fits except that now the expected mean observables, $E[\mathcal{O}]$, and the covariance matrix, V, are functions of all of the parameters being varied in the fits. Furthermore, the indices i and j each run from one to nine and they label the nine observables which are available for use in the fit. All of the relevant first and second order observables, including the diagonal and cross-terms, are included in the function.

The elements of the covariance matrix, V_{ij}, are functions of the optimal observables. The relationship is normally expressed as $V_{ij} = \mathrm{cov}(\mathcal{O}_i, \mathcal{O}_j)$, and they are calculated in the normal way using

$$\mathrm{cov}(\mathcal{O}_i, \mathcal{O}_j) = \langle \mathcal{O}_i \times \mathcal{O}_j \rangle - \langle \mathcal{O}_i \rangle \langle \mathcal{O}_j \rangle. \tag{5.7}$$

In a one parameter fit, V is a two-by-two matrix since two observables are used, whereas in a three parameter fit there are a total of nine observables, so the covariance matrix is nine-by-nine. The matrix, V^{-1}, is found by performing a matrix inversion of the covariance matrix. The covariance matrix is actually calculated from the expected observables, $E[\mathcal{O}]$, rather than from the sample from which the parameters are being extracted since it is found that the fit behaves much more stably with this larger sample and is also less biased [134].

5.1.3 Optimal Observable Evaluation

Equations 5.2 define the optimal observables in terms of S. These are determined analytically on an event-by-event basis using a differential cross-section calculator package which returns their tree level values [88]. This calculator requires as inputs the centre-of-mass energy, the five-angle set for the event, and the couplings for which $\frac{\mathrm{d}\sigma}{\mathrm{d}\Omega}$ is to be calculated, together with various electroweak parameters. For each individual event, that is for one five-angle set, Ω, the package is used to determine $\frac{\mathrm{d}\sigma}{\mathrm{d}\Omega}(\vec{\alpha})$ for both Standard Model and anomalous values of the couplings. From the relationship of equation 5.1 it can be seen that for Standard Model couplings, $\frac{\mathrm{d}\sigma}{\mathrm{d}\Omega}(\vec{\alpha} = \vec{0}) = S^{(0)}$, and where one coupling is changed from zero to a value $\alpha_i = \pm 1$, then $\frac{\mathrm{d}\sigma}{\mathrm{d}\Omega}(\alpha_i = \pm 1) = S^{(0)} \pm S^{(1)}_i + S^{(2)}_{ii}$. Using these relationships, together with those in which two couplings are deviated from zero to plus one, and also the definitions of equation 5.2, the optimal observable values for the event are given by

$$\begin{aligned}
\mathcal{O}_i^{(1)} &= \frac{\frac{\mathrm{d}\sigma}{\mathrm{d}\Omega}(\alpha_i=+1)-\frac{\mathrm{d}\sigma}{\mathrm{d}\Omega}(\alpha_i=-1)}{2\frac{\mathrm{d}\sigma}{\mathrm{d}\Omega}(\vec{\alpha}=\vec{0})}, \\
\mathcal{O}_{ii}^{(2)} &= \frac{\frac{\mathrm{d}\sigma}{\mathrm{d}\Omega}(\alpha_i=+1)+\frac{\mathrm{d}\sigma}{\mathrm{d}\Omega}(\alpha_i=-1)-2\frac{\mathrm{d}\sigma}{\mathrm{d}\Omega}(\vec{\alpha}=\vec{0})}{2\frac{\mathrm{d}\sigma}{\mathrm{d}\Omega}(\vec{\alpha}=\vec{0})}, \\
\mathcal{O}_{ij}^{(2)} &= \frac{\frac{\mathrm{d}\sigma}{\mathrm{d}\Omega}(\alpha_i=\alpha_j=+1)-\frac{\mathrm{d}\sigma}{\mathrm{d}\Omega}(\alpha_i=+1)-\frac{\mathrm{d}\sigma}{\mathrm{d}\Omega}(\alpha_j=+1)+\frac{\mathrm{d}\sigma}{\mathrm{d}\Omega}(\vec{\alpha}=\vec{0})}{\frac{\mathrm{d}\sigma}{\mathrm{d}\Omega}(\vec{\alpha}=\vec{0})}.
\end{aligned} \tag{5.8}$$

This procedure is used to calculate the optimal observable values for each event separately once the five-angle set has been reconstructed for the event. The distributions for the first and second order optimal observables $\mathcal{O}_2^{(1)}$ and $\mathcal{O}_{22}^{(2)}$ for events recorded and simulated at a centre-of-mass energy of 196 GeV are shown in figure 5.1. These plots show the distributions in recorded data together with the expected distributions using events simulated with both Standard Model and anomalous couplings. The optimal observable distributions have a clear sensitivity to the TGCs.

When calculating the mean of the $\mathcal{O}$ distribution only values satisfying $\mid \mathcal{O} \mid < 20.0$ are retained. This cut removes about 0.1% of the events and it is intended to exclude the very occasional events with particularly large $\mid \mathcal{O} \mid$ values which are found to have an effect on the accuracy of the fit results. A similar truncation is employed in the OPAL semi-leptonic analysis.

5.1.4 Paraboloid Functions

The construction of a calibration curve relies upon knowing how the expected values of the mean optimal observables vary as a function of the couplings. It is useful to be able to parameterise this dependency so that the mean optimal observable can be calculated within the fit procedure for any value of the coupling set. It has already been stated that this parameterisation will be derived using a sample of simulated events, this should then include in the fit all of the effects, such as those due to the detector, or initial and final state radiation. The functional form of the parameterisation can be predicted analytically, therefore, using several samples of events generated with both Standard

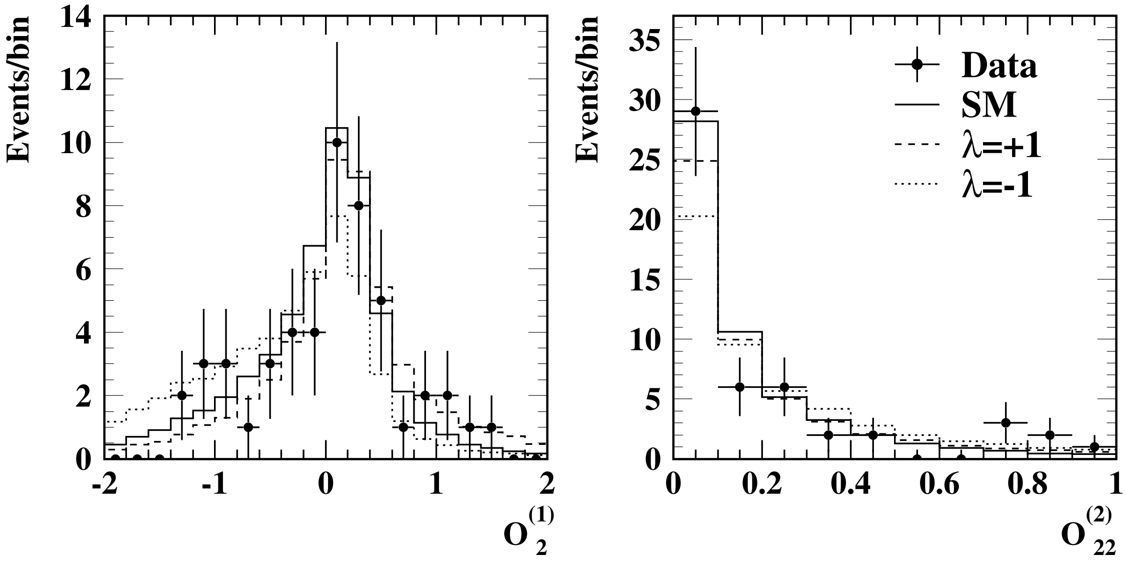

Figure 5.1: The optimal observable distributions for the first order $\mathcal{O}_2^{(1)}$ and the second order $\mathcal{O}_{22}^{(2)}$ observables corresponding to the TGC parameter λ. The dots represent OPAL data recorded at a centre-of-mass energy of 196 GeV. The histograms, normalised to the number of events observed in the OPAL data, show events simulating Standard Model (SM) and anomalous couplings ($\lambda = \pm 1.0$).

Model and anomalous couplings it is possible to calculate the parameterisation. The expected mean observable values can then be obtained for any TGC set by interpolating between and extrapolating beyond these known values.

The expected mean value of, for example, the first order optimal observable $\mathcal{O}_i^{(1)}(\Omega)$, denoted by $E[\mathcal{O}_i^{(1)}]$ is given by

$$\begin{aligned} E[\mathcal{O}_i^{(1)}] &= \frac{1}{\sigma_{\text{acc}}} \int \mathcal{O}_i^{(1)}(\Omega) \mathrm{d}\sigma(\Omega), \\ &\equiv \frac{1}{\sigma_{\text{acc}}} \int \mathcal{O}_i^{(1)}(\Omega) \frac{\mathrm{d}\sigma(\Omega)}{\mathrm{d}\Omega} \mathrm{d}\Omega. \end{aligned} \tag{5.9}$$

As usual, Ω represents the phase-space variables. The expression contains an integral over the cross-section, σ, and it is normalised to σ_{acc} which represents the accepted cross-section, $\int \mathrm{d}\sigma(\Omega) \left(= \int \frac{\mathrm{d}\sigma(\Omega)}{\mathrm{d}\Omega}\mathrm{d}\Omega\right)$. The form of the differential cross-section, $\frac{\mathrm{d}\sigma(\Omega)}{\mathrm{d}\Omega}$, as a function of the three TGC parameters is already known from equation 5.1 to be that of a three dimensional paraboloid. Crucially, since both $\mathcal{O}_i^{(1)}(\Omega)$ and Ω are independent of the TGC parameters, the αs in equation 5.1 are unaffected by the integral over Ω in equation 5.9, and they can be moved outside the integral. This means that $\int \mathcal{O}_i^{(1)}(\Omega)\mathrm{d}\sigma(\Omega)$ itself has the TGC functional form of a paraboloid with the $S_k^{(a)}(\Omega)$ terms in equation 5.1 replaced by $\mathcal{O}_i^{(1)}(\Omega) \times S_k^{(a)}(\Omega)$. Thus both σ_{acc} and $\sigma_{\mathrm{acc}} \times E[\mathcal{O}_i^{(1)}]$ are paraboloids in the TGC parameters, and therefore it is possible to determine their behaviour across all values of the couplings.

To be specific, the paraboloid function referred to is given by

$$paraboloid(\vec{\alpha}) = C^{(0)} + \sum_i \alpha_i C_i^{(1)} + \sum_{i,j} \alpha_i \alpha_j C_{ij}^{(2)} \tag{5.10}$$

where C are the paraboloid coefficients. The function is uniquely defined once the values of the coefficients are known. They are extracted using a procedure similar to the approach described in section 5.1.3 where the $\mathcal{O}$ values for a given event are calculated from functions of the differential cross-section for Standard Model and anomalous coupling values. The value of $paraboloid(\vec{\alpha})$ is evaluated for certain values of the TGC set $\vec{\alpha}$. For a three dimensional paraboloid there are a total of ten coefficients and a total of ten different $\vec{\alpha}$ sets are required to determine them. These $\vec{\alpha}$ sets are sometimes called the *basis points* and the ones used are

$$\begin{aligned}(\alpha_1, \alpha_2, \alpha_3) \quad = \quad & (0,0,0), \\ & (\pm 1,0,0),(0,\pm 1,0),(0,0,\pm 1), \\ & (+1,+1,0),(+1,0,+1),(0,+1,+1).\end{aligned}$$

The discussion following equation 5.9 can be extended to all optimal observables and not just $\mathcal{O}_i^{(1)}(\Omega)$. Therefore, both σ_{acc} and $\sigma_{\mathrm{acc}} \times E[\mathcal{O}]$ for all nine $\mathcal{O}$ types are paraboloids in the TGC parameters. In general, the expectation value for the optimal observable, $E[\mathcal{O}]$, is derived from the quotient of the two paraboloids which is given by

$$E[\mathcal{O}] = \frac{\sigma_{\mathrm{acc}} \times E[\mathcal{O}]}{\sigma_{\mathrm{acc}}}. \tag{5.11}$$

So, once the paraboloids in the numerator and denominator have been derived from the samples of simulated events, the expected mean optimal observables can be calculated for any value of the TGC parameters and the fits of equations 5.5 and 5.6 can be performed. Figure 5.2 shows $E[\mathcal{O}]$ as a function of each TGC parameter for each of the nine optimal observables for events simulated at 200 GeV. These curves *are* the calibration curves from which the couplings in the recorded data can be read off. Using a similar argument it can also be shown that $\sigma_{\mathrm{acc}} \times \mathrm{cov}(\mathcal{O}_i, \mathcal{O}_j)$ also has the form *paraboloid*$(\vec{\alpha})$, and so the covariance matrix, V_{ij}, in the chi-squared fit of equation 5.6 is given by

$$V_{ij} = \mathrm{cov}(\mathcal{O}_i, \mathcal{O}_j) = \frac{\sigma_{\mathrm{acc}} \times \mathrm{cov}(\mathcal{O}_i, \mathcal{O}_j)}{\sigma_{\mathrm{acc}}}. \tag{5.12}$$

The covariance matrix which enters into the chi-squared function can therefore itself be a function of the TGC parameters and can vary within the fit. It was found however that using this TGC dependent covariance matrix produced biases in the extracted parameters. Instead, the covariance matrix which is employed in the fits is the one determined from events simulated using Standard Model couplings.

In order to perform the chi-squared fit to the mean optimal observables of a sample of events, the only necessary inputs are the expected behaviour of σ_{acc}, $\sigma_{\mathrm{acc}} \times E[\mathcal{O}]$ and $\mathrm{cov}(\mathcal{O}_i, \mathcal{O}_j)$ which are all derived from simulated events. For a one parameter fit to α_1 where two mean optimal observables, $\mathcal{O}_1^{(1)}$ and $\mathcal{O}_{11}^{(2)}$ are used, the necessary inputs to the fit are σ_{acc}, the two $\sigma_{\mathrm{acc}} \times E[\mathcal{O}]$ parameterisations, one for each observable, and the four elements of the Standard Model two-by-two covariance matrix. Furthermore, for a complete three parameter fit where each is allowed to vary from its Standard Model value, the necessary inputs are σ_{acc}, nine $\sigma_{\mathrm{acc}} \times E[\mathcal{O}]$ parameterisations, and the 81 elements of the Standard Model nine-by-nine covariance matrix.

5.1.5 Monte Carlo Reweighting

To determine the paraboloid parameters, σ_{acc} and $\sigma_{\mathrm{acc}} \times E[\mathcal{O}]$ must be evaluated at the ten basis points. One approach is to generate ten different samples of events, each simulating the coupling set of one of the basis points. This requires a large number of events, therefore a more favourable approach is to use a single sample of events which

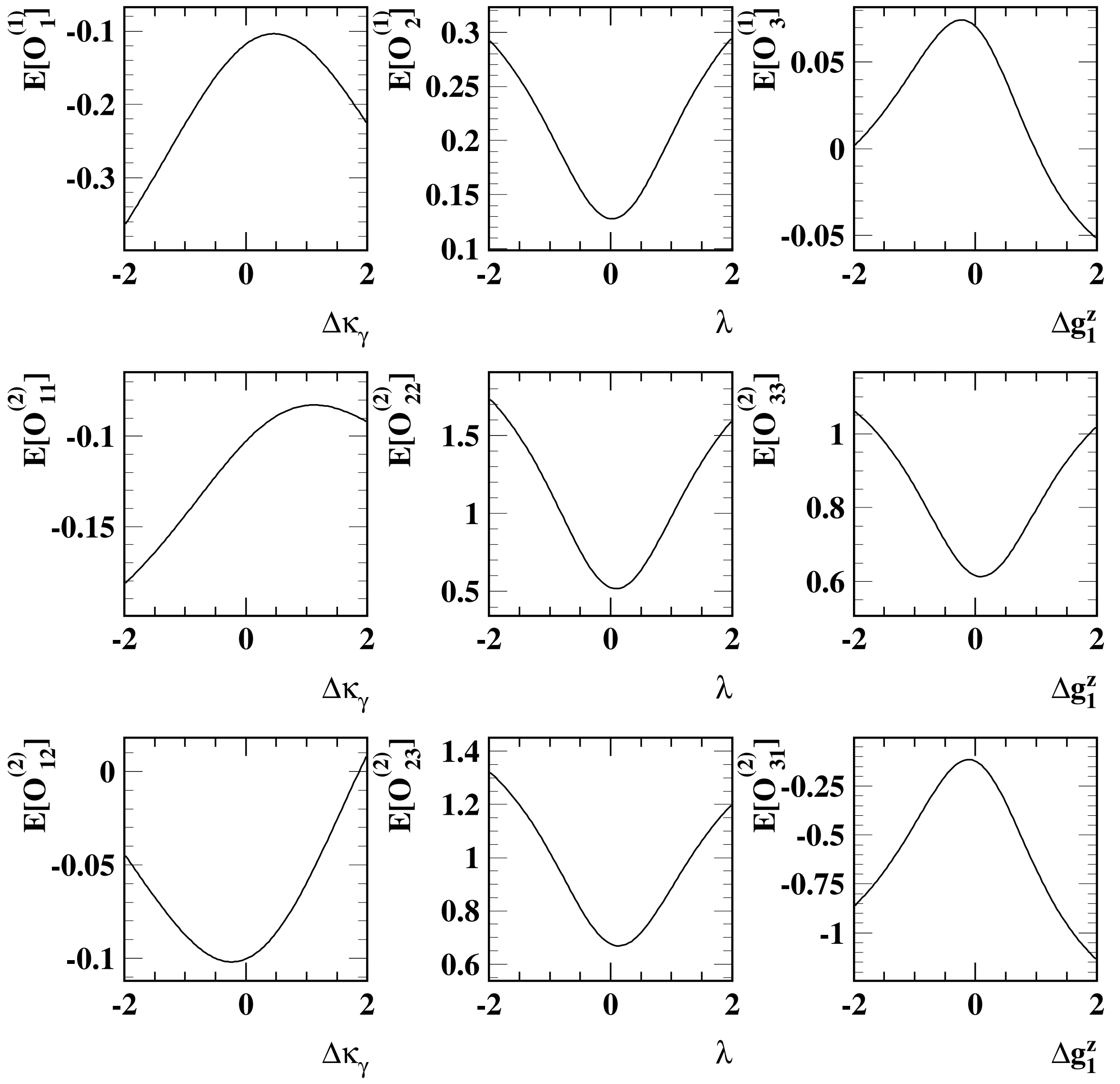

Figure 5.2: The expected mean optimal observable, $E[\mathcal{O}]$, for each of the nine optimal observables as a function of a TGC parameter. The subscript indicates which TGC parameter the observable corresponds to ($\Delta\kappa_\gamma$=1,λ=2,Δg_1^Z=3). These curves are the paraboloid functions obtained from events simulated with a centre-of-mass energy of 200 GeV.

is treated so that it mimics a sample with some other coupling values. This is achieved by reweighting the events.

This reweighting technique uses the fact that the TGC parameter values change the probability of a certain region of phase space being populated with events. So, if an event is generated with a five-angle distribution which is more probable for some other set of couplings, then the optimal observable values for that event should be weighted more highly for this other set of couplings. Suppose that for a sample of events generated with $\vec{\alpha} = (0, 0, 0)$ there are n_{a} events in some region of phase space $[\Omega, \Omega + \Delta\Omega]$. For a different sample of events generated with the same luminosity but with $\vec{\alpha} = (+1, 0, 0)$ there may be n_{b} events. The value of the optimal observable for events within $[\Omega, \Omega + \Delta\Omega]$ might lie in the range $[\mathcal{O}, \mathcal{O} + \Delta\mathcal{O}]$. This region of the $\mathcal{O}$ distribution filled by Monte Carlo events generated with $\vec{\alpha} = (+1, 0, 0)$ can be obtained from Monte Carlo events generated with $\vec{\alpha} = (0, 0, 0)$ by weighting this region of the $\mathcal{O}$ spectrum by a factor $n_{\mathrm{b}}/n_{\mathrm{a}}$ [135]. The $\mathcal{O}$ distribution for each basis point is obtained by calculating for each event, k, a weight, $\omega_k(\vec{\alpha}_{\mathrm{new}})$, given by

$$\omega_k(\vec{\alpha}_{\mathrm{new}}) = \frac{\mathrm{d}\sigma(\Omega_{\mathrm{k}}, \vec{\alpha}_{\mathrm{new}})}{\mathrm{d}\sigma(\Omega_{\mathrm{k}}, \vec{\alpha}_{\mathrm{gen}})} = \frac{\mid \mathcal{M}(\Omega_k, \vec{\alpha}_{\mathrm{new}}) \mid^2}{\mid \mathcal{M}(\Omega_k, \vec{\alpha}_{\mathrm{gen}}) \mid^2}. \tag{5.13}$$

In this expression, $\vec{\alpha}_{\mathrm{gen}}$ are the TGC parameter values which were used to generate the Monte Carlo sample and $\vec{\alpha}_{\mathrm{new}}$ are the values to which the events are being reweighted. In practice, this calculation is achieved by determining the ratio of the matrix elements, $\mid \mathcal{M} \mid^2$, associated with the event. Monte Carlo samples generated with the EXCALIBUR program [50] are used since it is possible to access the matrix element value for an event which has already been generated with $\vec{\alpha}_{\mathrm{gen}}$ as well as for the event had it been generated with $\vec{\alpha}_{\mathrm{new}}$. The inputs necessary to determine $\mid \mathcal{M} \mid^2$ are the four-vectors of the four final state fermions, their assigned flavours, the values of $\vec{\alpha}$, the centre-of-mass energy of the event, and the mass and width of the W boson, as well as other electroweak parameters.

The expected mean optimal observable for a sample of events with TGC parameters,

$\vec{\alpha}_{\text{new}}$, calculated from a sample of N events generated with $\vec{\alpha}_{\text{gen}}$ is given by

$$E[\mathcal{O}](\vec{\alpha}_{\text{new}}) = \frac{\sum_{k=1}^{N} \omega_k(\vec{\alpha}_{\text{new}}) \mathcal{O}(\Omega_k, \vec{\alpha}_{\text{gen}})}{\sum_{k=1}^{N} \omega_k(\vec{\alpha}_{\text{new}})}. \tag{5.14}$$

Using this technique, the simulated events can be reweighted to all of the ten basis points necessary to determine the paraboloid parameters. In principle, only one sample of Monte Carlo events is necessary for the complete analysis. However, some regions of phase space, which may be sparsely populated by events in this sample, might have a much larger cross-section for events with some other coupling values. As a result, the $\omega_k(\vec{\alpha}_{\text{new}})$ weight could be very large and the $E[\mathcal{O}](\vec{\alpha}_{\text{new}})$ value could experience large statistical fluctuations. To address this problem, several EXCALIBUR Monte Carlo samples generated with a range of anomalous couplings are used, and they are *all* reweighted to each of the basis points. A list of the Monte Carlo reference samples used in this analysis is given in appendix A.

5.1.6 Overview of Fit Procedure

The procedure used to extract the TGC values uses a chi-squared fit between the mean values of the optimal observables calculated from data and Monte Carlo generated events. For each event the five-angle set is reconstructed and each of the nine optimal observables are determined using an analytical differential cross-section calculator. The Monte Carlo events used to produce the calibration curves, called the 'reference samples', are reweighted to the ten basis points so that the paraboloid parameters can be determined. The expectation value of the mean optimal observable may then be extrapolated to all coupling values.

The chi-squared fit, whose minimisation is performed numerically by a program called MINUIT [136], returns a chi-squared curve which is plotted as a function of the fitted coupling. The results for the measurement of a TGC parameter consists of both the central value of the fit, and also the uncertainty on that value.

- The **central value** is equivalent to the coupling value at which the chi-squared curve is at its minimum. MINUIT locates this minimum and also returns the corresponding coupling value.

- The value which is quoted for the **error** on the central value is the one sigma uncertainty. The properties of the chi-squared curve were discussed in section 5.1.2. The one sigma uncertainty in a one parameter fit is taken to be the shift in the parameter value when the chi-squared curve rises to one unit above its minimum. Again, these values are returned by MINUIT. The shape of the chi-squared curve is not normally symmetric, therefore these one sigma deviations above and below the central value may not be equal, and it is more usual to quote one sigma values which are asymmetric.

It is not unusual for the chi-squared curve to exhibit double minima behaviour where two separate coupling values are successful at describing the data, the deeper one reflecting the preferred coupling value. This type of chi-squared curve can be problematic since it is no longer clear what the significance of the two central values and their uncertainties are.

The three TGC parameters being measured are (κ_γ,λ,g_1^Z). Several different fits are performed to extract these couplings, namely the one, two and three parameter fits, indicating the number of parameters which are allowed to vary from their Standard Model value. The more model-independent fit, and therefore the one most sensitive to new physics beyond the Standard Model which is expected to manifest itself as an anomaly in all or any of the couplings, is the three parameter fit in which all three parameters are allowed to vary simultaneously. In the two parameter fits, each one in turn is fixed to a constant value while the other two are allowed to vary. Finally, a total of three independent one parameter fits are performed, these are statistically the most stable and the easiest to combine with other measurements. In the one parameter fits only the optimal observables which are directly sensitive to the parameter being fitted is used, so for example when fitting the parameter α_1, the first order, $\mathcal{O}_1^{(1)}$, and second order, $\mathcal{O}_{11}^{(2)}$, mean observables are used in the fit. In the two and three parameter fits, however, all nine mean observables are utilised.

The simulated events which are used as the reference samples are generated using the EXCALIBUR program since these can be readily reweighted. Furthermore, these events are generated with all the four-fermion processes in which an $\ell\nu\ell\nu$ final state may exist. The motivation for using these events to construct the calibration curves is that they best represent the physics of the selected events. The selected OPAL data are dominantly $\ell\nu\ell\nu$ events, and since there are no requirements on the need for them to arise from W-pair production, they may contain other processes, such as single-W and Z-pairs, leading to the same final state. Before a Monte Carlo sample is used, those events which were generated without an $\ell\nu\ell\nu$ final state are removed. The remaining events are subjected to the same selection and tau rejection criterion as applied to the OPAL data.

5.2 Fit Tests

The sample of events from which the TGC values are being extracted are ultimately the recorded OPAL data, however, when testing the fit procedure this is normally a generated sample, referred to as the 'test' sample. The advantage of using simulated events as a test sample is that they have high statistics, so the fit procedure can be tested in the high statistics limit as well as at the same statistics as the OPAL data. Furthermore, these events simulate anomalous as well as Standard Model coupling values, so the reliability of the central value returned by the fit procedure can also be tested. In cases where a sample of Monte Carlo events is being treated as a test sample, those same events are not included in the reference sample. This ensures that the test sample is statistically independent of the reference sample.

5.2.1 Low Statistics Fit Tests

In order to test the expected performance of the fit procedure on the small number of selected events in the OPAL data, which was presented in the Sel$^{\mathrm{fin}}$ row in table 4.5, the fit is performed on test samples having the same statistics. The test events are from four-fermion samples generated both with Standard Model and anomalous coupling values. In each test, 10 000 separate subsamples are used where each one is subjected to the full fit procedure, either the one, two or three parameter fit. This set of 10 000 individual fits provides useful information about the results expected when the fit is applied to the OPAL data. In particular it provides an estimate of the expected one sigma fit uncertainty. It also provides a check on this estimate and therefore the possible need to apply a scaling to it.

There are insufficient Monte Carlo statistics to provide 10 000 or more *independent* subsamples with the size of the OPAL data, therefore, a procedure is followed where events are extracted at random from the complete Monte Carlo test sample to make up the 10 000 individual subsamples. This technique is expected to provide fit results which are, for this purpose, sufficiently independent [137]. An estimate of the expected one sigma uncertainty in the real data is derived by evaluating the mean of the uncertainty over the 10 000 test fits. This average expected error, together with its root mean square, is summarised in table 5.1 for the one and three parameter fits at the four centre-of-mass energies. All of these test samples have been generated with Standard Model couplings. This table demonstrates the relative sensitivity of the fit to the three couplings being measured. The couplings λ and Δg_1^Z are expected to be measured to a higher precision than $\Delta\kappa_\gamma$. Comparing the results for the larger statistics samples at 196 and 200 GeV to the others demonstrates the significant improvement of the measurements when larger statistics are available. Less obvious is the fact that the precision of the measurements per selected event increases with increasing centre-of-mass energy.

Beyond estimating the expected fit errors, this test also provides a check on the precision of the one sigma uncertainty estimate from the chi-squared curve. The main

	Expected fit error					
	$\Delta\kappa_\gamma$		λ		Δg_1^Z	
E_{CM}	mean	RMS	mean	RMS	mean	RMS
One parameter fits						
192	0.91	0.33	0.37	0.12	0.46	0.20
196	0.54	0.22	0.22	0.05	0.27	0.11
200	0.52	0.21	0.20	0.05	0.27	0.12
202	0.60	0.25	0.26	0.07	0.31	0.10
Three parameter fits						
192	1.23	0.58	0.41	0.28	0.63	0.45
196	0.72	0.25	0.24	0.09	0.36	0.13
200	0.70	0.24	0.22	0.05	0.35	0.10
202	0.76	0.27	0.28	0.07	0.40	0.16

Table 5.1: The expected one sigma uncertainty and root mean square (RMS) for the one and three parameter fits to real data for each centre-of-mass energy. The results are derived from 10 000 separate data sized test subsamples generated with Standard Model couplings.

criterion used to test this is the number of subsample fits which had a difference between the chi-squared value at its minimum and at the generated value within a certain critical range. For each fit performed on a test subsample, the chi-squared value at the minimum for that fit is obtained in the usual way. In addition to this, the chi-squared value for that fit at the coupling value used to generate those events is calculated. If the difference in these values, $\Delta\chi^2_{\mathrm{meas}}$, is less than a critical number, $\Delta\chi^2_{\mathrm{crit}}$, then the fit fulfilled this requirement. By comparing the number of subsample fits which have $\Delta\chi^2_{\mathrm{meas}} < \Delta\chi^2_{\mathrm{crit}}$ with the statistical expectation, the quality of the chi-squared curve determination can be found.

For a one parameter fit the $\Delta\chi^2_{\mathrm{crit}}$ value is set equal to one, which is actually the definition of the one sigma uncertainty on the measurement. The number of events satisfying $\Delta\chi^2_{\mathrm{meas}} < \Delta\chi^2_{\mathrm{crit}}$ is therefore the number of events where the true coupling is within one standard deviation of the measured coupling. If the distribution of these independent subsample fits is Gaussian in behaviour, then 68.27% of these fits, that is about 6 827 of the 10 000 individual tests should, satisfy $\Delta\chi^2_{\mathrm{meas}} < \Delta\chi^2_{\mathrm{crit}}$. Incidentally, since the outcome of a fit either does or does not satisfy the requirement, the probability of obtaining any particular number of successes is described by a binomial distribution. Using this, the one standard deviation on the expected number of successes can be calculated yielding an expected number of subsample fits of $6\,827 \pm 47$. For a three parameter fit the value $\Delta\chi^2_{\mathrm{crit}} = 3.527$ is used as this also corresponds to a 68.3% probability content for a measurement with Gaussian behaviour. Any disagreement with expectation may point to the need for a rescaling of the errors on the fit results which can be achieved by applying a multiplication factor to the chi-squared curve. For example, for a set of fits in which the number of tests satisfying $\Delta\chi^2_{\mathrm{meas}} < \Delta\chi^2_{\mathrm{crit}}$ is significantly above the expected value it could be concluded that the one sigma error on the fit results is too large. This would imply the need for the uncertainty on the fits to be scaled to a smaller value. This scale factor can be calculated from the $\Delta\chi^2_{\mathrm{meas}}$ value of the 6 827 th subsample test ordered by increasing values of $\Delta\chi^2_{\mathrm{meas}}$.

Before presenting the results, it is important to realise that this test assumes that the distribution of the central values of the 10 000 trial fits is Gaussian in behaviour, which is only an approximation. In fact the chi-squared curves can display double minima behaviour where the fit converges to one of two possible coupling values. These values may be similar to each other or the minima may be similar in depth, or have a difference in depth of just above $\Delta\chi^2_{\mathrm{crit}}$, this can distort the one sigma error estimates which are derived from the curves. The number of one parameter and three parameter fits which satisfy the $\Delta\chi^2_{\mathrm{meas}} < \Delta\chi^2_{\mathrm{crit}}$ criterion is given in table 5.2. It can be seen that most of the tests demonstrate good agreement with expectation which implies that there are no major problems with the one sigma uncertainty evaluation in these low statistics fits. In particular, the fit tests performed at 196 GeV show very good agreement, and those at 200 GeV tend to be slightly low which indicates that the error is under-estimated. The correction factor which would bring the number of fits to the 68.27% level at these two centre-of-mass energies are all within 5% of unity with the largest correction needed for the measurement of Δg_1^Z at 200 GeV. For the one parameter fits at 192 and 202 GeV, the results for the measurement of λ are as expected, but the one sigma errors for Δg_1^Z and $\Delta\kappa_\gamma$ are all over-estimated. This over-estimation simply implies that the fit results do not constrain the coupling values as strongly as they should. However, the distributions of the central values and one sigma errors for these 10 000 fits provide the reasons for these inconsistencies since there is evidence for a proportion of the chi-squared curves having double minima behaviour. In cases where the local maximum between the deepest and the second deepest minimum on the chi-squared curve is less than $\Delta\chi^2_{\text{crit}}$ above the deeper minimum, the one sigma error tends to be larger than expected. Conversely, where the local maximum is greater than $\Delta\chi^2_{\text{crit}}$, the one sigma error tends to be smaller than expected. The distribution of the fit errors show a two peak structure which supports the existence of these two possible outcomes. The scenario in which the error tends to be larger is more prevalent which explains the excess in the number of fits satisfying $\Delta\chi^2_{\text{meas}} < \Delta\chi^2_{\text{crit}}$.

More than two thirds of the real data collected during 1999 was recorded at 196 and 200 GeV, and the tests on these fits present little problem, therefore based on the numbers in table 5.2 no error scaling is applied. The fits at 192 and 202 GeV do not show problems in the error determination itself, only the influence from double minima behaviour, therefore error scaling is not applied here either. Furthermore, following similar arguments as for the one parameter fits, no error scaling is applied for the fits to three couplings.

5.2.2 High Statistics Bias Tests

In order to check that the fit procedure is unbiased, a series of fits are performed where the TGC parameter values are extracted from test samples with large statistics. The Standard Model Monte Carlo samples are the same as those used in the low statistics tests. Samples generated with anomalous couplings[a] are also used and the results

[a] Anomalous coupling samples at 196 and 200 GeV are generated with $\alpha = \pm 0.5, \pm 1.0$, whereas those at 192 and 202 GeV are generated only with $\alpha = \pm 1.0$.

E_{CM}	Number of samples satisfying $\Delta\chi^2_{\mathrm{meas}} < \Delta\chi^2_{\mathrm{crit}}$			
	one parameter fit			three parameter fit
	$\Delta\kappa_\gamma$	λ	Δg_1^Z	
192	8 391	6 935	7 598	7 589
196	6 773	6 644	6 836	6 748
200	6 603	6 581	6 450	6 525
202	7 763	6 912	7 240	7 340

Table 5.2: Results of low statistics tests for the one parameter and three parameter fits performed on various test samples. The values indicate the number of the 10 000 subsample fits which satisfy the requirement $\Delta\chi^2_{\mathrm{meas}} < \Delta\chi^2_{\mathrm{crit}}$. For a Gaussian distribution of fit results the numbers are expected to be close to $6\,827 \pm 47$. The test samples are generated with Standard Model couplings at each centre-of-mass energy separately.

are shown in figures 5.3 and 5.4. They show the one parameter fit results and one sigma uncertainties using the $E[\mathcal{O}_i^{(1)}]$ and $E[\mathcal{O}_{ii}^{(2)}]$ values corresponding to the α_i being extracted. The parameter value extracted from a fit, α_{fit}, is compared to the parameter value, α_{gen}, used to generated the events in that test sample. The range covered by the $\alpha_{\mathrm{fit}} - \alpha_{\mathrm{gen}}$ axis is equal to the expected error on the OPAL data which was presented in table 5.1. If the fit procedure is unbiased then good agreement within the precision of the measurement is expected between α_{fit} and α_{gen}.

It can immediately be seen that the TGC parameter values in the test samples returned by the fit generally reproduce the values used to generate them. The difference between the generated value and the central value is always within the expected one sigma uncertainty for the OPAL data. The agreement is also usually good taking into account the one sigma uncertainty on the high statistics fit results. In all cases, the fit returns results for the Standard Model test samples which are within two sigma of the Standard Model. In section 5.1.1 it was stated that the optimal observables employed in this fit are maximally sensitive for couplings near to these values. Although the use of the second order observables attempts to supplement the sensitivity to a larger range of couplings, the fit is still expected to behave less well at values significantly away from the Standard Model. The fit results are worth discussing further:

- At all energies, α_{gen} is within two sigma of the α_{fit} result for $\Delta\kappa_\gamma$ for all points apart from two. The first point, where $\Delta\kappa_\gamma$ is extracted from a sample with $\Delta\kappa_\gamma = -1$ at 202 GeV, α_{fit} is about 3.9 standard deviations below the expected value. This is acceptable from a statistical viewpoint and especially considering the lower sensitivity of the fit at this value of the coupling. Secondly, also at 202 GeV, the fitted value for the test sample generated with $\Delta\kappa_\gamma = +1$ is $\Delta\kappa_\gamma = -0.21^{+0.08}_{-0.07}$. The reason for this is that the chi-squared curve for this fit possesses a double minimum structure which means that two different values of $\Delta\kappa_\gamma$ are found to best describe the coupling value in the sample. The MINUIT program which performs the minimisation finds the deepest of the two minima. The second minimum, which is higher than the first by $\Delta\chi^2 = 1.3$, has a value $\Delta\kappa_\gamma = 1.01^{+0.08}_{-0.09}$, which is consistent with α_{gen}. The range of couplings which are within one sigma of the two minima central values are shown in figure 5.4 as the two disconnected lines, the one with the dot corresponds to the central value with the lowest chi-squared value. This degeneracy can be lifted by using results from other decay channels.

- All of the α_{fit} results for λ are consistent with the α_{gen} values to within three standard deviations apart from the fit results at 200 GeV. At this energy the fit tends to underestimate the magnitude of the deviation from the Standard Model value by about 10% at $\lambda = \pm 1.0$. The fit results for the Standard Model and ± 0.5 test samples could be argued to be consistent with α_{gen} especially since the fit is expected to be maximally sensitive at these values. However, the fit procedure for large values of $|\lambda|$ does not perform so well. The results are similar to those from bias tests performed on data generated at a centre-of-mass energy of 189 GeV [134], although the effect is not so evident at other centre-of-mass energies.

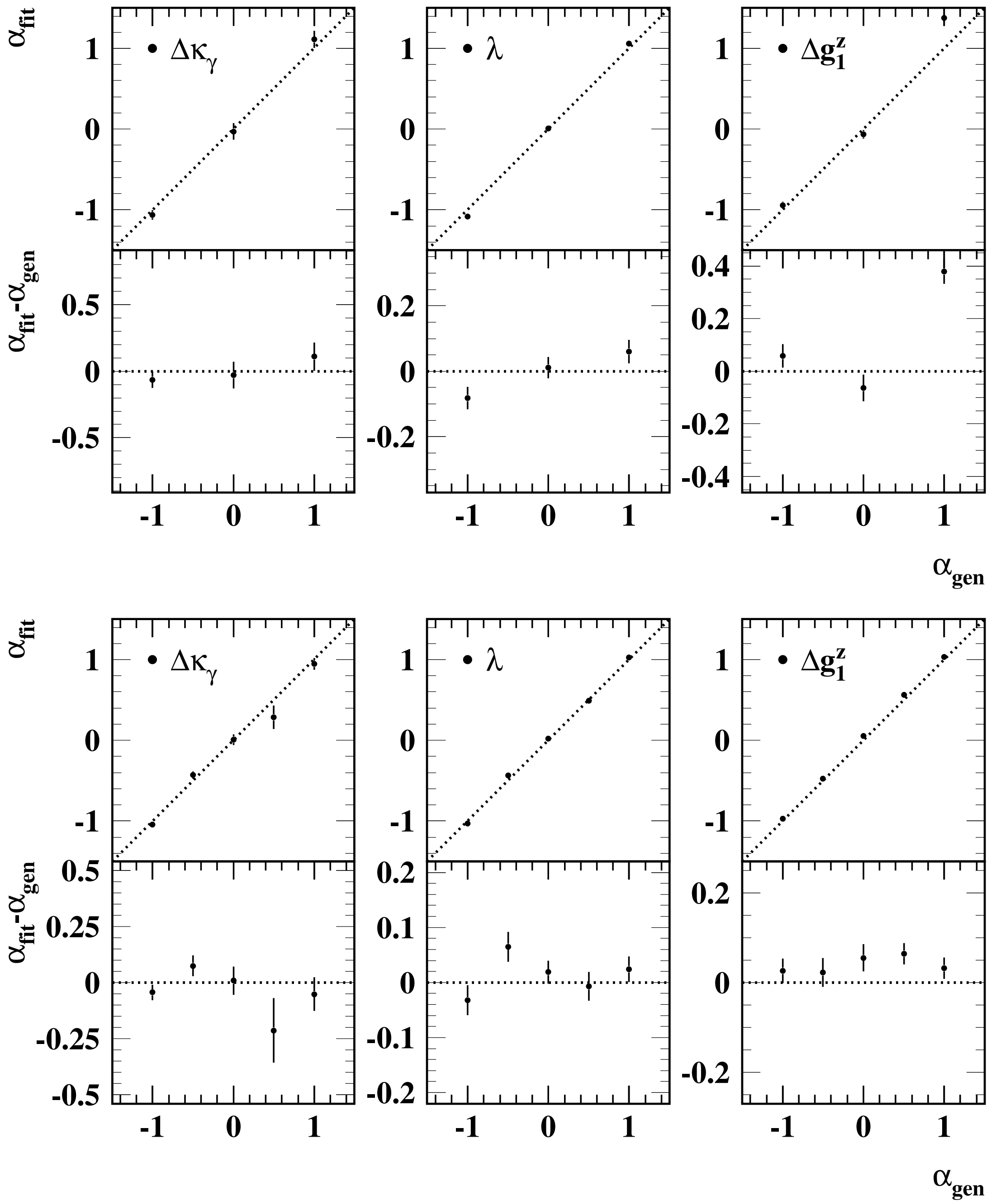

Figure 5.3: Results of high statistics bias tests for fits at 192 GeV (upper) and 196 GeV (lower). The points and error bars represent the central values and one sigma uncertainties for the one parameter fits for $\Delta\kappa_\gamma$, λ and Δg_1^Z using the appropriate $E[\mathcal{O}_i^{(1)}]$ and $E[\mathcal{O}_{ii}^{(2)}]$. The extracted values, $\alpha_{\rm fit}$, are plotted against those used to generate the events in the test sample, $\alpha_{\rm gen}$. The range on the $\alpha_{\rm fit} - \alpha_{\rm gen}$ axis is equal to the expected error on the OPAL data. The dotted lines are intended to indicate where the points should lie if the fit results are unbiased.

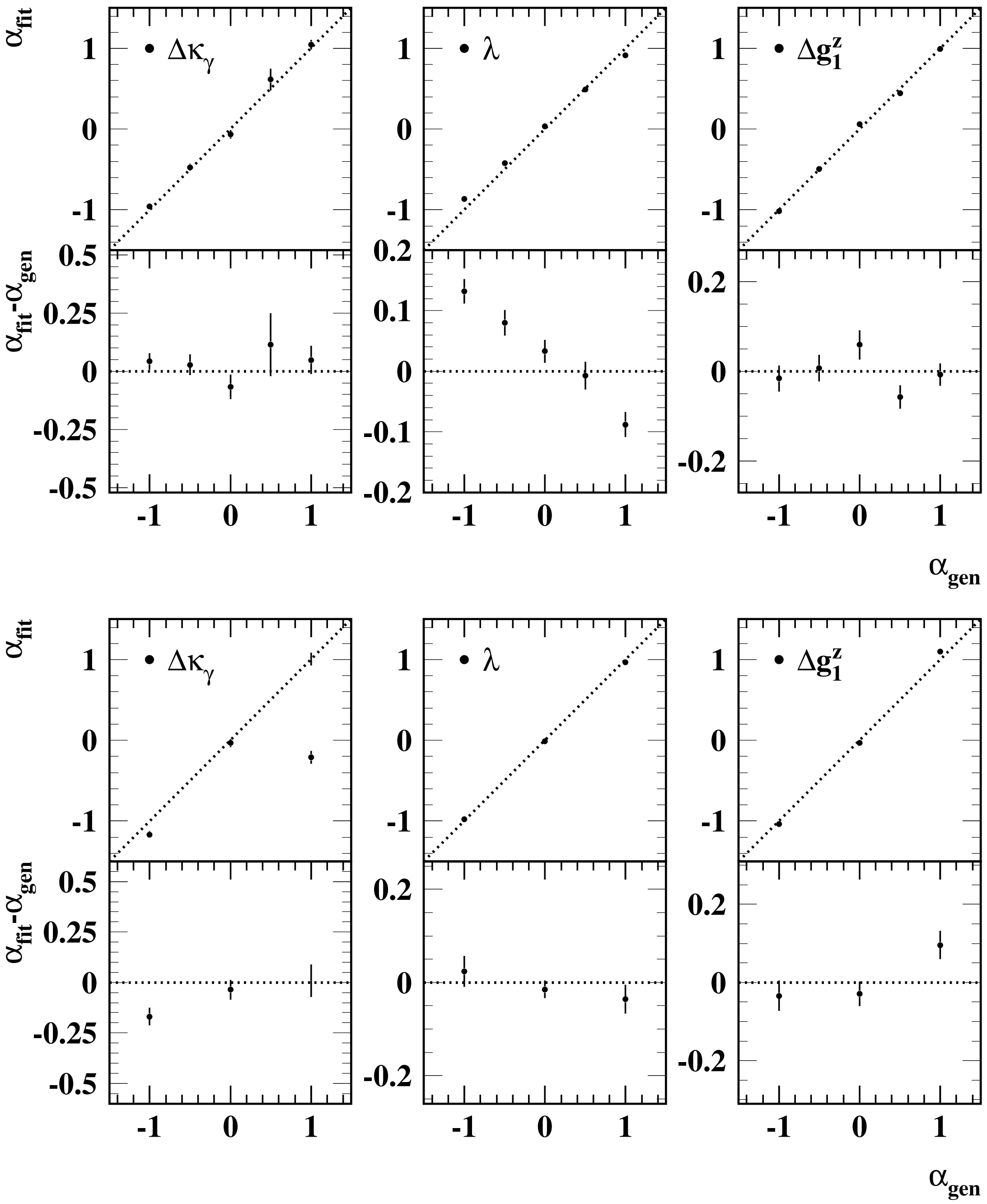

Figure 5.4: Results of high statistics bias tests for fits at 200 GeV (upper) and 202 GeV (lower). The points and error bars represent the central values and one sigma uncertainties for the one parameter fits for $\Delta\kappa_\gamma$, λ and Δg_1^Z using the appropriate $E[\mathcal{O}_i^{(1)}]$ and $E[\mathcal{O}_{ii}^{(2)}]$. The extracted values, $\alpha_{\rm fit}$, are plotted against those used to generate the events in the test sample, $\alpha_{\rm gen}$. The range on the $\alpha_{\rm fit} - \alpha_{\rm gen}$ axis is equal to the expected error on the OPAL data. The dotted lines are intended to indicate where the points should lie if the fit results are unbiased.

- The $\alpha_{\rm gen}$ value is within three standard deviation of the $\alpha_{\rm fit}$ results for Δg_1^Z for all points apart from one. This point is the fit performed on events generated with $\Delta g_1^Z = +1$ at 192 GeV, here $\alpha_{\rm gen}$ is more than nine sigma away from the fitted value. The shape of the chi-squared curve for this fit is non-Gaussian with a second minimum at about $\Delta g_1^Z = -1.8$, although with a much larger chi-squared value of about 300, nevertheless, the result still agrees with the generated value within the uncertainty expected in real OPAL data.

These high statistics bias tests demonstrate some of the problems which could arise when interpreting the results from fits to the OPAL data. It is therefore important to measure these biases. The results demonstrate that the fit is reliable in accurately predicting the couplings for events generated with values around the Standard Model. It also demonstrates that within the uncertainty on the fit result, the fit can successfully extract the correct coupling values from the OPAL data.

Similar results for the three parameter fits are shown in table 5.3. In these fits all nine of the mean optimal observables are used. The test samples were generated using Standard Model and anomalous coupling values, and the reference samples were the same as those used in the one parameter fits. The one sigma uncertainties expected in OPAL data for these fits were given in table 5.1. All of the results for the test samples generated with Standard Model couplings are consistent with $\alpha_{\rm gen}$ to within two standard deviations. For the fits to samples generated with anomalous couplings, where the fit is expected to be less sensitive, all of the results are well within the expected one sigma uncertainty for the OPAL data. Most of the results are consistent to within three sigma and normally to within two and one sigma except for the measurement of $\Delta g_1^Z = -0.5$ at 196 GeV and $\lambda = -0.5$ at 200 GeV.

MC test sample	Fitted couplings, α_{fit}		
E_{CM}, coupling	$\Delta\kappa_\gamma$	λ	Δg_1^Z
192, SM	-0.030 ± 0.140	$+0.055 \pm 0.037$	-0.108 ± 0.068
196, SM	$+0.010 \pm 0.054$	-0.007 ± 0.025	$+0.058 \pm 0.036$
200, SM	-0.056 ± 0.050	$+0.023 \pm 0.021$	$+0.035 \pm 0.035$
202, SM	-0.042 ± 0.053	-0.009 ± 0.022	-0.020 ± 0.035
196, $\alpha = +0.5$	$+0.301 \pm 0.174$	$+0.475 \pm 0.026$	$+0.579 \pm 0.047$
196, $\alpha = -0.5$	-0.459 ± 0.060	-0.435 ± 0.033	-0.264 ± 0.048
200, $\alpha = +0.5$	$+0.222 \pm 0.104$	$+0.490 \pm 0.024$	$+0.522 \pm 0.054$
200, $\alpha = -0.5$	-0.372 ± 0.057	-0.392 ± 0.025	-0.523 ± 0.036

Table 5.3: Results of high statistics three parameter fits to various test samples using all nine mean optimal observables. The numbers indicate the central value and one sigma uncertainty on the fit. The test samples are generated with Standard Model (SM) couplings or with one anomalous coupling, α, at the indicated value. Fits are performed for each centre-of-mass energy separately.

5.3 Determination of Systematic Effects

There are many possible sources of systematic error which might affect the measurement of the couplings. Those considered most important were investigated and the magnitude of their effect was evaluated. The systematic error becomes important if its size approaches the size of the statistical error on the measurement. This is never the case in this analysis.

The size of the systematic effect is evaluated from the difference in the central values of the couplings which are obtained from the chi-squared curves for both the situations in which the systematic effect is included and not included in the fit. If the shift is actually smaller than the statistical precision on the results then the uncertainty on the difference between the two results is taken as the systematic error. The value quoted also depends upon the nature of the check being performed. For example, when investigating the effect of the Monte Carlo generator being used, the difference between the generated coupling value and the value returned by the fit is more important.

To incorporate the systematic effects into the final fit to the real OPAL data, the systematic shifts are taken on the observable values themselves. A nine-by-nine systematic error matrix is constructed for each effect and these are summed together to give the full systematic error covariance matrix which is added to the expected statistical covariance matrix, V_{ij}, in equation 5.6 before inversion [138]. This does not alter the overall procedure for performing the fit and it was found that in this analysis, the inclusion of the systematic effects has virtually no impact on the coupling results and errors.

Several separate samples of events were generated in order to investigate these systematic effects, these are listed in appendix A. The overall systematic effects observed for the entire 1999 data sample together are quoted in table 5.4. These are obtained from the four chi-squared curves by simply adding them together to produce an overall chi-squared curve from which the fit results are extracted. The systematic errors are not expected to vary significantly with centre-of-mass energy, and combining the results helps to reduce their statistical error.

The following sources of systematic uncertainty were considered:

- The uncertainty associated with the **Monte Carlo generator** used in the analysis was investigated. Large samples of four-fermion events generated with KORALW [51, 52] were treated as the test samples. These events differ from the EXCALIBUR events in their matrix element calculation and the treatment of initial state radiation. The events were generated with Standard Model couplings and the systematic error is taken as the shift in the measured couplings from their expected values, or the statistical uncertainty if greater.
- The uncertainty due to the Monte Carlo modelling of the **efficiency dependence** on the event shape is checked by comparing the real data and generated distributions of kinematic variables. This specifically checks the dependence of

the selection on the kinematics of the event. The kinematic variables which were investigated were the reconstructed lepton energies and their polar angles. Good agreement was found in the distributions of these quantities between the real OPAL data and simulated events. However, in order to quantify this uncertainty, the ratio of these distributions were parameterised as straight lines, and these were used to correct the distributions in the test sample being used in the fit. This parameterisation was difficult to obtain because of the low statistics of the fully leptonic channel, therefore, the parameterisations for the same kinematic distributions for the lepton in the higher statistics semi-leptonic channel were used. The fit was performed on W-pair events generated with KORALW with and without this efficiency correction applied.

- The **background contamination** in the event selection, which was discussed in section 4.3.2, was found to be very small, therefore its whole effect is included in the analysis as a systematic error. The size of the effect is found by including in the fit those events which simulate background processes and which were accepted by the selection. The fit was performed on a test sample of W-pair events generated with KORALW in both the cases where these background events were included and not included. The mean optimal observable values are calculated for these background events, and the corresponding values in the test samples were shifted to mimic the presence of these events. The background events included were those which were accepted by the final selection, the event rates expected are listed with their statistical error in the $\mathrm{Sel}^{\mathrm{fin}}$ columns of table 4.4.

- The uncertainty due to the **lepton reconstruction** was investigated by considering the effects of smearing and shifting the kinematics of the lepton in the generated events. The lepton energies were shifted by +0.3%, and the resolution of the lepton energy, azimuthal and polar angles were smeared by 3%, 5% and 10% respectively. The size of these variations are determined from extensive studies of Z decays. The fit was performed on a test sample of W-pair events generated with KORALW in both the cases where the lepton kinematic quantities were and were not adjusted.

Source	Systematic error		
	$\Delta\kappa_\gamma$	λ	Δg_1^Z
Monte Carlo generator	± 0.07	± 0.01	± 0.02
Efficiency	± 0.07	± 0.02	± 0.03
Background	± 0.05	± 0.02	± 0.02
Reconstruction	± 0.005	± 0.001	± 0.002
E_{beam} and M_{W}	± 0.004	± 0.003	± 0.002
Total	± 0.11	± 0.04	± 0.03

Table 5.4: The overall systematic uncertainties arising from different sources in the determination of the triple gauge boson couplings using a one parameter fit.

- The effects of the uncertainties on the measurements of the **LEP beam energy** and the **W mass** were investigated as these both affect the fit results. The current error on the measurement of the LEP beam energy is around $\pm 20\,\text{MeV}$ [139]. Also, some of the Monte Carlo samples being employed were generated at a different energy to that at which the data was taken. To investigate this, samples of W-pair events generated with KORALW at different centre-of-mass energies, typically $\pm 3\,\text{GeV}$, were treated as test samples. The shifts in these fit results were scaled down to the size of the expected uncertainty in the energy measurement, and this is taken as the systematic uncertainty. A similar procedure is used to assess the uncertainty due to the measurement of the W mass which, according to independent measurements from hadron collisions, has a current error of around $90\,\text{MeV}/c^2$ [140, 141]. Samples of events are generated with W masses at $80.33\,\text{GeV}/c^2$ and at ± 0.5 and $\pm 1.0\,\text{GeV}/c^2$ about this value. Again, the observed shifts are scaled down to the size of the expected uncertainty and this is taken as the systematic error.

It can be seen that the expected systematic uncertainties are very small compared to the expected precision on the measurement of the coupling values shown in table 5.1.

5.4 Results and Conclusions

5.4.1 WW $\to \ell\nu\ell\nu$ fits

The same fit procedure employed in the fit tests and systematic checks is used to extract the TGC parameter values from the real OPAL data presented in table 4.5. The reference samples are as usual all of the available four-fermion EXCALIBUR samples. The systematic error matrix is included in the fit, but as previously stated, this actually has very little impact on the fit results. Results are presented for the one parameter and multi-parameter fits for each centre-of-mass energy separately and for the total 1999 data. The overall fit results are obtained by summing together the chi-squared curves obtained from the fits to the four energies separately and recalculating the minima and one sigma uncertainty values.

The one parameter fit results, where only one of the couplings is allowed to vary from its Standard Model value, are given in table 5.5. In these fits the only mean observables used are the first and second order diagonal ones corresponding to the parameter being fitted. The individual and summed chi-squared curves obtained from the fits to each of the couplings are presented in figure 5.5. The one sigma uncertainties

	One parameter fit result		
E_{CM}	$\Delta\kappa_\gamma$	λ	Δg_1^Z
192	$+0.15^{+1.02}_{-0.75}$	$-0.43^{+0.43}_{-0.35}$	$-0.36^{+0.49}_{-0.41}$
196	$-0.52^{+0.42}_{-0.32}$	$-0.43^{+0.21}_{-0.19}$	$-0.44^{+0.28}_{-0.23}$
200	$+0.52^{+0.42}_{-0.46}$	$+0.01^{+0.18}_{-0.17}$	$+0.10^{+0.21}_{-0.23}$
202	$+0.21^{+0.68}_{-0.53}$	$+0.08^{+0.31}_{-0.30}$	$-0.18^{+0.33}_{-0.30}$
overall	$+0.18^{+0.46}_{-0.32}$	$-0.13^{+0.13}_{-0.12}$	$-0.15^{+0.17}_{-0.16}$

Table 5.5: Results of one parameter fits to extract the TGC parameter values $\Delta\kappa_\gamma$, λ and Δg_1^Z from 1999 data. The results for each centre-of-mass energy are shown separately together with the overall result. The errors represent one sigma uncertainties including systematic effects.

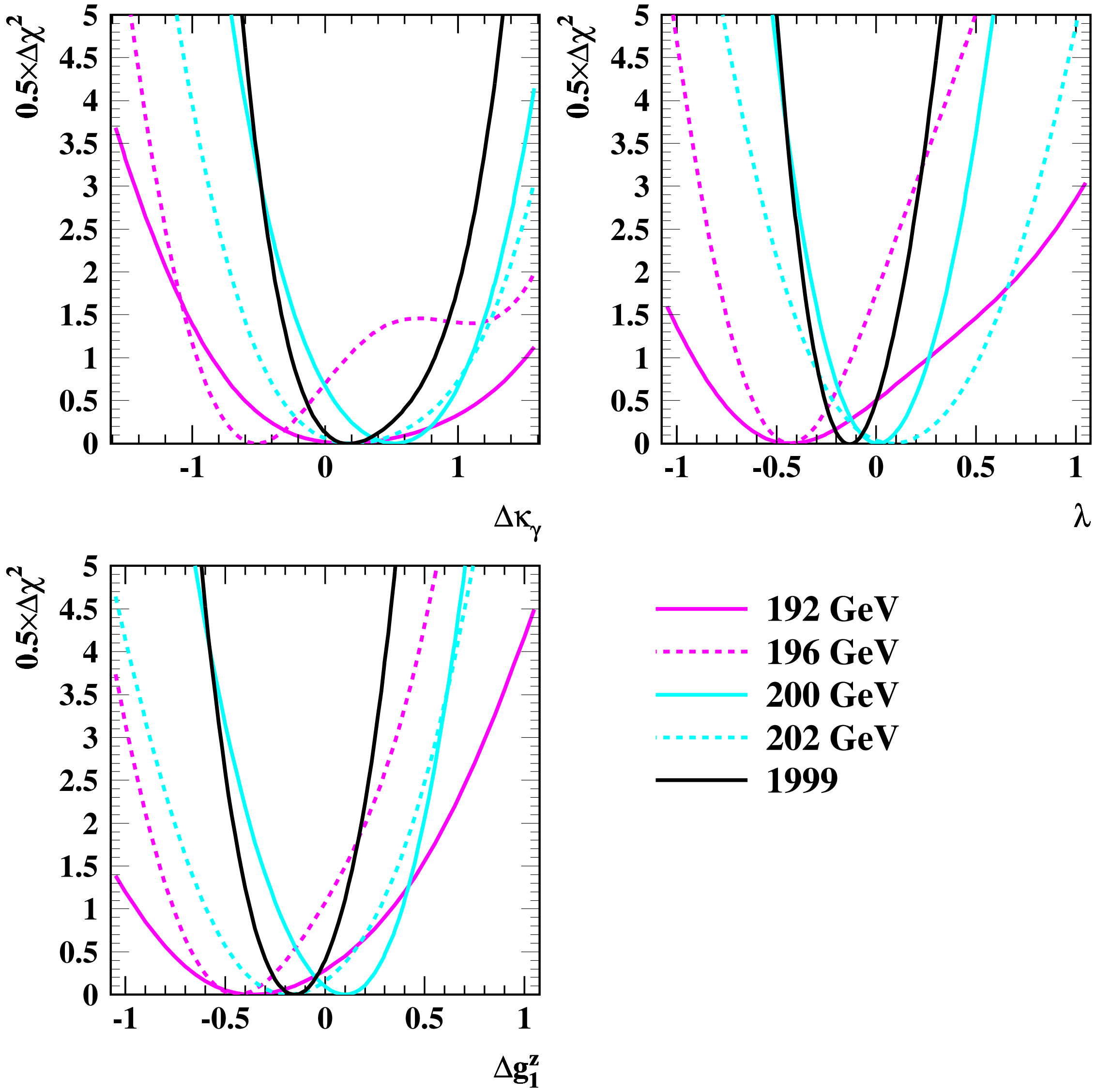

Figure 5.5: The $0.5 \times \Delta\chi^2$ curves for the one parameter fits performed on real OPAL data recorded during 1999. The curves are shifted so that their minimum values are at zero, and the factor of 0.5 converts the $\Delta\chi^2$ values into $-\Delta \log \mathrm{L}$ values. The curves for the four centre-of-mass energies are shown separately together with the total for the 1999 OPAL data. The fits include systematic effects.

for each coupling at each centre-of-mass energy agree well with the expected error determined from the low statistics fit tests shown in table 5.1. The results for κ_γ ($\equiv \Delta\kappa_\gamma + 1$) and g_1^Z ($\equiv \Delta g_1^Z + 1$) exclude coupling values of zero by more than three and five sigma respectively. Furthermore, all of these results are in agreement with the Standard Model expectations for the coupling values. One result, the measurement of λ at 196 GeV, lies just over two sigma away from the Standard Model expectation, whereas all of the other results are within two sigma, and more often to within one sigma, of the Standard Model value.

The results for the more model independent multi-parameter fits are shown in table 5.6. In the two parameter fits each of the three couplings in turn is fixed to its Standard Model value while the other two are allowed to vary. In the three parameter fits all three couplings are allowed to vary simultaneously. In these fits the mean values of all nine optimal observables are included. The one sigma uncertainties on these results agree well with the expected errors determined from the low statistics fit tests which were shown in table 5.1. The two dimensional projections of the chi-squared contours for these fits are presented in figure 5.6. The one, two, three and four sigma contours in the planes defined by the three pairs of couplings are shown for both the two and three parameter fits. The contours corresponding to the two parameter case are from fits where the third parameter was set to its Standard Model value, whereas those for the three parameter fits has the third parameter set to its best value in that fit. As with the one parameter fits, these results exclude coupling values of zero and they are all in agreement with the Standard Model expectation to within at least three sigma, and more usually within two and one sigma. The contours in figure 5.6 demonstrate how the fit convergence of the three pairs of couplings depend upon whether the third parameter is fixed or allowed to vary.

The WW $\rightarrow \ell\nu\ell\nu$ data recorded by OPAL during 1999 alone confirm the presence of triple gauge couplings. The results are also in agreement with the Standard Model predictions for the coupling values and therefore there is no evidence for any behaviour beyond Standard Model expectations.

E_{CM}	Multi-parameter fit results $\Delta\kappa_\gamma$	λ	Δg_1^Z
Two parameter fits			
192	$+0.14^{+0.94}_{-0.81}$	$-0.35^{+0.49}_{-0.35}$	0.0
	$-0.11^{+0.90}_{-0.89}$	0.0	$-0.33^{+0.50}_{-0.44}$
	0.0	$-0.30^{+0.47}_{-0.37}$	$-0.22^{+0.47}_{-0.44}$
196	$-0.56^{+0.55}_{-0.38}$	$-0.36^{+0.24}_{-0.21}$	0.0
	$-0.07^{+0.53}_{-1.44}$	0.0	$-0.62^{+0.26}_{-0.23}$
	0.0	$-0.08^{+0.27}_{-0.25}$	$-0.57^{+0.26}_{-0.23}$
200	$+0.51^{+0.42}_{-0.46}$	$-0.01^{+0.19}_{-0.17}$	0.0
	$+0.92^{+0.50}_{-0.48}$	0.0	$+0.40^{+0.28}_{-0.26}$
	0.0	$-0.39^{+0.18}_{-0.17}$	$+0.08^{+0.20}_{-0.22}$
202	$+0.23^{+0.70}_{-0.54}$	$+0.14^{+0.31}_{-0.31}$	0.0
	$+0.08^{+0.63}_{-0.54}$	0.0	$-0.13^{+0.32}_{-0.29}$
	0.0	$+0.15^{+0.27}_{-0.27}$	$-0.18^{+0.32}_{-0.29}$
overall	$+0.43^{+0.36}_{-0.35}$	$-0.07^{+0.15}_{-0.14}$	0.0
	$+0.35^{+0.42}_{-0.38}$	0.0	$+0.02^{+0.20}_{-0.18}$
	0.0	$-0.09^{+0.13}_{-0.12}$	$-0.03^{+0.17}_{-0.16}$
Three parameter fits			
192	$-0.07^{+1.00}_{-0.99}$	$-0.30^{+0.48}_{-0.38}$	$-0.23^{+0.50}_{-0.47}$
196	$-0.85^{+1.66}_{-0.51}$	$-0.23^{+0.31}_{-0.25}$	$-0.25^{+0.29}_{-0.47}$
200	$+0.93^{+0.57}_{-0.52}$	$-0.08^{+0.22}_{-0.19}$	$+0.41^{+0.32}_{-0.29}$
202	$+0.08^{+0.71}_{-0.60}$	$+0.15^{+0.27}_{-0.28}$	$-0.17^{+0.37}_{-0.31}$
overall	$+0.39^{+0.39}_{-0.37}$	$-0.08^{+0.14}_{-0.13}$	$-0.13^{+0.18}_{-0.16}$

Table 5.6: Results of two and three parameter fits to extract the TGC parameter values $\Delta\kappa_\gamma$, λ and Δg_1^Z from 1999 data. The results for each centre-of-mass energy are shown separately together with the overall result. The errors represent one sigma uncertainties including systematic effects.

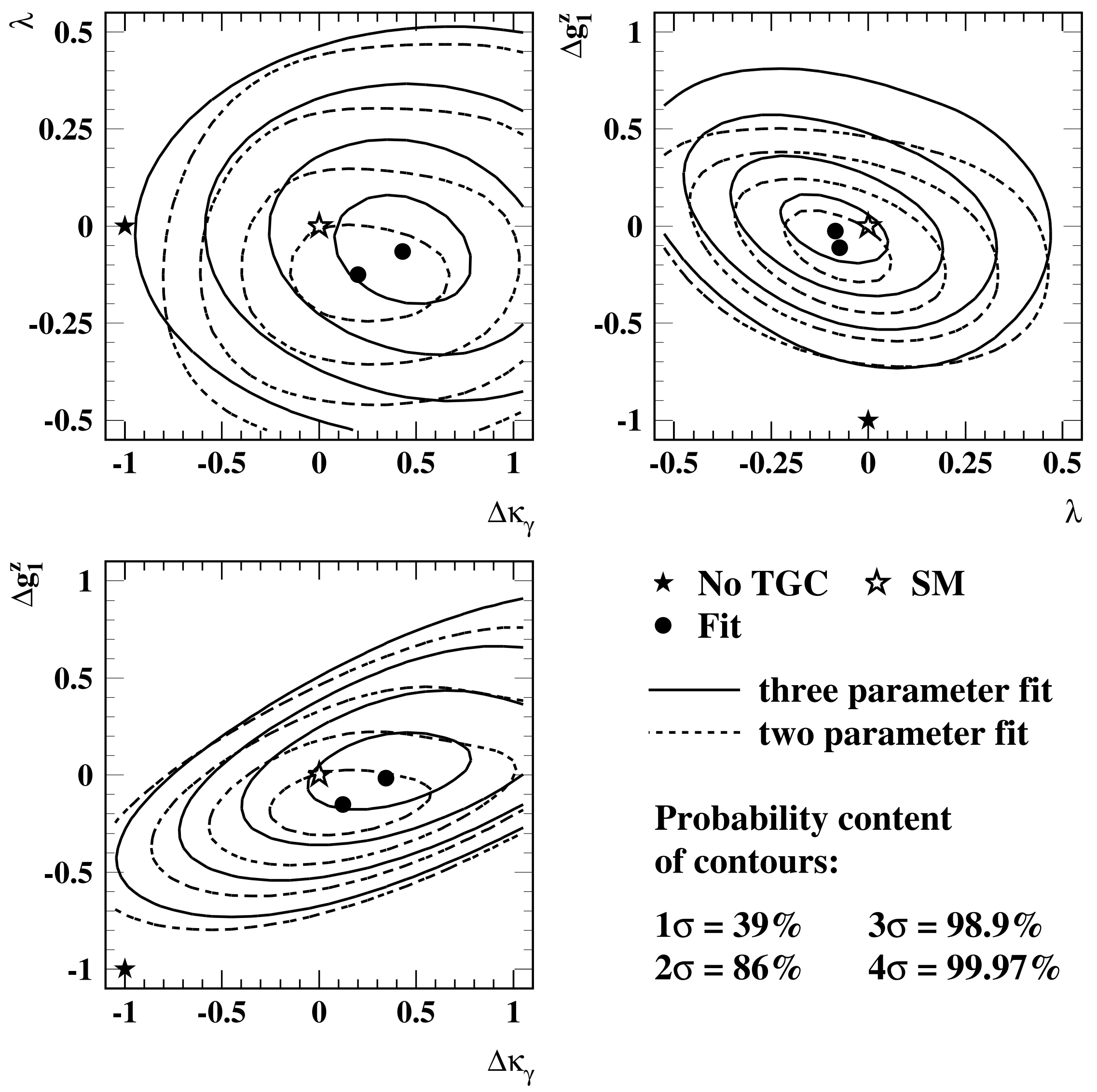

Figure 5.6: The two dimensional chi-squared contours for the two and three parameter fits performed on real OPAL data recorded during 1999. The central values for the fits, the Standard Model couplings (SM) and the couplings in the absence of triple gauge boson vertices (No TGC) are indicated. The solid contours represent the case in which the third parameter is set to the value to which it converged in the three parameter fit. The dashed contours are where the third parameter is set to its Standard Model value. These fits include systematic effects.

5.4.2 Combination

The results for the measurement of $\Delta\kappa_\gamma$, λ and Δg_1^Z using the angular distributions in $WW \to \ell\nu\ell\nu$ events recorded by OPAL during 1999 are combined with those measured using the hadronic and semi-leptonic W-pair events as well as those obtained from the event rate analysis for the same year [95]. In addition, these results are combined with those obtained using data recorded at lower centre-of-mass energies [90–92, 94]. The combination is achieved by adding together the chi-squared curves from each of the fits, including systematic effects, and the minima and one sigma uncertainties are re-evaluated from them. The results are further combined with those obtained from the analysis of single-W events recorded by OPAL at 189 GeV [93]. The coupling values together with their one sigma uncertainties from all of these results combined together are

$$\begin{aligned} \kappa_\gamma &= 0.91^{+0.11}_{-0.10}, \\ \lambda &= -0.103^{+0.040}_{-0.039}, \\ g_1^Z &= 0.954^{+0.042}_{-0.041}. \end{aligned}$$

Each parameter is determined with the other two parameters set to their Standard Model values and they include systematic effects [95]. These results are all reasonably consistent with the Standard Model expectation, although the value of λ is interesting.

These results are combined with the measurements performed by the ALEPH, DELPHI and L3 collaborations to give one parameter fit results of

$$\begin{aligned} \kappa_\gamma &= 0.998^{+0.067}_{-0.065}, \\ \lambda &= -0.036^{+0.028}_{-0.027}, \\ g_1^Z &= 0.975^{+0.026}_{-0.026}, \end{aligned}$$

where the one sigma uncertainty is shown, including systematic effects [142]. These results are consistent with the Standard Model expectation at the 95% confidence level. The low value of λ extracted by OPAL is not confirmed with any statistical significance by the other experiments.

Appendix A

Monte Carlo Samples

This appendix lists the Monte Carlo samples employed in the TGC analysis presented in this thesis. They are listed in tables A.1-A.4 which are divided up according to the purpose for which they were used. The first part of the tables lists the sample used to determining the selection efficiency, the second list samples used to extract the TGC parameter values, the third list samples used to estimate background rates, and the last list samples used in evaluating systematic effects. The samples are described by:

- the *run number*, which is used within OPAL to uniquely identify the sample,
- the *channel*, or the physical process which is being modelled in the sample. For samples generated with anomalous couplings, the parameter values are given ($\Delta\kappa_\gamma$,λ,Δg_1^Z),
- the *generator*, which is the name of the software used to generate the events in the sample,
- the *number of events*, N_{ev}, in the sample,
- the *integrated luminosity*, $\int \mathcal{L}\,\mathrm{d}t$, of the sample,
- the *cross-section*, σ, of the process being simulated in the sample, the cross-section is obtained according to the generator used to produce the sample.

run	channel	generator	N_{ev}	$\int\mathcal{L}\,\mathrm{d}t$ [fb^{-1}]	σ [pb]
8700	WW $\rightarrow$ all	KORALW	100 000	5.9	16.9
9484	4f (0,0,0)	EXCALIBUR	93 000	5.0	18.4
10012	4f (+1,0,0)	EXCALIBUR	50 000	2.5	19.9
10013	4f (-1,0,0)	EXCALIBUR	50 000	2.4	20.6
10014	4f (0,+1,0)	EXCALIBUR	50 000	2.1	24.3
10015	4f (0,-1,0)	EXCALIBUR	50 000	2.0	25.5
10016	4f (0,0,+1)	EXCALIBUR	50 000	2.0	25.5
10017	4f (0,0,-1)	EXCALIBUR	50 000	1.9	26.3
1352	ee	BHWIDE	100 000	0.2	577
1624	$\mu\mu$	KORALZ	50 000	6.5	7.7
1626	$\mu\mu$	KK2F	50 000	6.0	8.3
1551	$\tau\tau$	KORALZ	50 000	6.5	7.7
1553	$\tau\tau$	KK2F	50 000	6.2	8.0
5105	qq	PYTHIA	100 000	1.1	90.1
9095	4f (eeee)	GRC4F	90 603	5.0	18.1
9275	4f (ee$\mu\mu$)	GRC4F	63 380	5.0	12.7
9276	4f (ee$\tau\tau$)	GRC4F	9 113	5.0	1.8
9542	4f ($\ell\ell\ell\ell$) (not eeff f = e/μ/τ)	GRC4F	16 173	5.0	3.2
9277	4f (eeqq)	GRC4F	207 129	5.0	41.4
1031	2γ (eeee)	VERMASEREN	800 000	1.0	805
1030	2γ (ee$\mu\mu$)	VERMASEREN	600 000	1.0	600
1032	2γ (ee$\tau\tau$)	VERMASEREN	430 000	1.0	438
1042	2γ untagged	PHOJET	999 999	0.1	10 560
1046	2γ tagged	PHOJET	5 000	2.3	2.21
1049	2γ tagged	HERWIG	150 000	0.5	302
1443	$\nu\nu$(nγ)	NUNUGAM	20 000	2.3	8.8
1354	ee(γ)	TEEGG	100 000	0.1	693
9859	$\gamma\gamma$	RADCOR	114 496	4.7	24.2
9206	4f ($\ell\ell\ell\ell$) (not eeff f = e/μ/τ)	KORALW	16 055	5.0	3.2
10082	4f M_{W}=79.33 GeV	KORALW	50 000	2.7	18.5
9900	4f M_{W}=80.33 GeV	KORALW	200 000	10.7	18.7
10083	4f M_{W}=81.33 GeV	KORALW	50 000	2.7	18.8

Table A.1: A list of the Monte Carlo samples employed in the TGC analysis performed at 192 GeV.

run	channel	generator	N_{ev}	$\int\mathcal{L}\,\mathrm{d}t$ [pb^{-1}]	σ [pb]
8704	WW $\rightarrow$ all	KORALW	200 000	11.6	17.2
9486	4f (0,0,0)	EXCALIBUR	190 000	10.1	18.8
9746	4f (+1,0,0)	EXCALIBUR	100 000	4.9	20.5
9747	4f (+0.5,0,0)	EXCALIBUR	100 000	5.2	19.1
9748	4f (-0.5,0,0)	EXCALIBUR	100 000	5.1	19.6
9749	4f (-1,0,0)	EXCALIBUR	100 000	4.7	21.4
9750	4f (0,+1,0)	EXCALIBUR	100 000	3.9	25.7
9751	4f (0,+0.5,0)	EXCALIBUR	100 000	4.9	20.4
9752	4f (0,-0.5,0)	EXCALIBUR	100 000	4.7	21.1
9753	4f (0,-1,0)	EXCALIBUR	100 000	3.7	27.1
9754	4f (0,0,+1)	EXCALIBUR	100 000	3.7	26.8
9755	4f (0,0,+0.5)	EXCALIBUR	100 000	4.8	20.7
9756	4f (0,0,-0.5)	EXCALIBUR	100 000	4.7	21.2
9757	4f (0,0,-1)	EXCALIBUR	100 000	3.6	27.8
9758	4f (+1,0,+1)	EXCALIBUR	100 000	3.8	26.2
9759	4f (+1,+1,0)	EXCALIBUR	100 000	3.6	27.9
9760	4f (0,+1,+1)	EXCALIBUR	100 000	2.4	41.1
1353	ee	BHWIDE	243 500	0.4	554
1625	$\mu\mu$	KORALZ	50 000	6.8	7.4
1627	$\mu\mu$	KK2F	50 000	6.3	7.9
1552	$\tau\tau$	KORALZ	50 000	6.8	7.3
1554	$\tau\tau$	KK2F	50 000	6.5	7.7
5106	qq	PYTHIA	250 000	2.9	85.3
9192	4f (eeee)	GRC4F	88 715	5.0	17.7
9278	4f (ee$\mu\mu$)	GRC4F	61 505	5.0	12.3
9279	4f (ee$\tau\tau$)	GRC4F	8 984	5.0	1.8
9543	4f ($\ell\ell\ell\ell$) (not eeff f = e/μ/τ)	GRC4F	16 474	5.0	3.3
9280	4f (eeqq)	GRC4F	202 483	5.0	40.5
1074	2γ (eeee)	VERMASEREN	823 118	1.0	824
1076	2γ (ee$\mu\mu$)	VERMASEREN	590 000	1.0	588
1078	2γ (ee$\tau\tau$)	VERMASEREN	440 000	1.0	440
1092	2γ untagged	PHOJET	999 999	0.1	10 890
1090	2γ tagged	F2GEN	346 000	1.0	346
1087	2γ tagged	HERWIG	160 000	0.5	310
1446	$\nu\nu$(nγ)	NUNUGAM	100 000	11.7	8.5
1354	ee(γ)	TEEGG	159 000	0.2	677
9859	$\gamma\gamma$	RADCOR	22 574	1.0	22.6
9203	4f ($\ell\ell\ell\ell$) (not eeff f = e/μ/τ)	KORALW	32 751	10.0	3.3
10084	4f M_{W}=79.33 GeV	KORALW	50 000	2.7	18.8
9905	4f M_{W}=80.33 GeV	KORALW	200 000	10.5	19.0
10085	4f M_{W}=81.33 GeV	KORALW	50 000	2.6	19.3

Table A.2: A list of the Monte Carlo samples employed in the TGC analysis performed at 196 GeV.

run	channel	generator	N_{ev}	$\int\mathcal{L}\,\mathrm{d}t$ [pb^{-1}]	σ [pb]
9210	WW $\rightarrow$ all	KORALW	200 000	11.5	17.4
9488	4f (0,0,0)	EXCALIBUR	192 000	10.1	19.1
9761	4f (+1,0,0)	EXCALIBUR	100 000	4.8	20.9
9762	4f (+0.5,0,0)	EXCALIBUR	100 000	5.2	19.4
9763	4f (-0.5,0,0)	EXCALIBUR	100 000	5.0	19.9
9764	4f (-1,0,0)	EXCALIBUR	100 000	4.6	22.0
9765	4f (0,+1,0)	EXCALIBUR	100 000	3.7	27.0
9766	4f (0,+0.5,0)	EXCALIBUR	100 000	4.8	20.9
9767	4f (0,-0.5,0)	EXCALIBUR	100 000	4.6	21.7
9768	4f (0,-1,0)	EXCALIBUR	100 000	3.5	28.7
9769	4f (0,0,+1)	EXCALIBUR	100 000	3.6	27.9
9770	4f (0,0,+0.5)	EXCALIBUR	100 000	4.7	21.1
9771	4f (0,0,-0.5)	EXCALIBUR	100 000	4.6	21.7
9772	4f (0,0,-1)	EXCALIBUR	100 000	3.4	29.1
9773	4f (+1,0,+1)	EXCALIBUR	100 000	3.7	27.2
9774	4f (+1,+1,0)	EXCALIBUR	100 000	3.4	29.5
9775	4f (0,+1,+1)	EXCALIBUR	100 000	2.3	44.1
1361	ee	BHWIDE	200 000	0.4	532
1640	$\mu\mu$	KORALZ	50 000	7.1	7.0
1628	$\mu\mu$	KK2F	60 000	8.0	7.5
1563	$\tau\tau$	KORALZ	50 000	7.1	7.0
1559	$\tau\tau$	KK2F	60 000	8.2	7.4
5121	qq	PYTHIA	250 000	3.1	80.9
9315	4f (eeee)	GRC4F	87 230	5.0	17.5
9316	4f (ee$\mu\mu$)	GRC4F	60 420	5.0	12.1
9317	4f (ee$\tau\tau$)	GRC4F	8 898	5.0	1.8
9312	4f ($\ell\ell\ell\ell$) (not eeff f = e/μ/τ)	GRC4F	16 727	5.0	3.3
9318	4f (eeqq)	GRC4F	197 391	5.0	39.5
1075	2γ (eeee)	VERMASEREN	825 000	1.0	825
1077	2γ (ee$\mu\mu$)	VERMASEREN	608 000	1.0	607
1079	2γ (ee$\tau\tau$)	VERMASEREN	450 000	1.0	445
1129	2γ untagged	PHOJET	999 999	0.3	3 159
1091	2γ tagged	F2GEN	349 000	1.0	349
1088	2γ tagged	HERWIG	164 000	0.5	314
1451	$\nu\nu$(nγ)	NUNUGAM	100 000	12.0	8.3
1356	ee(γ)	TEEGG	400 000	0.6	665
9562	$\gamma\gamma$	RADCOR	86 352	4.0	21.6
9209	4f ($\ell\ell\ell\ell$) (not eeff f = e/μ/τ)	KORALW	66 544	20.0	3.3
10086	4f M_{W}=79.33 GeV	KORALW	50 000	2.6	19.0
9910	4f M_{W}=80.33 GeV	KORALW	200 000	10.4	19.3
10087	4f M_{W}=81.33 GeV	KORALW	50 000	2.5	19.7

Table A.3: A list of the Monte Carlo samples employed in the TGC analysis performed at 200 GeV.

run	channel	generator	$N_{\rm ev}$	$\int \mathcal{L}\,{\rm d}t$ [pb^{-1}]	σ [pb]
9809	WW $\rightarrow$ all	KORALW	200 000	11.5	17.5
9850	4f (0,0,0)	EXCALIBUR	192 000	10.0	19.2
10018	4f (+1,0,0)	EXCALIBUR	50 000	2.4	21.1
10019	4f (-1,0,0)	EXCALIBUR	50 000	2.3	22.3
10020	4f (0,+1,0)	EXCALIBUR	50 000	1.8	27.7
10021	4f (0,-1,0)	EXCALIBUR	50 000	1.7	29.4
10022	4f (0,0,+1)	EXCALIBUR	50 000	1.8	28.4
10023	4f (0,0,-1)	EXCALIBUR	50 000	1.7	29.7
1362	ee	BHWIDE	200 000	0.4	521
1639	$\mu\mu$	KORALZ	50 000	6.8	7.4
1641	$\mu\mu$	KK2F	50 000	8.1	6.2
1564	$\tau\tau$	KORALZ	50 000	8.1	6.2
1562	$\tau\tau$	KK2F	50 000	7.0	7.2
5126	qq	PYTHIA	150 000	1.9	79.3
9806	4f (eeee)	GRC4F	86 400	5.0	17.3
9807	4f (ee$\mu\mu$)	GRC4F	59 240	5.0	11.9
9808	4f (ee$\tau\tau$)	GRC4F	8 763	5.0	1.8
9829	4f ($\ell\ell\ell\ell$) (not eeff f = e/μ/τ)	GRC4F	16 817	5.0	3.4
9713	4f (eeqq)	GRC4F	195 239	5.0	39.1
1133	2γ (eeee)	VERMASEREN	830 000	1.0	870
1135	2γ (ee$\mu\mu$)	VERMASEREN	360 000	1.0	348
1136	2γ (ee$\tau\tau$)	VERMASEREN	450 000	1.0	451
1129	2γ untagged	PHOJET	999 999	0.3	3 159
1091	2γ tagged	F2GEN	349 000	1.0	349
1088	2γ tagged	HERWIG	164 000	0.5	314
1453	$\nu\nu$(nγ)	NUNUGAM	50 000	6.0	8.1
1364	ee(γ)	TEEGG	250 000	0.4	657
9864	$\gamma\gamma$	RADCOR	21 253	1.0	21.3
9703	4f ($\ell\ell\ell\ell$) (not eeff f = e/μ/τ)	KORALW	33 497	10.0	3.4
10088	4f $M_{\rm W}$=79.33 GeV	KORALW	50 000	2.6	19.1
9915	4f $M_{\rm W}$=80.33 GeV	KORALW	200 000	10.3	19.4
10089	4f $M_{\rm W}$=81.33 GeV	KORALW	50 000	2.5	19.8

Table A.4: A list of the Monte Carlo samples employed in the TGC analysis performed at 202 GeV.

Appendix B

The OPAL Collaboration

G. Abbiendi[2], C. Ainsley[5], P.F. Åkesson[3], G. Alexander[22], J. Allison[16], G. Anagnostou[1], K.J. Anderson[9], S. Arcelli[17], S. Asai[23], D. Axen[27], G. Azuelos[18,a], I. Bailey[26], A.H. Ball[8], E. Barberio[8], R.J. Barlow[16], T. Behnke[25], K.W. Bell[20], G. Bella[22], A. Bellerive[9], G. Benelli[2], S. Bentvelsen[8], S. Bethke[32], O. Biebel[32], I.J. Bloodworth[1], O. Boeriu[10], P. Bock[11], J. Böhme[14,g], D. Bonacorsi[2], M. Boutemeur[31], S. Braibant[8], P. Bright-Thomas[1], L. Brigliadori[2], R.M. Brown[20], H.J. Burckhart[8], J. Cammin[3], P. Capiluppi[2], R.K. Carnegie[6], B. Caron[28], A.A. Carter[13], J.R. Carter[5], C.Y. Chang[17], D.G. Charlton[1,b], P.E.L. Clarke[15], E. Clay[15], I. Cohen[22], O.C. Cooke[8], J. Couchman[15], R.L. Coxe[9], A. Csilling[15,i], M. Cuffiani[2], S. Dado[21], G.M. Dallavalle[2], S. Dallison[16], A. De Roeck[8], E.A. De Wolf[8], P. Dervan[15], K. Desch[25], B. Dienes[30,f], M.S. Dixit[7], M. Donkers[6], J. Dubbert[31], E. Duchovni[24], G. Duckeck[31], I.P. Duerdoth[16], P.G. Estabrooks[6], E. Etzion[22], F. Fabbri[2], M. Fanti[2], L. Feld[10], P. Ferrari[12], F. Fiedler[8], I. Fleck[10], M. Ford[5], A. Frey[8], A. Fürtjes[8], D.I. Futyan[16], P. Gagnon[12], J.W. Gary[4],

G. Gaycken[25], C. Geich-Gimbel[3], G. Giacomelli[2], P. Giacomelli[8], D. Glenzinski[9], J. Goldberg[21], C. Grandi[2], K. Graham[26], E. Gross[24], J. Grunhaus[22], M. Gruwé[25], P.O. Günther[3], C. Hajdu[29], G.G. Hanson[12], K. Harder[25], A. Harel[21], M. Harin-Dirac[4], M. Hauschild[8], C.M. Hawkes[1], R. Hawkings[8], R.J. Hemingway[6], C. Hensel[25], G. Herten[10], R.D. Heuer[25], J.C. Hill[5], A. Hocker[9], K. Hoffman[8], R.J. Homer[1], A.K. Honma[8], D. Horváth[29,c], K.R. Hossain[28], R. Howard[27], P. Hüntemeyer[25], P. Igo-Kemenes[11], K. Ishii[23], F.R. Jacob[20], A. Jawahery[17], H. Jeremie[18], C.R. Jones[5], P. Jovanovic[1], T.R. Junk[6], N. Kanaya[23], J. Kanzaki[23], G. Karapetian[18], D. Karlen[6], V. Kartvelishvili[16], K. Kawagoe[23], T. Kawamoto[23], R.K. Keeler[26], R.G. Kellogg[17], B.W. Kennedy[20], D.H. Kim[19], K. Klein[11], A. Klier[24], S. Kluth[32], T. Kobayashi[23], M. Kobel[3], T.P. Kokott[3], S. Komamiya[23], R.V. Kowalewski[26], T. Kress[4], P. Krieger[6], J. von Krogh[11], D. Krop[12], T. Kuhl[3], M. Kupper[24], P. Kyberd[13], G.D. Lafferty[16], H. Landsman[21], D. Lanske[14], I. Lawson[26], J.G. Layter[4], A. Leins[31], D. Lellouch[24], J. Letts[12], L. Levinson[24], R. Liebisch[11], J. Lillich[10], C. Littlewood[5], A.W. Lloyd[1], S.L. Lloyd[13], F.K. Loebinger[16], G.D. Long[26], M.J. Losty[7], J. Lu[27], J. Ludwig[10], A. Macchiolo[18], A. Macpherson[28,l], W. Mader[3], S. Marcellini[2], T.E. Marchant[16], A.J. Martin[13], J.P. Martin[18], G. Martinez[17], T. Mashimo[23], P. Mättig[24], W.J. McDonald[28], J. McKenna[27], T.J. McMahon[1], R.A. McPherson[26], F. Meijers[8], P. Mendez-Lorenzo[31], W. Menges[25], F.S. Merritt[9], H. Mes[7], A. Michelini[2], S. Mihara[23], G. Mikenberg[24], D.J. Miller[15], W. Mohr[10], A. Montanari[2], T. Mori[23], K. Nagai[13], I. Nakamura[23], H.A. Neal[33], R. Nisius[8], S.W. O'Neale[1], F.G. Oakham[7], F. Odorici[2], A. Oh[8], A. Okpara[11], M.J. Oreglia[9], S. Orito[23], G. Pásztor[8,i], J.R. Pater[16], G.N. Patrick[20], P. Pfeifenschneider[14,h], J.E. Pilcher[9], J. Pinfold[28], D.E. Plane[8], B. Poli[2], J. Polok[8], O. Pooth[8], M. Przybycień[8,d], A. Quadt[8], K. Rabbertz[8], C. Rembser[8], P. Renkel[24], H. Rick[4], N. Rodning[28], J.M. Roney[26], S. Rosati[3], K. Roscoe[16], A.M. Rossi[2], Y. Rozen[21], K. Runge[10], O. Runolfsson[8], D.R. Rust[12], K. Sachs[6], T. Saeki[23], O. Sahr[31], E.K.G. Sarkisyan[8,m], C. Sbarra[26], A.D. Schaile[31], O. Schaile[31], P. Scharff-Hansen[8], M. Schröder[8], M. Schumacher[25], C. Schwick[8], W.G. Scott[20], R. Seuster[14,g], T.G. Shears[8,j], B.C. Shen[4], C.H. Shepherd-Themistocleous[5], P. Sherwood[15], G.P. Siroli[2], A. Skuja[17], A.M. Smith[8], G.A. Snow[17], R. Sobie[26],

S. Söldner-Rembold[10,e], S. Spagnolo[20], M. Sproston[20], A. Stahl[3], K. Stephens[16], K. Stoll[10], D. Strom[19], R. Ströhmer[31], L. Stumpf[26], B. Surrow[8], S.D. Talbot[1], S. Tarem[21], R.J. Taylor[15], R. Teuscher[9], J. Thomas[15], M.A. Thomson[8], M. Tönnesmann[32], E. Torrence[9], S. Towers[6], D. Toya[23], T. Trefzger[31], I. Trigger[8], Z. Trócsányi[30,f], E. Tsur[22], M.F. Turner-Watson[1], I. Ueda[23], B. Vachon[26], P. Vannerem[10], M. Verzocchi[8], H. Voss[8], J. Vossebeld[8], D. Waller[6], C.P. Ward[5], D.R. Ward[5], P.M. Watkins[1], A.T. Watson[1], N.K. Watson[1], P.S. Wells[8], T. Wengler[8], N. Wermes[3], D. Wetterling[11] J.S. White[6], G.W. Wilson[16], J.A. Wilson[1], T.R. Wyatt[16], S. Yamashita[23], V. Zacek[18], D. Zer-Zion[8,k]

[1]School of Physics and Astronomy, University of Birmingham, Birmingham B15 2TT, UK

[2]Dipartimento di Fisica dell' Università di Bologna and INFN, I-40126 Bologna, Italy

[3]Physikalisches Institut, Universität Bonn, D-53115 Bonn, Germany

[4]Department of Physics, University of California, Riverside CA 92521, USA

[5]Cavendish Laboratory, Cambridge CB3 0HE, UK

[6]Ottawa-Carleton Institute for Physics, Department of Physics, Carleton University, Ottawa, Ontario K1S 5B6, Canada

[7]Centre for Research in Particle Physics, Carleton University, Ottawa, Ontario K1S 5B6, Canada

[8]CERN, European Organisation for Nuclear Research, CH-1211 Geneva 23, Switzerland

[9]Enrico Fermi Institute and Department of Physics, University of Chicago, Chicago IL 60637, USA

[10]Fakultät für Physik, Albert Ludwigs Universität, D-79104 Freiburg, Germany

[11]Physikalisches Institut, Universität Heidelberg, D-69120 Heidelberg, Germany

[12]Indiana University, Department of Physics, Swain Hall West 117, Bloomington IN 47405, USA

[13]Queen Mary and Westfield College, University of London, London E1 4NS, UK

[14]Technische Hochschule Aachen, III Physikalisches Institut, Sommerfeldstrasse 26-28,

D-52056 Aachen, Germany
[15]University College London, London WC1E 6BT, UK
[16]Department of Physics, Schuster Laboratory, The University, Manchester M13 9PL, UK
[17]Department of Physics, University of Maryland, College Park, MD 20742, USA
[18]Laboratoire de Physique Nucléaire, Université de Montréal, Montréal, Quebec H3C 3J7, Canada
[19]University of Oregon, Department of Physics, Eugene OR 97403, USA
[20]CLRC Rutherford Appleton Laboratory, Chilton, Didcot, Oxfordshire OX11 0QX, UK
[21]Department of Physics, Technion-Israel Institute of Technology, Haifa 32000, Israel
[22]Department of Physics and Astronomy, Tel Aviv University, Tel Aviv 69978, Israel
[23]International Centre for Elementary Particle Physics and Department of Physics, University of Tokyo, Tokyo 113-0033, and Kobe University, Kobe 657-8501, Japan
[24]Particle Physics Department, Weizmann Institute of Science, Rehovot 76100, Israel
[25]Universität Hamburg/DESY, II Institut für Experimental Physik, Notkestrasse 85, D-22607 Hamburg, Germany
[26]University of Victoria, Department of Physics, P O Box 3055, Victoria BC V8W 3P6, Canada
[27]University of British Columbia, Department of Physics, Vancouver BC V6T 1Z1, Canada
[28]University of Alberta, Department of Physics, Edmonton AB T6G 2J1, Canada
[29]Research Institute for Particle and Nuclear Physics, H-1525 Budapest, P O Box 49, Hungary
[30]Institute of Nuclear Research, H-4001 Debrecen, P O Box 51, Hungary
[31]Ludwigs-Maximilians-Universität München, Sektion Physik, Am Coulombwall 1, D-85748 Garching, Germany
[32]Max-Planck-Institute für Physik, Föhring Ring 6, 80805 München, Germany
[33]Yale University,Department of Physics,New Haven, CT 06520, USA

[a] and at TRIUMF, Vancouver, Canada V6T 2A3

[b] and Royal Society University Research Fellow

[c] and Institute of Nuclear Research, Debrecen, Hungary

[d] and University of Mining and Metallurgy, Cracow

[e] and Heisenberg Fellow

[f] and Department of Experimental Physics, Lajos Kossuth University, Debrecen, Hungary

[g] and MPI München

[h] now at MPI für Physik, 80805 München

[i] and Research Institute for Particle and Nuclear Physics, Budapest, Hungary

[j] now at University of Liverpool, Dept of Physics, Liverpool L69 3BX, UK

[k] and University of California, Riverside, High Energy Physics Group, CA 92521, USA

[l] and CERN, EP Div, 1211 Geneva 23

[m] and Tel Aviv University, School of Physics and Astronomy, Tel Aviv 69978, Israel.

Bibliography

[1] C. Quigg, "Gauge Theories of the Strong, Weak and Electromagnetic Interactions", The Benjamin-Cummings Publishing Company Inc., US, 1983.

[2] F. Halzen and A. D. Martin, "Quarks and Leptons", John Wiley & Sons, US, 1984.

[3] C. Caso et al., "Review of Particle Physics", *Eur. Phys. J.* **C3**, 1 (1998).

[4] CDF Collaboration, F. Abe et al., "Observation of Top Quark Production in $p\overline{p}$ Collisions", *Phys. Rev. Lett.* **74**, 2626 (1995).

[5] D0 Collaboration, S. Abachi et al., "Observation of the Top Quark", *Phys. Rev. Lett.* **74**, 2632 (1995).

[6] DONUT Collaboration, M. Nakamura et al., "Result from DONUT: Direct Observation of ν/τ Interaction", *Nucl. Phys. Proc. Suppl.* **77**, 259 (1999).

[7] Super-Kamiokande Collaboration, T. Kajita, "Results from Super-Kamiokande", *Nucl. Phys. Proc. Suppl.* **85**, 44 (2000).

[8] N. Cabibbo, "Unitary Symmetry and Leptonic Decays", *Phys. Rev. Lett.* **10**, 531 (1963).

[9] M. Kobayashi and T. Maskawa, "CP Violation in the Renormalisable Theory of Weak Interaction", *Prog. Theor. Phys.* **49**, 652 (1973).

[10] G. 't Hooft, "Renormalisable Lagrangians for Massive Yang-Mills Fields", *Nucl. Phys.* **B35**, 167 (1971).

[11] S. L. Glashow, "Partial Symmetries of Weak Interactions", *Nucl. Phys.* **22**, 579 (1961).

[12] S. Weinberg, "A Model of Leptons", *Phys. Rev. Lett.* **19**, 1264 (1967).

[13] A. Salam, "Weak and Electromagnetic Interactions", Originally printed in "Svartholm: Elementary Particle Theory, Proceedings of The Nobel Symposium held in 1968 at Lerum, Sweden", Stockholm, 1968.

[14] D. Bardin et al., "ZFITTER 6.21: A Semi-Analytical Program for Fermion Pair Production in e^+e^- Annihilation", DESY 99-070, 1999.

[15] D. Bardin et al., "GENTLE/4fan 2.0: A Program for the Semi-Analytic Calculation of Predictions for the Process $e^+e^- \to 4f$", *Comput. Phys. Commun.* **104**, 161 (1997).

[16] A. Denner, S. Dittmaier, M. Roth, and D. Wackeroth, "$\mathcal{O}(\alpha)$ Corrections to $e^+e^- \to W^+W^- \to 4f(+\gamma)$: First Numerical Results from RACOONWW", *Phys. Lett.* **B475**, 127 (2000).

[17] S. Jadach, W. Placzek, M. Skrzypek, B. F. L. Ward, and Z. Was, "Final State Radiative Effects for the Exact $\mathcal{O}(\alpha)$ YFS Exponentiated (un)stable WW Production at and Beyond LEP2 Energies", *Phys. Rev.* **D61**, 113010 (2000).

[18] OPAL Collaboration, "Measurement of Standard Model Processes in e^+e^- Collisions at $\sqrt{s} > 202\,\mathrm{GeV}$", OPAL Physics Note PN462, 2000.

[19] P. Igo-Kemenes, "Status of Higgs Boson Searches", Talk at LEPC, November 2000, `http://lephiggs.web.cern.ch/LEPHIGGS/`.

[20] D. Abbaneo et al., "A Combination of Preliminary Electroweak Measurements and Constraints on the Standard Model", CERN-EP-2000-016, 2000.

[21] S. Myers and E. Picasso, "The Design, Construction and Commissioning of the CERN Large Electron Positron Collider", *Contemp. Phys.* **31**, 387 (1990).

[22] E. Picasso and G. Plass, "The Machine Design", *Europhys. News* **20**, 80 (1989).

[23] S. Myers, From Design to Approval "The LEP Collider and 1990" Commissioning, Nov 26, Lecture at the CERN Accelerator School, CERN 91-08, 1990.

[24] OPAL Collaboration, K. Ahmet et al., "The OPAL Detector at LEP", *Nucl. Instrum. Meth.* **A305**, 275 (1991).

[25] ALEPH Collaboration, D. Decamp et al., "ALEPH: A Detector for Electron - Positron Annihilation at LEP", *Nucl. Instrum. Meth.* **A294**, 121 (1990).

[26] DELPHI Collaboration, P. Aarnio et al., "The DELPHI Detector at LEP", *Nucl. Instrum. Meth.* **A303**, 233 (1991).

[27] L3 Collaboration, M. Acciarri et al., "The Construction of the L3 Experiment", *Nucl. Instrum. Meth.* **A289**, 35 (1990).

[28] P. P. Allport et al., "The OPAL Silicon Microvertex Detector", *Nucl. Instrum. Meth.* **A324**, 34 (1993).

[29] OPAL Collaboration, A. Honma, "The OPAL Silicon Strip Microvertex Detector Upgrade to two Coordinate Readout", *Nucl. Instrum. Meth.* **A348**, 409 (1994).

[30] S. Anderson et al., "The Extended OPAL Silicon Strip Microvertex Detector", *Nucl. Instrum. Meth.* **A403**, 326 (1998).

[31] J. R. Carter et al., "The OPAL Vertex Drift Chamber", *Nucl. Instrum. Meth.* **A286**, 99 (1990).

[32] H. M. Fischer et al., "The OPAL Jet Chamber", *Nucl. Instrum. Meth.* **A283**, 492 (1989).

[33] H. Drumm et al., "Experience with the Jet Chamber of the JADE Detector at PETRA (talk)", *Nucl. Instrum. Meth.* **176**, A333 (1980).

[34] G. Aguillion et al., "Thin Scintillating Tiles with High Light Yield for the OPAL Endcaps", *Nucl. Instrum. Meth.* **A417**, 266 (1998).

[35] C. Beard et al., "Thin, High Gain Wire Chambers for Electromagnetic Presampling in OPAL", *Nucl. Instr. Meth.* **A286**, 117 (1990).

[36] T. Kobayashi, "Realization of OPAL Electromagnetic Barrel Calorimeter", Prepared for the 2nd International Conference on Calorimetry in High-Energy Physics, Capri, Italy, 1991.

[37] P. W. Jeffreys et al., "Development Studies for the OPAL Endcap Electromagnetic Calorimeter using Vacuum Photo Triode Instrumented Lead Glass", *Nucl. Instrum. Meth.* **A290**, 76 (1990).

[38] G. Artusi et al., "Limited Streamer Tubes for the OPAL Hadron Calorimeter", *Nucl. Instr. Meth.* **A279**, 523 (1989).

[39] G. Mikenberg, "Thin Gap Gas Chambers for Hadronic Calorimetry", *Nucl. Instrum. Meth.* **A265**, 223 (1988).

[40] R. J. Akers et al., "The OPAL Muon Barrel Detector", *Nucl. Instrum. Meth.* **A357**, 253 (1995).

[41] G. T. J. Arnison et al., "Production and Testing of Limited Streamer Tubes for the Endcap Muon Subdetector of OPAL", *Nucl. Instrum. Meth.* **A294**, 431 (1990).

[42] B. E. Anderson et al., "The OPAL Silicon-Tungsten Calorimeter Front End Electronics", *IEEE Trans. Nucl. Sci.* **41**, 845 (1994).

[43] M. Arignon et al., "The Pretrigger System of the OPAL Experiment at LEP", *Nucl. Instrum. Meth.* **A333**, 330 (1993).

[44] M. Arignon et al., "The Trigger System of the OPAL Experiment at LEP", *Nucl. Instrum. Meth.* **A313**, 103 (1992).

[45] J. T. M. Baines et al., "The Data Acquisition System of the OPAL Detector at LEP", *Nucl. Instrum. Meth.* **A325**, 271 (1993).

[46] D. G. Charlton, F. Meijers, T. J. Smith, and P. S. Wells, "The Online Event Filter of the OPAL Experiment at LEP", *Nucl. Instrum. Meth.* **A325**, 129 (1993).

[47] C. Hawkes et al., "ROPE410 Users' Guide", 1996, OPAL Offline Note 16 / OFFL-0487.

[48] A. Buijis, "The OPAL DST (OD) Processor in ROPE", 1994, OPAL Offline Note 16 / OFFL-0318.

[49] T. Sjöstrand, "High-Energy Physics Event Generation with PYTHIA 5.7 and JETSET 7.4", *Comput. Phys. Commun.* **82**, 74 (1994).

[50] F. A. Berends, R. Pittau, and R. Kleiss, "Excalibur: A Monte Carlo Program to Evaluate all Four Fermion Processes at LEP200 and Beyond", *Comput. Phys. Commun.* **85**, 437 (1995).

[51] M. Skrzypek, S. Jadach, W. Placzek, and Z. Was, "Monte Carlo Program KORALW 1.02 for W Pair Production at LEP2/NLC Energies with Yennie-Frautschi-Suura Exponentiation", *Comput. Phys. Commun.* **94**, 216 (1996).

[52] S. Jadach, W. Placzek, M. Skrzypek, B. F. L. Ward, and Z. Was, "Monte Carlo Program KORALW 1.42 for all Four-Fermion Final States in e^+e^- Collisions", *Comput. Phys. Commun.* **119**, 272 (1999).

[53] S. Jadach, Z. Was, R. Decker, and J. H. Kuhn, "The Tau Decay Library TAUOLA 2.4", *Comput. Phys. Commun.* **76**, 361 (1993).

[54] G. Marchesini et al., "HERWIG v.5.1: A Monte Carlo Event Generator for Simulating Hadron Emission Reactions with Interfering Gluons", *Comput. Phys. Commun.* **67**, 465 (1992).

[55] CERN Application Software Group, "GEANT Detector Description and Simulation Tool", Software Manual CERN Program Library Long Writeup W5013, CERN, 1993.

[56] J. Allison et al., "The Detector Simulation Program for the OPAL Experiment at LEP", *Nucl. Instrum. Meth.* **A317**, 47 (1992).

[57] OPAL Collaboration, R. Akers et al., "Observations of π-B Charge-Flavour Correlations and Resonant Bπ and BK Production", *Z. Phys.* **C66**, 19 (1995).

[58] OPAL Collaboration, K. Ackerstaff et al., “B^* Production in Z^0 Decays”, *Z. Phys.* **C74**, 413 (1997).

[59] DELPHI Collaboration, P. Abreu et al., “B^* Production in Z^0 Decays”, *Z. Phys.* **C68**, 353 (1995).

[60] DELPHI Collaboration, P. Abreu et al., “Observation of Orbitally Excited B Mesons”, *Phys. Lett.* **B345**, 598 (1995).

[61] ALEPH Collaboration, D. Buskulic et al., “Production of Excited Beauty States in Z^0 Decays”, *Z. Phys.* **C69**, 393 (1996).

[62] ALEPH Collaboration, R. Barate et al., “Resonant Structure and Flavour Tagging in the $B\pi^{\pm}$ system using Fully Reconstructed B Decays”, *Phys. Lett.* **B425**, 215 (1998).

[63] L3 Collaboration, M. Acciarri et al., “Measurement of the Spectroscopy of Orbitally Excited B Mesons at LEP”, *Phys. Lett.* **B465**, 323 (1999).

[64] CDF Collaboration, T. Affolder et al., “Observation of Orbitally Excited B Mesons in $p\overline{p}$ Collisions at $\sqrt{s} = 1.8\,\mathrm{TeV}$”, *Submitted to Phys. Rev.* **D** (1999).

[65] OPAL Collaboration, G. Abbiendi et al., “Investigation of the Decay of Orbitally-Excited B Mesons and First Measurement of the Branching Ratio BR ($B_J^* \to B^*\pi(X)$)”, *Submitted to Eur. Phys. J.* **C** (2000).

[66] OPAL Collaboration, R. Akers et al., “A Model Independent Measurement of Quark and Gluon Jet Properties and Differences”, *Z. Phys.* **C68**, 179 (1995).

[67] OPAL Collaboration, G. Abbiendi et al., “Search for Higgs Bosons in e^+e^- Collisions at 183 GeV”, *Eur. Phys. J.* **C7**, 407 (1999).

[68] R. Kowalewski, “Study of Lifetime Tagging of b Hadrons in OPAL”, OPAL Technical Note TN181, 1993.

[69] A. N. Bell, “Evaluating the use of a Vertex Weight Method for Measuring the B^{**} and B_s^{**} Mass Peaks”, OPAL Technical Note TN448, 1996.

[70] C. Peterson, T. Rögnvaldsson and L. Lönnblad, "JETNET 3.0: A Versatile Artificial Neural Network Package", *Comput. Phys. Commun.* **81**, 185 (1994).

[71] I. Nakamura T. Omori, S. Asai and S. Yamashita, "MT User's Guide", 1994, OPAL documentation, version 1.51.

[72] S. Robins, "Inclusive Reconstruction of b Hadrons", OPAL Technical Note TN594, 1999.

[73] N. Isgur and M. B. Wise, "Spectroscopy with Heavy Quark Symmetry", *Phys. Rev. Lett.* **66**, 1130 (1991).

[74] S. Godfrey and R. Kokoski, "The Properties of P Wave Mesons with One Heavy Quark", *Phys. Rev.* **D43**, 1679 (1991).

[75] D. Ebert, V. O. Galkin, and R. N. Faustov, "Mass Spectrum of Orbitally and Radially Excited Heavy-Light Mesons in the Relativistic Quark Model", *Phys. Rev.* **D57**, 5663 (1998).

[76] E. J. Eichten, C. T. Hill, and C. Quigg, "Properties of Orbitally Excited Heavy-Light Mesons", *Phys. Rev. Lett.* **71**, 4116 (1993).

[77] A. Leins, "Search for the First Radial Excitation of B and B^* Mesons with the OPAL detector", Master's thesis, Albert Ludwig University, Freiburg, 1999.

[78] A. W. Lloyd, "Inclusive b Hadron Reconstruction and a Technique for Estimating the B^{**} Background", OPAL Technical Note TN604, 1999.

[79] OPAL Collaboration, K. Ackerstaff et al., "Measurement of $f(c \to D^{*+}X)$, $f(b \to D^{*+}X)$ and $\Gamma_{c\bar{c}}/\Gamma_{had}$ using $D^{*\pm}$ Mesons", *Eur. Phys. J.* **C1**, 439 (1998).

[80] A. N. Bell, "Measurements of the B^{**}, B_s^{**} Mass Peaks, and B Mixing using Data from the OPAL Experiment", PhD thesis, University of Birmingham, 1997.

[81] OPAL Collaboration, G. Abbiendi et al., "Search for Trilinear Neutral Gauge Boson Couplings in $Z\gamma$ production at $\sqrt{s} = 189\,\mathrm{GeV}$ at LEP", *Submitted to Eur. Phys. J.* **C** (2000).

[82] OPAL Collaboration, G. Abbiendi et al., “Z Boson Pair Production in e^+e^- Collisions at $\sqrt{s} = 183\,\mathrm{GeV}$ and $189\,\mathrm{GeV}$”, *Phys. Lett.* **B476**, 256 (2000).

[83] OPAL Collaboration, “Z Boson Pair Production in e^+e^- Collisions at $\sqrt{s} > 190\,\mathrm{GeV}$”, OPAL Physics Note PN423, 2000.

[84] OPAL Collaboration, G. Abbiendi et al., “Measurement of the $W^+W^-\gamma$ Cross-Section and First Direct Limits on Anomalous Electroweak Quartic Gauge Couplings”, *Phys. Lett.* **B471**, 293 (1999).

[85] L3 Collaboration, M. Acciarri et al., Measurement of the $WW\gamma$ Cross-Section and Direct Limits on Anomalous Quartic Gauge Couplings at LEP”, *Phys. Lett.* **B490**, 187 (2000).

[86] G. Altarelli, T. Sjöstrand and F. Zwirner, “Physics at LEP2”, CERN 09-01 Vol.1, 1996.

[87] D. Zeppenfeld K. Hagiwara, R. D. Peccei and K. Hikasa, “Probing the Weak Boson Sector in $e^+e^- \to W^+W^-$”, *Nucl. Phys.* **B282**, 253 (1987).

[88] F. M. Renard M. Bilenky, J. L. Kneur and D. Schildknecht, “Trilinear Couplings among the Electroweak Vector Bosons and their Determination at LEP200”, *Nucl. Phys.* **B409**, 22 (1993).

[89] C. Hamzaoui F. Boudjema, C. P. Burgess and J. A. Robinson, “CP Violating but P Preserving Electromagnetic Couplings of the $W^\pm$ and Z^0”, *Phys. Rev.* **D43**, 3683 (1991).

[90] OPAL Collaboration, K. Ackerstaff et al., “Measurement of the Triple Gauge Boson Coupling α_{W_ϕ} from W^+W^- Production in e^+e^- Collisions at $\sqrt{s} = 161\,\mathrm{GeV}$”, *Phys. Lett.* **B397**, 147 (1997).

[91] OPAL Collaboration, K. Ackerstaff et al., “Measurement of Triple Gauge Boson Couplings from W^+W^- Production at $\sqrt{s} = 172\,\mathrm{GeV}$”, *Eur. Phys. J.* **C2**, 597 (1998).

[92] OPAL Collaboration, G. Abbiendi et al., "W^+W^- Production and Triple Gauge Boson Couplings at LEP Energies up to 183 GeV", *Eur. Phys. J.* **C8**, 191 (1999).

[93] OPAL Collaboration, "Measurement of Single-W Production and Triple Gauge Boson Couplings in e^+e^- Collisions at $\sqrt{s} = 189$ GeV", OPAL Physics Note PN427, 2000.

[94] OPAL Collaboration, G. Abbiendi et al., "Measurement of Triple Gauge Boson Couplings from W^+W^- Production at LEP Energies up to 189 GeV", *Submitted to Eur. Phys. J.* **C** (2000).

[95] OPAL Collaboration, "Triple Gauge Boson Couplings in W^+W^- Production at LEP Energies up to 202 GeV", OPAL Physics Note PN441, 2000.

[96] OPAL Collaboration, G. Abbiendi et al., "Measurement of the W Boson Polarisation and CP Violating Triple Gauge Couplings from W^+W^- Production at LEP", *Submitted to Eur. Phys. J.* **C** (2000).

[97] ALEPH Collaboration, R. Barate et al., "A Study of Single-W Production in e^+e^- Collisions at $\sqrt{s} = 161$ GeV to 183 GeV", *Phys. Lett.* **B462**, 389 (1999).

[98] ALEPH Collaboration, R. Barate et al., "Measurement of Triple Gauge $WW\gamma$ Couplings at LEP2 using Photonic Events", *Phys. Lett.* **B445**, 239 (1998).

[99] ALEPH Collaboration, R. Barate et al., "Measurement of Triple Gauge Boson Couplings at 172 GeV", *Phys. Lett.* **B422**, 369 (1998).

[100] ALEPH Collaboration, "Measurement of Triple Gauge-Boson Couplings at LEP energies up to 189 GeV", ALEPH/2000-015, 2000.

[101] ALEPH Collaboration, "Measurement of Triple Gauge-Boson Couplings at 192-202 GeV", ALEPH/2000-016, 2000.

[102] DELPHI Collaboration, P. Abreu et al., "Measurement of Trilinear Gauge Couplings in e^+e^- Collisions at 161 GeV and 172 GeV", *Phys. Lett.* **B423**, 194 (1998).

[103] DELPHI Collaboration, P. Abreu et al., "Measurements of the Trilinear Gauge Boson Couplings WWV (V≡γ/Z) in e^+e^- collisions at 183 GeV", *Phys. Lett.* **B459**, 382 (1999).

[104] DELPHI Collaboration, "Measurement of Trilinear Gauge Boson Couplings WWV (V≡γ/Z) in e^+e^- Collisions at 189 GeV", DELPHI 2000-139, 2000.

[105] DELPHI Collaboration, "Measurement of Trilinear Gauge Boson Couplings in e^+e^- Collisions at 192-202 GeV", DELPHI 2000-146, 2000.

[106] L3 Collaboration, M. Acciarri et al., "Pair Production of W Bosons in e^+e^- Interactions at $\sqrt{s} = 161$ GeV", *Phys. Lett.* **B398**, 223 (1997).

[107] L3 Collaboration, M. Acciarri et al., "Measurements of Mass, Width and Gauge Couplings of the W Boson at LEP", *Phys. Lett.* **B413**, 176 (1997).

[108] L3 Collaboration, M. Acciarri et al., "Measurement of Triple Gauge Boson Couplings of the W Boson at LEP", *Phys. Lett.* **B467**, 171 (1999).

[109] L3 Collaboration, M. Acciarri et al., "Production of Single-W Bosons at $\sqrt{s} = 189$ GeV and Measurement of WWγ Gauge Couplings", *Phys. Lett.* **B487**, 229 (2000).

[110] L3 Collaboration, "Preliminary Results on the Measurement of Triple Gauge Boson Couplings of the W Boson at LEP", L3 note 2378, 1999.

[111] L3 Collaboration, "Preliminary Results on Single-W Boson Production at $192 \leq \sqrt{s} \leq 202$ GeV", L3 note 2518, 2000.

[112] L3 Collaboration, "Preliminary Results on the Measurement of Triple Gauge Boson Couplings of the W Boson at LEP", L3 note 2567, 2000.

[113] D0 Collaboration, B. Abbott et al., "Studies of WW and WZ Production and Limits on Anomalous WWγ and WWZ Couplings", *Phys. Rev.* **D60**, 072002 (1999).

[114] CDF Collaboration, F. Abe et al., “Limits on WWZ and WWγ Couplings from WW and WZ Production in $p\overline{p}$ collisions at $\sqrt{s} = 1.8\,\mathrm{TeV}$”, *Phys. Rev. Lett.* **75**, 1017 (1995).

[115] D. G. Charlton, “Measurement of Triple Gauge Coupling Parameters with WW $\to \ell\nu\ell\nu$ Events via an Unbinned Maximum Likelihood Fit”, OPAL Technical Note TN536, 1998.

[116] OPAL Collaboration, K. Ackerstaff et al., “Tests of the Standard Model and Constraints on New Physics from Measurements of Fermion Pair Production at 130 GeV to 172 GeV at LEP”, *Eur. Phys. J.* **C2**, 441 (1998).

[117] G. Wilson, “Towards an Event Selection of Acoplanar Di-Lepton Events Optimised for the WW $\to \ell\nu\ell\nu$ channel at $\sqrt{s} \approx 2M_{\mathrm{W}}$”, OPAL Technical Note TN382, 1996.

[118] G. Wilson, “An Improved Selection of Acoplanar Dilepton Events with High Visible Energy at $\sqrt{s} = 172\,\mathrm{GeV}$”, OPAL Technical Note TN446, 1996.

[119] T. Wyatt, “A General Selection of Lepton Pair Events Containing Missing Momentum at $\sqrt{s} = 161\,\mathrm{GeV}$”, OPAL Technical Note TN395, 1996.

[120] OPAL Collaboration, K. Ackerstaff et al., “Search for Anomalous Production of Di-Lepton Events with Missing Transverse Momentum in e^+e^- Collisions at $\sqrt{s} = 161\,\mathrm{GeV}$ and $172\,\mathrm{GeV}$”, *Eur. Phys. J.* **C4**, 47 (1998).

[121] OPAL Collaboration, G. Abbiendi et al., “W^+W^- Production Cross Section and W Branching Fractions in e^+e^- Collisions at 189 GeV”, *Submitted to Phys. Lett.* **B** (2000).

[122] G. Wilson, “Further Improvements to an Event Selection for Events with Two Charged Leptons and Missing Energy”, OPAL Technical Note (in preparation), 1999.

[123] K. Roscoe, “Improvements to the Classification of Leptonically Decaying W Pair Events at $\sqrt{s} = 189\,\mathrm{GeV}$”, OPAL Technical Note TN617, 1999.

[124] S. Jadach, W. Placzek, and B. F. L. Ward, "BHWIDE 1.00: $\mathcal{O}(\alpha)$ YFS Exponentiated Monte Carlo for Bhabha Scattering at Wide Angles for LEP1/SLC and LEP2", *Phys. Lett.* **B390**, 298 (1997).

[125] S. Jadach, B. F. L. Ward, and Z. Was, "The Monte Carlo Program KORALZ, for the Lepton or Quark Pair Production at LEP/SLC Energies", *Comput. Phys. Commun.* **124**, 233 (2000).

[126] S. Jadach, B. F. L. Ward, and Z. Was, "The Precision Monte Carlo Event Generator KK for Two- Fermion Final States in e^+e^- Collisions", *Comput. Phys. Commun.* **130**, 260 (2000).

[127] J. Fujimoto et al., "GRC4F 1.1: A Four-Fermion Event Generator for e^+e^- Collisions", *Comput. Phys. Commun.* **100**, 128 (1997).

[128] J. A. M. Vermaseren, "Two Photon Processes at Very High Energies", *Nucl. Phys.* **B229**, 347 (1983).

[129] M. Davier, L. Duflot, F. Le Diberder, and A. Rouge, "The Optimal Method for the Measurement of tau Polarisation", *Phys. Lett.* **B306**, 411 (1993).

[130] M. Diehl and O. Nachtmann, "Optimal Observables for the Measurement of Three Gauge Boson Couplings in $e^+e^- \to W^+W^-$", *Z. Phys.* **C62**, 397 (1994).

[131] M. Diehl and O. Nachtmann, "Anomalous Three Gauge Boson Couplings in $e^+e^- \to W^+W^-$ and Optimal Strategies for their Measurement", *Eur. Phys. J.* **C1**, 177 (1998).

[132] D. Fassouliotis G. K. Fanourakis and S. E. Tzamarias, "A Method to Include Detector Effects in Estimators Sensitive to the Trilinear Gauge Couplings", *Nucl. Instrum. Meth.* **A412**, 465 (1998).

[133] D. Fassouliotis G. K. Fanourakis and S. E. Tzamarias, "Accurate Estimation of the Trilinear Gauge Couplings using Optimal Observables Including Detector Effects", *Nucl. Instrum. Meth.* **A414**, 399 (1998).

[134] D. G. Charlton and A. W. Lloyd, "Measurement of Triple Gauge Coupling Parameters with Optimal Observables for WW $\to \ell\nu\ell\nu$ Events at $\sqrt{s} = 189\,\mathrm{GeV}$", OPAL Technical Note TN633, 1999.

[135] H. Voss, "TGC Measurement at 189 GeV in the WW $\to$ qq$\ell\nu$ Channel Using Optimal Observables", OPAL Technical Note (in preparation), 2000.

[136] F. James, "MINUIT Function Minimisation and Error Analysis", 1994, CERN Program Library Long Writeup D506.

[137] E. Bradley and E. J. Tibshirani, "An Introduction to the Bootstrap (Monographs on Statistics and No 57)" Applied Probability, Chapman & Hall, NY, 1993.

[138] R. J. Barlow, "Statistics, A Guide to the Use of Statistical Methods in the Physical Sciences", John Wiley & Sons, NY, 1989.

[139] LEP Energy Working Group, A. Blondel et al., "Evaluation of the LEP Centre-of-Mass Energy above the W Pair Production Threshold", *Eur. Phys. J.* **C11**, 573 (1999).

[140] D0 Collaboration, B. Abbott et al., "A Measurement of the W Boson Mass using Electrons at Large Rapidities", *Phys. Rev. Lett* **84**, 222 (2000).

[141] CDF Collaboration, F. Abe et al., "Measurement of the W Boson Mass", *Phys. Rev. Lett.* **75**, 11 (1995).

[142] LEP Electroweak Working Group, "A Combination of Preliminary Results on Electroweak Gauge Boson Couplings Measured by the LEP Experiments", LEPEWWG/TGC/2000-02, 2000.